Advanced Nanostructure Materials for Hybrid Supercapacitors

by

Salah Abureden

A thesis

presented to the University of Waterloo

in fulfillment of the

thesis requirement for the degree of

Doctor of Philosophy
in

Chemical Engineering (Nanotechnology)

Waterloo, Ontario, Canada, 2017

Examining Committee Membership

The following served on the Examining Committee for this thesis. The decision of the Examining Committee is by majority vote.

External Examiner	Dr. Tianpin Wu Physicist, Argonne National Laboratory-USA
Supervisors	Prof. Zhongwei Chen Professor & Canada Research Chair Chemical Engineering Department Prof. Aiping Yu Professor, Chemical Engineering
Internal Member	Prof. Ting Tsui Professor, Chemical Engineering; Director of Collaborative Graduate Program in Nanotechnology Prof. Boxing Zhao Professor, Chemical Engineering Department
Internal-external Member	Prof. Bo Cui Professor, Department of Electrical and Computer Engineering Director, Waterloo Nanofabrication Group

AUTHOR'S DECLARATION

This thesis consists of material all of which I authored or co-authored: see Statement of Contributions included in the thesis. This is a true copy of the thesis, including any required final revisions, as accepted by my examiners.

I understand that my thesis may be made electronically available to the public

Statement of Contributions

This thesis comprises contents of published work. Some chapters are reprinted from the below list of journal papers in adjusted format. The reference to each one of these papers is provided within the related chapters.

Salah Abureden, Fathy M Hassan, Gregory Lui, Wook Ahn, Serubbabel Sy, Aiping Yu, and Zhongwei Chen, "*Multigrain Electrospun Nickel Doped Lithium Titanate Nanofibers with High Power Lithium Ion Storage*", Journal of Material Chemistry A, 2016,**4**, 12638-12647

Salah Abureden, Fathy M Hassan, Gregory Lui, Serubbabel Sy, Rasim Batmaz, Wook Ahn, Aiping Yu, and Zhongwei Chen, "*Modified Chalcogens with Tuned Nano-Architecture for High Energy Density and Long Life Hybrid Super Capacitor*", Journal of Material Chemistry A, 2017,**5**, 7523-7532.

Salah Abureden, Fathy M Hassan, Aiping Yu, and Zhongwei Chen, "*Reconciled Nanoarchitecture with Overlapped 2D Anatomy for High Energy Hybrid Supercapacitors*", Energy Technology Journal-Wiley-VCH, accepted manuscript online: 8 May 2017.

Abstract

Hybrid supercapacitors (HSCs) are electrochemical devices that combine the characteristics of batteries and supercapacitors in one asymmetric cell. Lithium ion batteries (LIBs) and supercapacitors (SCs) represent two ends of the power and energy density spectrum. On one end of the Ragone plot spectrum, LIBs utilize faradaic reactions to provide high energy densities (150–250) $Whkg^{-1}$, however, this relatively slow reaction process limits the power density of LIBs (<1000 W kg^{-1}). The faradic mechanism intercalates/de-intercalates lithium into the active material, which causes changes in the chemical phase and increases the likelihood of material degradation, resulting in a limited cycle life (500-300 cycles). On the other end of the spectrum, SCs are based on electrostatic charge collection, which involve fast, reversible adsorption and desorption of ions on the surface of the active material without phase change or chemical reactions. For this reason, SCs are well known for their high power densities (~10 000 W kg^{-1}) and long cyclability (>100 000 cycles), however SCs suffer from limited energy densities (<10 $Whkg^{-1}$).

Combining half-battery and half supercapacitor in one device to bridge the energy/power density gap, while improving cycle life is a promising solution to meet the evolving energy requirements. However, the rapid fading of the power density, reduced capacitance retention and reduced cyclability at high power rates are the main challenges hindering the development of HSC devices. The power density decays significantly because the faradic material at the battery part can’t adjust its rate of charge-discharge reactions to match the adsorption-desorption rate of SCs. The capacitance retention and cycle life correspond to the stability of

the material on the battery component. To overcome these challenges, it is important to develop a new type of nanostructure materials with improved electrochemical capabilities.

In this work, we investigate a new class of nanostructure materials with high stability and improved reaction kinetics for the faradic component of the HSC. The development strategy introduces alterations to the intrinsic characteristics of the materials, without changing their chemical phase. The investigated materials included: 1D nickel doped lithium titanate oxide nanofibers, 2D vanadium-modified chalcogens nanosheets anchored graphene nanosheets, and reconciled 2D vanadium disulfide nanosheets with prominent 3D ultra-small nanoparticles attached to graphene nanosheets. The developed materials exhibit outstanding electrochemical performance.

In chapter 5, we report how a simple and scalable electrospinning technique was utilized to synthesis 1D nickel doped lithium titanate oxide nanofibers (Ni-LTONF$_{10}$). The physiochemical characterization confirmed: 1) the successful insertion of nickel into the lattice of the lithium titanate oxide nanofibers (LTONF) without changing its chemical structure and, 2) that the nickel was homogenously distributed throughout the nanofibers to the atomic level, resulting in significantly enhanced ion diffusion and electrical conductivity. This unique coupling of 1D morphology and nickel doping of LTO was investigated as the anode material for lithium ion batteries capable of demonstrating outstanding rate capabilities (up to 50 times higher than theoretical capacity (50 C)). The investigated nanofibers also performs 3 times better than nickel-doped nanoparticles demonstrated in other recent reports and shows outstanding ability to maintain high capacity even at 50 C. Ni-LTONF$_{10}$ shows 20 times higher

capacity compared to un-doped lithium titanate nanofibers at 50 C. Specifically, Ni-LTONF$_{10}$ displays an initial capacity of 190 mAhg^{-1} at 0.2 C which is 9% higher than the theoretical capacity of LTO, 150 mAhg^{-1} at 5 C, 116 mAhg^{-1} at 20 C and 63 mAhg^{-1} at 50 C. Additionaly, a hybrid supercapacitor was fabricated using Ni-LTONF$_{10}$, showing superior energy density at high power density. The device was capable of delivering an energy density of 60 Wh kg^{-1} at a power density of 1.5 kW kg^{-1} and also retained a high energy density of 35 Wh kg^{-1} at 5 kW kg^{-1}.

In chapter 6, we discuss the development of vanadium-modified binary chalcogens ($NiCo_2S_4$) wrapped with graphene (VNCS), forming tuned 2D sheet-on-sheet nanostructure. This unique material has been synthesized using a facile solvothermal method and is used as an electrode material for supercapacitors capable of demonstrating outstanding improvement in cyclability and capacitance retention at high power rates. The VNCS material shows a superior performance with 430% improvement in capacitance retention at high power rates (50 A g^{-1}) and 140% improvement in capacitance retention after 10,000 cycles at 10 A g^{-1}, when compared to the un-modified material. Specifically, the VNCS showed an initial capacitance of 1340 F g^{-1} at 2 A g^{-1} and outstanding capacitance retention at 50 A g^{-1} (1024 F g^{-1}). Impressively, the capacitance retention after 10,000 cycles at 10 A g^{-1} exceeds 90%. These exceptional results are considered at the top of reported work in literature as discussed in chapter 6. Moreover, a hybrid supercapacitor (HSC) was fabricated using the VNCS showing superior performance. The HSC delivers an energy density of 45.9 Wh kg^{-1} at 0.87 kW kg^{-1} and maintains a superior

energy density of 33.6 Wh kg^{-1} at 9 kW kg^{-1} indicating the excellent potential of this material in hybrid supercapacitor applications

The sheet-on-sheet structure reduced particle aggregation, provided larger surface areas with more electroactive sites for ion diffusion, enhanced the charge-discharge kinetics, which allows for faster electron transport. The morphology and structure characterization techniques confirmed that the vanadium is homogenously distributed throughout the binary chalcogens, resulting in significantly enhanced material stability at high power rates. HRTEM analysis confirmed the role of vanadium in fine-tuning the nano-architecture of the material and showed the dislocation in material structure.

In chapter 7, we introduce the use of a safe and simple solvothermal method to synthesize a distinctive, flower bouquet-like, 2D vanadium disulfide (VS_2) nanosheet structure with ultra-small prominent 3D VS_2 nanoparticles (10-25 nm) on its surface and anchored on the surface of graphene nanosheets (VS_2/G). This inimitable material has been tested in supercapacitors and showed superior capacitance, cyclability and capacitance retention at high power rates.

The VS_2/G showed 130 % higher capacitance at 1 A g^{-1} compared to other recent reports and remarkably improved capacitance at higher current densities. The material also showed a distinctive ability to maintain capacitance after long cycles at high current densities. Specifically, VS_2/G showed 211 F g^{-1} at 1 A g^{-1}, 135 F g^{-1} at 20 A g^{-1} and 97 % capacitance retention after 8000 cycles at 5 A g^{-1}. The VS_2/G was tested in a full cell HSC and showed superior energy density of 46.93 Wh kg^{-1} at a power density of 0.91 kW kg^{-1} and retained high energy density of 23.11 Wh kg^{-1} even when the power density was increased ten-fold (9.40 kW

k g^{-1}) highlighting the excellent potential of this material to bridge the gap between battery and supercapacitor technologies.

The unique morphology of VS_2 nanosheets embedded on graphene nanosheets with ultra-small VS_2 nanoparticles distributed uniformly at the surface of the nanosheets was confirmed by different characterization techniques including SEM and TEM. The presence of graphene and the harmonized synergy between the 2D sheet-on-sheet morphology with the 3D ultra-small VS_2 nanoparticles has a number of advantages. As such, it 1) hinders the agglomeration of the material and provides a large contact area with the electrolyte; and 2) generates strong covalent interactions between the VS_2 with the graphene surface. These characteristics lead to an increase in capacitance due to the increase in the number of electroactive sites and improve the charge transfer kinetics, while paving shorter ion diffusion pathways, all resulting in stable and reversible charge transfer processes.

Chapter 8 summarizes and concludes the thesis and suggests potential future works for capitalizing on the reported scientific achievements. The introduction of effective changes to the intrinsic characteristics of materials and the development of tuned and novel nanostructure materials, using simple and inexpensive methods, pave the way toward the development of commercial and industrial scale hybrid supercapacitor devices. Future work can investigate the design and development of thick electrodes in an attempt to exploit the high stability of the developed materials and increase the material loading on the electrodes leading to higher energy densities without scarifying the power densities. The increased working voltage and the long cycling life along with the high capacitance retention of the developed materials at high power

rates can be used as a base to investigate the design of multi-stack device for industrial scale applications such as electrical vehicles, backup systems, transportation, etc. It is also recommended to further investigate incorporating the developed material in other energy storage and conversion devices.

Acknowledgements

First of all, I would like to thank my supervisors, Professor Zhongwei Chen and Professor Aiping Yu for the great support, passion and guidance they provided throughout my PhD study. I also want to thank my colleagues at the clean energy and applied nanomaterial laboratories for their help.

Special thanks to the faculty and staff of the chemical engineering department for their kindness and support. Of particular note is Mrs Judy Caron, who provided great help during my studies.

I would like also to acknowledge and thank the examining committee, including Professor Ting Tsui, Professor Boxing Zhao, Professor Bo Cui and Professor Tianpin Wu from Argonne National Laboratory for their valuable advices.

Finally, I would like to thank my family and friends for their patience, encouragement and support they provided every day during my PhD journey.

Dedication

To the soul of my father…...no words can describe how much I miss you.

Table of Contents

List of Figures

List of Tables

List of Abbreviations

AC: Activated carbon

C.R: capacitance retention

CD: Charge-discharge

CE: Counter electrode

CV: Cyclic voltammetry

DDI: Distilled de-ionized water

EC-DMC: ethylene carbonate- dimethyl carbonate

EDL: Electrical double layer

EDX: Energy dispersive x-ray

EELS: electron energy loss spectroscopy

EG – Ethylene glycol

EIS: electrochemical impedance spectroscopy

GNCS: Graphene wrapped nickel cobalt sulfide

GO – Graphene oxide

HAADF: High annular angle dark field

HSC: Hybrid Supercapacitor

LIBs: Lithium ion batteries

NCS: nickel cobalt sulfide

Ni-LTONF: Nickel doped lithium titanate oxide nanofibers

NMP: N-methyl-pyrrolidone

PVDF: Polyvinylidene fluoride

RE: Reference electrode

SAD: Selected area diffraction

SCs: Supercapacitors

SEM: Scanning electron microscopy

SG: Sulfur doped graphene

STEM: scanning transmission electron microscopy

TEM: Transmission electron microscopy

BET: Brunauer–Emmett–Teller

TGA: Thermogravimetric analysis

VNCS: Vanadium modified nickel cobalt sulfide

VS2: vanadium di-sulfide

WE: Working electrode

XPS: X-ray photoelectron spectroscopy

XRD: X-ray diffraction

Chapter 1: Introduction

1.1 The energy challenge

The developments of portable electronics, electric vehicles, and smart grids are increasing the need for reliable energy storage devices with safe operations and high energy and power capabilities.[2,3] Lithium ion batteries (LIBs) and supercapacitors (SCs) are two examples of reliable and cost effective energy storage and conversion technologies. LIBs are based on faradaic reactions that can provide high energy densities (hours of operation at a given weight) but suffer from low power densities and a limited cycle life. LIBs have been studied extensively in the past years as one of the most promising candidates for energy storage applications. However, current graphite-based, electrode technologies used in LIBs suffer from limited power capabilities and limited cycle life.[4] To address these challenges, scientists have investigated a number of alternative materials including metal oxides and conductive polymers.[5] These efforts are focused on reducing the charging time, increasing the amount of stored charge per unit mass or volume, increasing cyclability and reducing production cost.

Complementarily, SCs are energy storage devices that can provide decent energy densities at high power densities over a large number of cycles.[6-8] SCs are used in applications where many charge-discharges are required in quick successions such as in back-up systems and electrical generators. One of the main shortcomings of supercapacitors lies with their low energy density compared to current lithium ion battery technology. Therefore, the majority of recent research has been dedicated to developing supercapacitors with enhanced energy densities without compromising on the power density. Supercapacitors are typically fabricated by introducing high

surface-area materials (maximizing the area for electrochemical double-layer capacitance) or pseudocapacitive materials including conducting polymers and metal oxides (in order to induce charge transfer-based storage).[7] Pseudocapacitive materials provide higher energy densities due to their redox-based charge transfer mechanism. Combining half a supercapacitor with half a battery in one device creates a new class of energy storage devices known as hybrid supercapacitors (HSCs) or asymmetric supercapacitors.

The global market size for SCs increased from $643.4 million in 2012 to $776 million in 2013 and $1.15 billion in 2016. This growth is expected to continue with an annual growth rate of 19% to reach $2.1 billion by 2019. The global market for LIBs have also increased from 16.2 billion in 2012 to 22.6 billion in 2016 and is expected to reach 43 billion in 2019.[9,10] Based on these statistics, we can conceive the growing market for the hybrid supercapacitors if sufficient scientific progress can be made to overcome the current development challenges and to bridge the gap between supercapacitors and batteries technologies (**Figure1-1**). The proceeding sections will introduce the fundamental principles of SCs and LIBs. Chapter 2 will discuss the theory and structure of HSCs in more details.

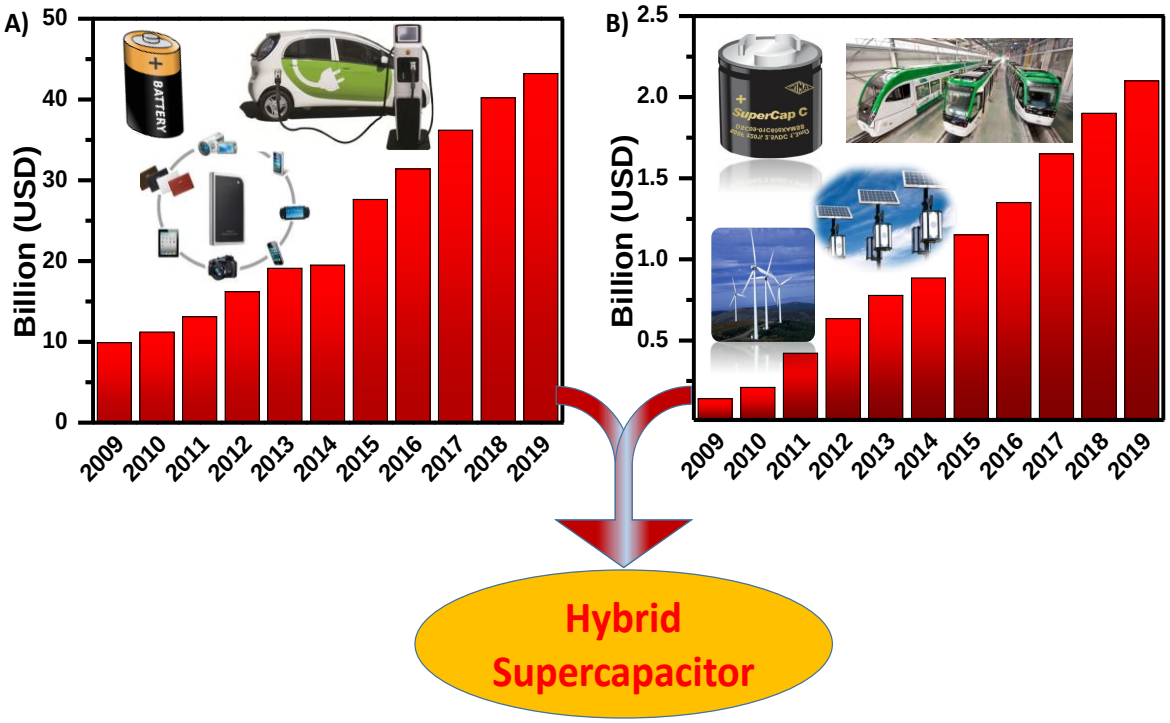

Figure 1-1 Market data for A) LIBs, and B) SCs. The data used to plot the graphs is obtained from *energy storage association http://energystorage.org and, from ref.[1])*

1.2 Supercapacitors

The working principle of supercapacitors (SCs) is based on accumulating charge at the interface between the electrode surface and the electrolyte known as electrical double layer (EDL or EDLC). This physical process is highly reversible, up to thousands of cycles and doesn't induce chemical reactions or phase changes. A supercapacitor can be constructed with two identical, parallel, carbon-based electrodes in a cell filled with electrolyte and separated by a membrane (**Figure1-2)** At open circuit, there is no potential difference, however, if we

close the circuit and connect the cell to an external power supply, current will start to flow from one electrode to the other, generating a potential difference between the electrodes. The charge will be separated and accumulated at both ends of the cell in the area between the electrode and electrolyte. This is similar to creating two in-series capacitors joined by electrolyte as a connector. If we subsequently open the circuit again, the potential difference will continue to exist because the charge has already been stored when the solvated ions of the electrolyte were attracted to the electrode of opposite charge. The EDL is a very thin layer (~ 1 nm) with direct contact with both electrolyte and electrode surface. The amount of stored charge depends on the surface area of the electrode, therefore activated carbon is an ideal choice for SCs (i.e. surface area can reach 2300 m^2 per gram).[11] The charge-discharge process is very fast (seconds) due to the ease of ions movement from the electrolyte medium to the surface of the active material and vice versa and because there is no reaction at the interface and is only limited by diffusion of the ions to the active sites. In addition to the EDL mechanism, a secondary charge-transfer mechanism based on reversible faradic reactions can play a role in storing charge in SCs. This mechanism is based on storing charge by diffusing ions into the active material and inducing phase changes. depending on the type of active material, pseudocapacitance contributes typically 5-10 % of the total SC capacitance.[12]

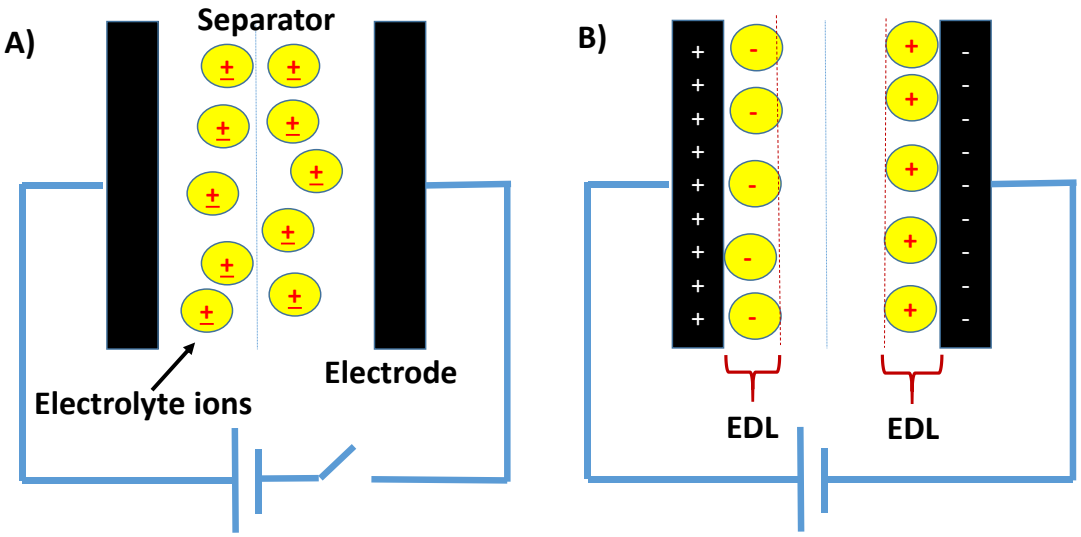

Figure 1-2. Schematic representation of the working mechanism of supercapacitor and showing the charge status at A) open circuit, and B) closed circuit

1.3 Lithium ion batteries

Lithium ion batteries (LIBs) are comprised of two electrodes, electrolyte and a separator. The working principle of LIBs is based on faradic redox reactions, *i.e.* charge is generated due to phase changes in the electrodes and not at the electrode/electrolyte interface, like in the case of SCs. The active material is usually constituted of lithium intercalated compounds (**Figure1-3)**.[13,14] During the discharge process, the positive charge ions will travel from the anode to cathode through the electrolyte medium, which will force the electrons of the anode to travel through the outer circuit generating current flow. These electrons will meet the positive ions diffusing into the opposite electrode. This process is reversed during charging operations.[15,16]

LIBs are widely used in many applications, especially in portable electronic devices because of their high energy density and low rate of self-discharge when idle.

The electrochemical performance of LIBs depends on the type of the active material and electrolyte, and as a result, affects the operating voltage. The most commonly-used active materials for LIBs are lithium cobalt oxide ($LiCoO_2$), lithium manganese oxide (LMO), lithium iron phosphate (LFP) and lithium nickel manganese cobalt oxide (NMC). $LiCoO_2$ is the most widely used active material because it has higher energy density compared to the other materials, however, it deteriorates quicker when cycled leading to shorter cycle life. LIBs pose safety hazards if damaged because they use flammable electrolytes inside pressurized cells.

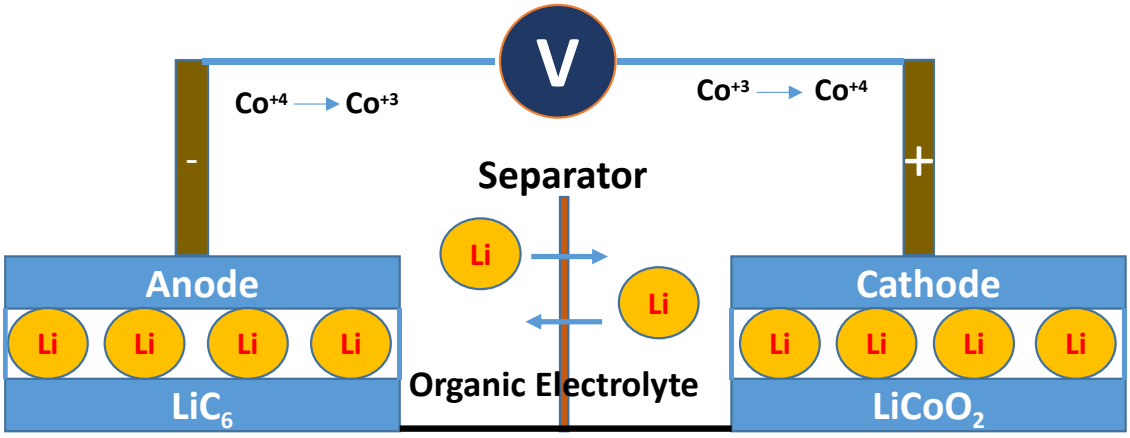

Figure 1-3. Schematic representation of the LIB structure and working mechanism

1.4 SCs Vs LIBs

Table 1-1 summarizes the main differences between LIBs and SCs. These differences stem from the difference in the charge transfer mechanism.[12,15]

Table 01-1. Comparison between LIBs and SCs

	LIBs	**SCs**
Charge storage mechanism	Faradic redox reactions	EDL/Pseudocapacitance
Power limitations	Reaction-kinetics, active- material, and conductivity	Electrolyte conductivity (how quickly ions can diffuse within the electrolyte)
Energy limitations	Mass of active material (bulk)	Specific surface area
Rate of charge-discharge	Controlled by lithium diffusion kinetics	Controlled by the physical charge accumulation
Cycle life limitations	Material stability and reaction reversibility	Side reactions
Life-limitations	Thermodynamics stability	Side reactions
Energy density (Wh kg^{-1})	< 150	< 10
Power density (W kg^{-1})	2-15	<14000
Cycle life	500-3000	>100,000
Charge-discharge time	Hours	Seconds/minutes

Chapter 2: Hybrid Supercapacitors

This chapter will introduce the main concept of HSCs, energy and power density definitions, the structure of HSC, the contributions of LIBs and SCs on HSCs, and the main challenges hindering the development of HSC.

2.1 Chapter introduction

The conception of creating a hybrid device is to complement the characteristics of batteries and supercapacitors; this has attracted the attention of many researchers in the last decade. The simplest approach to preparing HSCs is by combining one electrode from a battery and one electrode from a supercapacitor in one asymmetric cell. Although HSCs are composed of half a battery and half a supercapacitor, they still grouped in the family of SCs (**Figure 2-1**) due to the influential effect of EDL on the overall performance of HSC. The combination of the two mechanisms together should, theoretically, increase the maximum charge capacity. The total stored charge is determined by the contribution of each half; in other words, the total transferred charge should be equal to the sum of the charges on each side of the HSC.[17] However, the type of the active material used on each electrode and the other cell components govern the amount of stored charge, device stability, cycle life, and power and energy densities. The main disadvantage of this approach is the mismatch in the amount of delivered power and energy densities of each electrode at both low and high current rates. At low current rates, the relatively slow faradic reaction kinetics at the battery part will dominate the charge transfer mechanism and the respective power and energy densities. When the current rate increases, the rate of

faradic reactions will not be able match the EDL's charge transfer rate. Therefore, at high rates of current, the EDL will dominate the cell performance delivering low energy density and a power density lower than SCs.[12,17] To overcome this, it is crucial to improve the characteristics of the electrode material at the battery half to continue to deliver high energy density, while simultaneously deliver high power density and match the charge storage and transfer kinetics of EDL component.

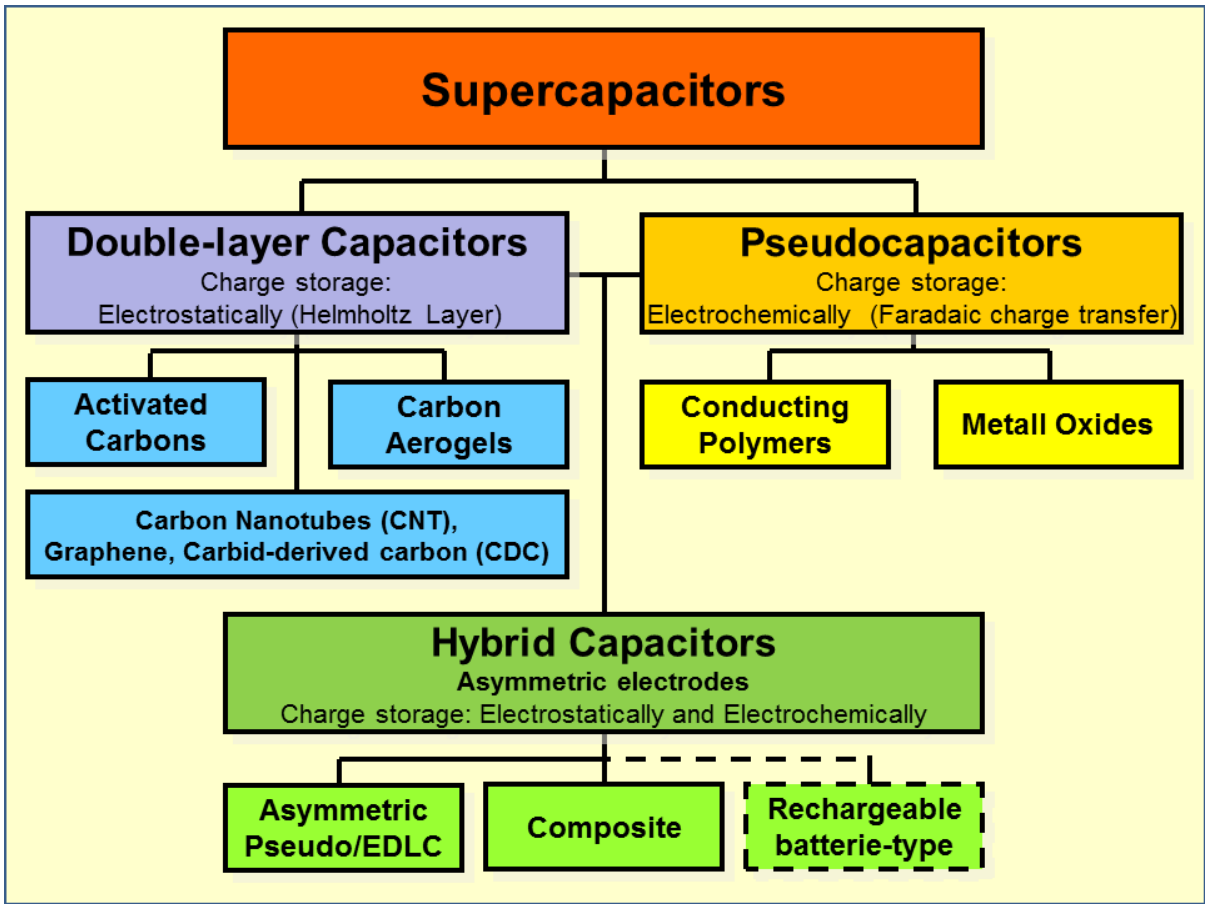

Figure 2-1. Schematic showing the Hierarchical classification of supercapacitors and related types.

(Source *https://en.wikipedia.org/wiki/User:Elcap/Supercapacitor*)

2.2 Energy and power densities

Energy density is the amount of energy stored per unit mass (Wh g^{-1}) or per unit volume (Wh cm^{-3}). Energy density is a function of the specific capacitance and operating voltage of the device as shown in **Equation 2-1:**[18,19]

$$\boldsymbol{E = \frac{1}{2} C V^2} \qquad \textbf{(2-1)}$$

Where E is the specific energy density (Wh g^{-1}), C is the specific capacitance (Farad g^{-1}), and V is the operating voltage (Volt).

Power density measures the ability to deliver power. In other words, it is how quickly the energy storage system can discharge the stored energy per unit mass or volume. Power density is calculated using the following equation: [18,19]

$$\boldsymbol{P = \frac{E}{dt}} \qquad \textbf{(2-2)}$$

Where P is the power density (W g^{-1}), E is the energy density (Wh g^{-1}), and dt is the time (h).

The difference in energy storage technologies leads to different energy and power capabilities. The relationship between the energy density and power density of different energy storage devices is summarized in what is known as Ragone plot (**Figure 2-2).** The classification of the performance of newly developed hybrid devices is assessed by their location on the Ragone plot and their proximity to other devices. For example, high quality HSCs should have a performance that can surpass both LIBs and SCs on the Ragone plot.

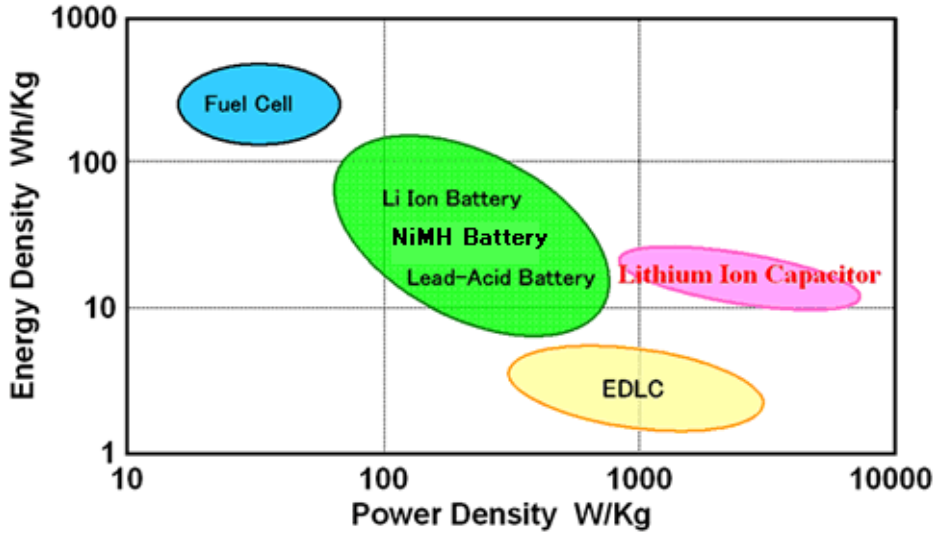

Figure 2-2. Ragone plot showing the relationship between energy density and power density for different energy storage devices (*source of image Wikipedia www.wikipedia.com*)

2.3 Structure

This section will introduce the structure of the asymmetric, HSC and the function of each component. The main components of HSC are similar to LIBs and SCs: cathode and anode, electrolyte, and separator as shown in in **Figure 2-3**.

2.3.1 Anode and cathode

The selection of the proper materials for the cathode and anode depends on a number of factors:[12,20] 1) specific surface area (SSA): the electrostatic accumulation from EDL are stored at the surface of the active material. Therefore, high SSA such as activated carbon will allow for more charge storage sites. 2) electrical conductivity: conductivity is an important factor in determining the charge transfer kinetics; highly conductive materials can operate under higher

current densities and allow for faster reaction kinetics, which will lead to higher rate capabilities and capacitance retention. 3) material stability: it is important to select materials with high mechanical and chemical stability. The material stability is the crucial factor to determining the cycle life of HSC. Lastly, 4) cost and safety: the selection of safe, abundant and cost-effective materials is an essential factor to the practical implementation of HSC electrodes. The faradic part in HSC will act like the "energy" provider and the EDL part will act like the "power" provider

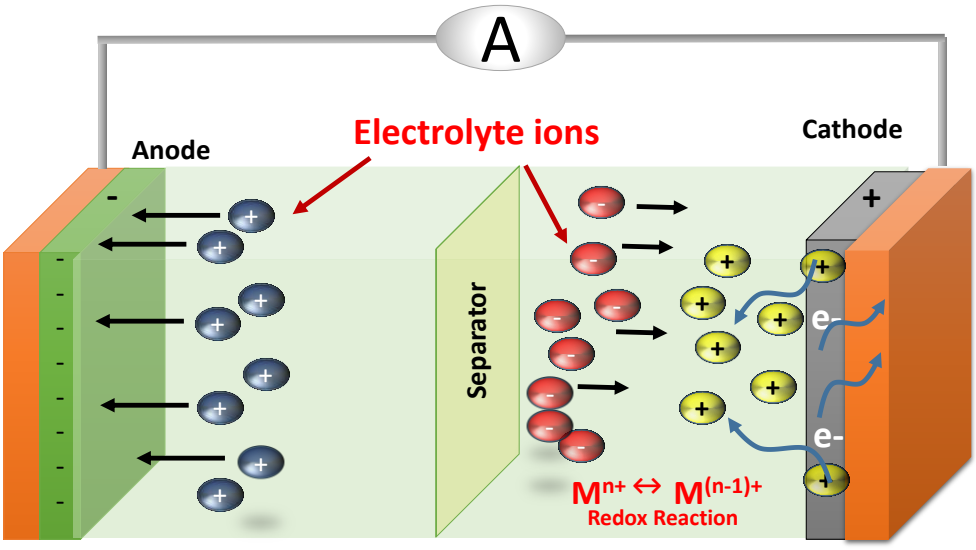

Figure 2-3. Schematic depicting the structure of hybrid supercapacitor and showing the main components and the charges transfer principles.

2.3.2 Separator

The separator in HSC is ideally placed in the center of the device, equidistant from each electrode. The separator's primary function is to prevent direct contact between the two electrodes, while simultaneously allowing ions to diffuse across the device. Number of factors need to be considered when selecting the proper separator such as: 1) mechanical stability and permeability, 2) chemical stability in different electrolytic mediums, 3) ion conductivity, which allows for facile diffusion through the separator membrane (less resistance) and, 4) electrical conductivity; poor electrical conductivity is required to avoid shorting the circuit. Most commonly used separators in HSC are made of polyethylene, polyvinyl alcohol, polyolefin, and polypropylene.[21]

2.3.3 Electrolyte

The thermodynamic stability of the electrolyte determines the operating voltage, which directly affects the energy and power densities. Selecting the proper electrolyte depends mainly on the chemical stability of the active material in the electrolyte medium. Other factors to consider also include:[20,22] 1) chemical and thermal stability of the electrolyte itself, 2) conductivity; good ion conductivity and poor electrical conductivity are required 3) ionic concentration and purity; the concentration depends on the loading of active material and high purity is essential requirement, 4) size of solvated ions; the size of solvated ions need to be smaller than the pores of the separator membrane, 5) viscosity; reasonable levels of viscosity is required to minimize the diffusion resistance of the ions in the electrolyte, 6) cost, and 7) safety and environmental impacts.

The most common electrolytes are dissolved in organic or aqueous solvents. Organic electrolytes can operate under relatively high potential windows (2.5 - 3.5 V) which is crucial to increasing the energy density. However, organic electrolytes are flammable, expensive and require strict atmospheric controls during device fabrication (within glove box) to ensure chemical stability. [20] On the other hand, aqueous electrolytes are safer, inexpensive, abundant, and chemically stable in regular room conditions. However, aqueous electrolytes suffer from a limited operating voltage window. The working voltage of the aqueous electrolytes is determined by the electrolyte type and can reach up to 2.0 V.[17,22,23]

In addition to organic and aqueous electrolytes, ionic liquid electrolytes composed from anions and cations (i.e. molten salts) are also used in energy storage device. Ionic liquids are known for their high chemical and thermal stability and high working voltage (up to 4.0 V). However, ionic liquid electrolytes tend to be more expensive and suffer from high viscosities and low ionic conductivities. [22]

2.4 The Working principle

As mentioned earlier, the SC component in a HSC device will generate charge using EDL and pseudocapacitance mechanisms while the battery component will generate charge using faradic redox reactions only. When the surface of SC electrode is exposed to electrolyte, a very thin EDL layer is formed at the electrode-electrolyte interface as seen in **Figure 2-4**. This layer is called electrical double layer (EDL or EDLC) because two layers of charges will be formed at both sides of the interface between the electrolyte and electrode. The first layer of charges is made of the adsorbed ions accumulated at the surface of active material. The second layer is

called the diffusion layer, which includes the charges attracted to the surface of active material by coulombic forces and thermal motion of the solvated ions in the electrolyte.[12]

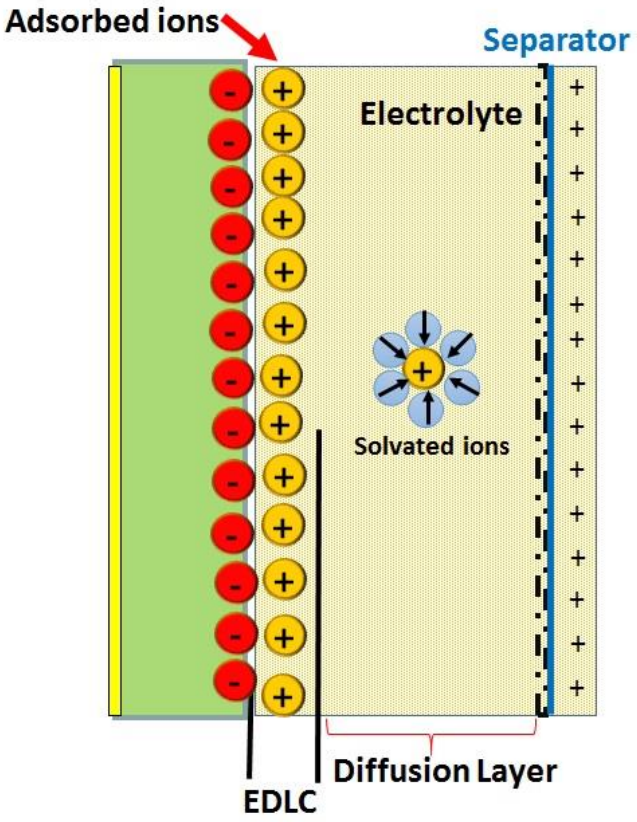

Figure 2-4. Schematic illustrating the EDL charge accumulation mechanism and showing the two layers of adsorbed ions and diffusion layer.

Pseudocapacitance happens when the de-solvated electrolytes ions diffuse into the bulk of active material causing redox reactions. Pseudocapacitance occurs only with EDL and they both contribute to the overall capacitance of the SC part in HSC. The level of the contribution of pseudocapacitance increases with increasing the operating voltage which acts as a driving

force towards the migration of the de-solvated ions. The contribution of pseudocapacitance is also affected by the design of the electrodes and the type of the used electrolyte.[24] The overall specific capacitance of SCs is measured in Farad per gram and is expresses in **equation 2-3** shown below:[25]

$$C = Q/mV \qquad \textbf{(2-3)}$$

Where C is the specific capacitance (Fg^{-1}), Q is the stored charge (coulombs), m is the mass of the active material (g), and V is the working voltage range (V).

Since two mechanisms contribute to the overall capacitance, the theoretical capacitance for each mechanism can be calculated separately using **equations 2-4 and 2-5** below:[12,25]

$$\text{For EDL:} \quad C = \varepsilon_r \varepsilon_o A / d \qquad \textbf{(2-4)}$$

Where ε_r is the relative permittivity of the EDL (Fm^{-1}), ε_o is the permittivity of vacuum (Fm^{-1}), A is the specific surface area of the active material (m^2), and d is the width of EDL (m).

$$\text{Pseudocapacitance:} \quad C = n F / (M V) \qquad \textbf{(2-5)}$$

Where n is the number of the electrons involved in the faradic reaction, F is Faraday's constant (96485 C mol^{-1}), M is the molecular weight (g mol^{-1}), and V is the working voltage range (V).

The working principle for the battery component is similar to conventional LIBs discussed in section 1.3. The amount of ions and electrons generated from the chemical redox reactions determine the capacity. The theoretical capacity ($mAhg^{-1}$) can be calculated based on the faradic reactions formula. For example, the reaction for LiC_6 is shown in **equation 2-6** below:

$$Li^+ + e^- + C_6 \leftrightarrow LiC_6 \qquad \textbf{(2-6)}$$

The theoretical specific capacity is calculated using **equation 2-7:**[15]

$C_s = eF\,(nM)^{-1} = 1\times 96485/6\times(12) = 372\ \text{mAhg}^{-1}$ **(2-7)**

Where C_s is the specific capacity in mAh g^{-1}, e is number of electrons, F is Faraday's constant (96485 C mol^{-1}), n is the number of moles reacted, and M is the molecular weight ($gmol^{-1}$). Similarly, we can calculate the theoretical specific capacity for the reaction of $LiCoO_2$ shown in **equation 2-8**:

$LiCoO_2 \leftrightarrow 0.5Li^+ + 0.5e^- + Li_{0.5}CoO_2$ **(2-8)**

The theoretical capacity is equal to 272 $mAhg^{-1}$ (1C). The theoretical capacity is measured by C-rate (mA g^{-1}). 1C rate means that the applied discharge current can completely discharge the battery in 1 hour.

Combining the two different mechanisms in one hybrid device will dictate the operating voltage window and, overall energy and power output of the device. To elaborate, **Figure 2-5** schematically illustrates the process of combining half a battery and half a supercapacitor. **Figure 2-5A** shows half a supercapacitor (one electrode) and its corresponding charge-transfer profile. The potential profile is linear because the EDL mechanism is based on physical collection of charge on the surface of the active material. Thus, the energy stored in the capacitor half will be equal to the area of the triangle shown in **Figure 2-5A**.[26] On the battery component, the faradic material follows the Nernstian behavior, which includes a phase change and reaching an equilibrium. During equilibrium, the driving forces moving the charges will be at stabilized status leading to voltage plateau, thus, the energy stored in half battery will be equal to the area under the curve shown in **Figure 2-5B**.[26] Combining the two different types of electrodes in one device will merge the high power density characteristic of EDL materials

(and low energy density) with high energy density of the faradic redox material (and low power density) as shown in **Figure 2-5C**. This merger will be accompanied with an increase in the working voltage window, which in turn, should theoretically lead to an increase in the energy density and power density. However, the slow reaction kinetics of the faradic part compared to EDL component will limit the hybrid device capabilities in transferring all available charge in both ways (charge-discharge) and reaching its maximum energy storage and power capabilities.[17,27]

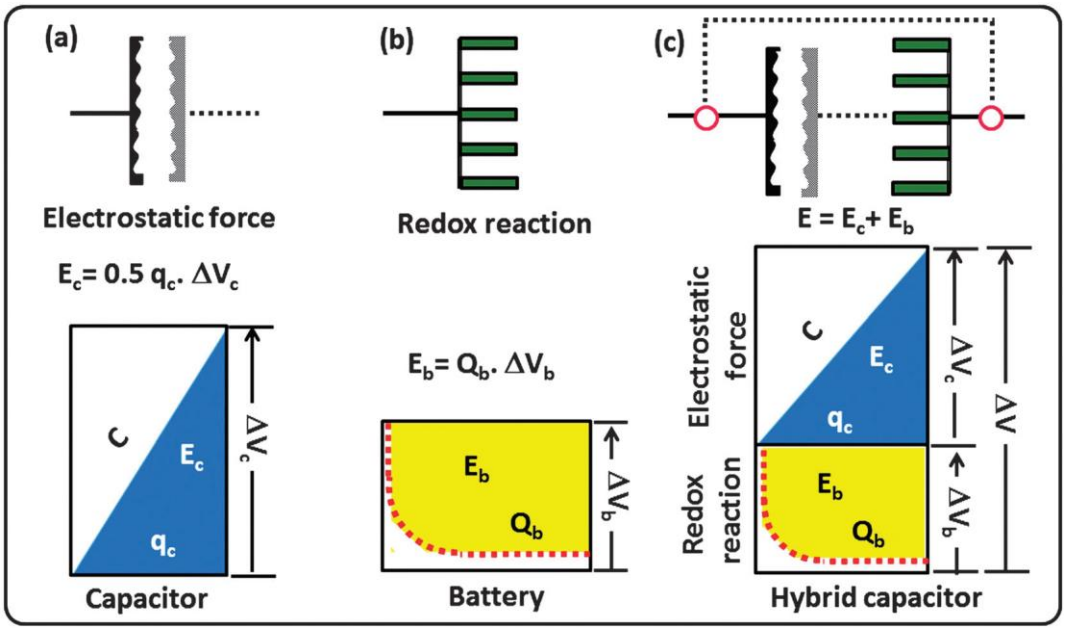

Figure 2-5. Schematic representations of a single electrode system (a), capacitor (b) battery and (c) an asymmetric capacitor system with an aqueous electrolyte according to the charge–potential profile with corresponding equations for energy storage. E is the energy density, q is the charge, and V is the voltage. (re-printed from Ref.[26] with permission from *Chemical Society Journal)*.

2.5 Development challenges

Blending the best characteristics of LIBs and SCs technologies have inspired researchers in the last decade. Despite the incremental advancements in developing novel materials for EDLC, materials with high surface area such as activated carbon and graphene remain the ideal material for the SC segment.[28,29] Therefore, researchers' efforts were mainly focused on investigating materials for the faradic factor of the HSC: including metal oxides, such as RuO_2,[30] MnO_2,[31] $Li_4Ti_5O_{12}$,[19] V_2O_5[32] and $Co_2O_{3;}$[33] metal sulfides, such as MoS_2,[34] $NiCo_2S_4$;[35] and, conducting polymers such as polyaniline[36] and polypyrolle.[37] However, despite the recent success in improving the energy density of the HSC, the low power density and limited cycle life are still challenging factors in hybrid supercapacitors.[17,22] The power density decays significantly because faradic materials can't adapt their reaction mechanism to gain/release charge near EDLC's high power rates . High current densities will force the faradic piece to charge/discharge quicker, which can accelerate the degradation of the faradic active material leading to poorer cycling performance and possible fire risk.[17]

To overcome these issues, two fundamental approaches can be utilized: 1) develop new nanostructure materials with modified characteristics and superior performance and, 2) design an asymmetric device with controlled charge reaction kinetics on both cathode and anode electrodes.

Chapter 3: Thesis Objectives and Strategy

3.1 Objectives and strategy

The ultimate objective of this work is to develop a new nanostructure faradic materials capable of delivering high energy densities and high power densities, with high stability and long life for hybrid supercapacitor applications. To accomplish this, a new strategy is implemented to improve material capacitance and operating voltage in order to increase the energy density and enhance material characteristics to improve the cycle life. This will be done simultaneously with careful control of the charge transfer kinetics on each side of the hybrid supercapacitor to maintain high power density. The thesis strategy is based on increasing the locations for charge storage and provide faster channels of charge transfer between the two sides of HSC. The hypothesis of this approach is based on developing nanostructure material capable of meeting the followings: 1) increased number of electroactive sites, 2) wide contact area between the active material and the electrolyte, 3) improved electrical conductivity, 4) shorten diffusion paths, 5) fast and more stable charge transfer kinetics and lastly, 6) ability to operate under high voltage range without material distortion.

To achieve this, it is important to identify the shortcomings of the selected materials and introduce influential and permanent changes to the intrinsic characteristics of the nanostructure materials to be capable of meeting all the above points in a harmonized synergy. An example is binary metal sulfide, which have shown to provide improved initial capacitance and higher conductivity than their oxide variants. However, binary metal sulfides nanoparticles such as $NiCo_2S_4$ (NCS), suffer from limited cyclability, material instability and

conductivity decay. Our strategic approach for improving this material is to insert a highly conductive element (vanadium) into the lattice of NCS, without affecting its chemical composition, while rooted on graphene nanosheets. This approach has led to remarkable changes in the material morphology; from 3D nanoparticles to 2D elongated nanosheets and the formation of ordered crystal-structured vanadium modified NCS nanosheets (VNCS) anchored on the surface of graphene nanosheets. This have resulted in superior electrochemical performance at high power rates, and remarkable stability over long cycling periods with high capacitance retention. Similar strategies were applied for other investigated materials, as discussed in the relevant chapters.

To reiterate, the specific objectives of the thesis are the followings:

- Design and development of unique nanostructure materials, capable of delivering energy densities higher than 20 Wh kg^{-1} at a power density around 1 kW kg^{-1}.
- Achieve long cyclability more than 5000 cycles with at least 70 % capacitance retention compared to the capacitance at the first cycles.
- The developed nanostructure materials should be capable of operating at high power rates without significant loss of capacitance.
- The use of simple, inexpensive and scalable synthesis methods to open the door for potential commercialization of these technologies.

The strategy and research process of this thesis is shown in **Figure 3-1**. The details of the used approach for each material is discussed in the relevant chapter.

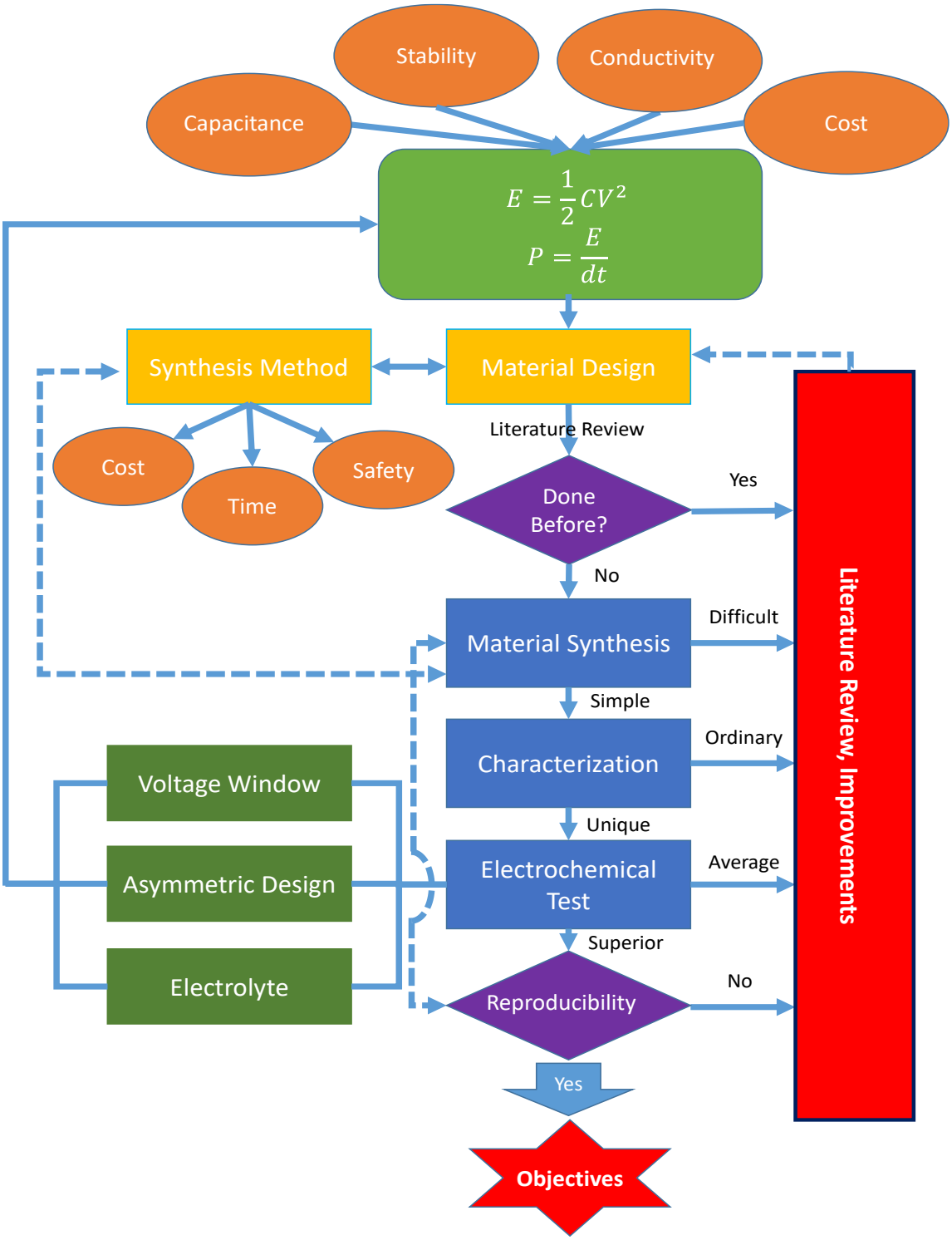

Figure 3-1. Schematic depicting the work flow strategy of this thesis.

3.2 Investigated solutions

The adopted strategy discussed in the previous section led to the development of three approaches to achieve the desired objectives. These three approaches shown in **Figure 3-2** include the development of the followings: 1) multigrain electrospun 1D nickel-doped lithium titanate nanofibers synthesized by a simple electrospinning process, 2) vanadium-modified 2D chalcogens rooted on 2D graphene nanosheets prepared by energy efficient and inexpensive solvothermal method, and 3) reconciled 2D and 3D vanadium disulfide anchored on 2D graphene nanosheets prepared by solvothermal method.

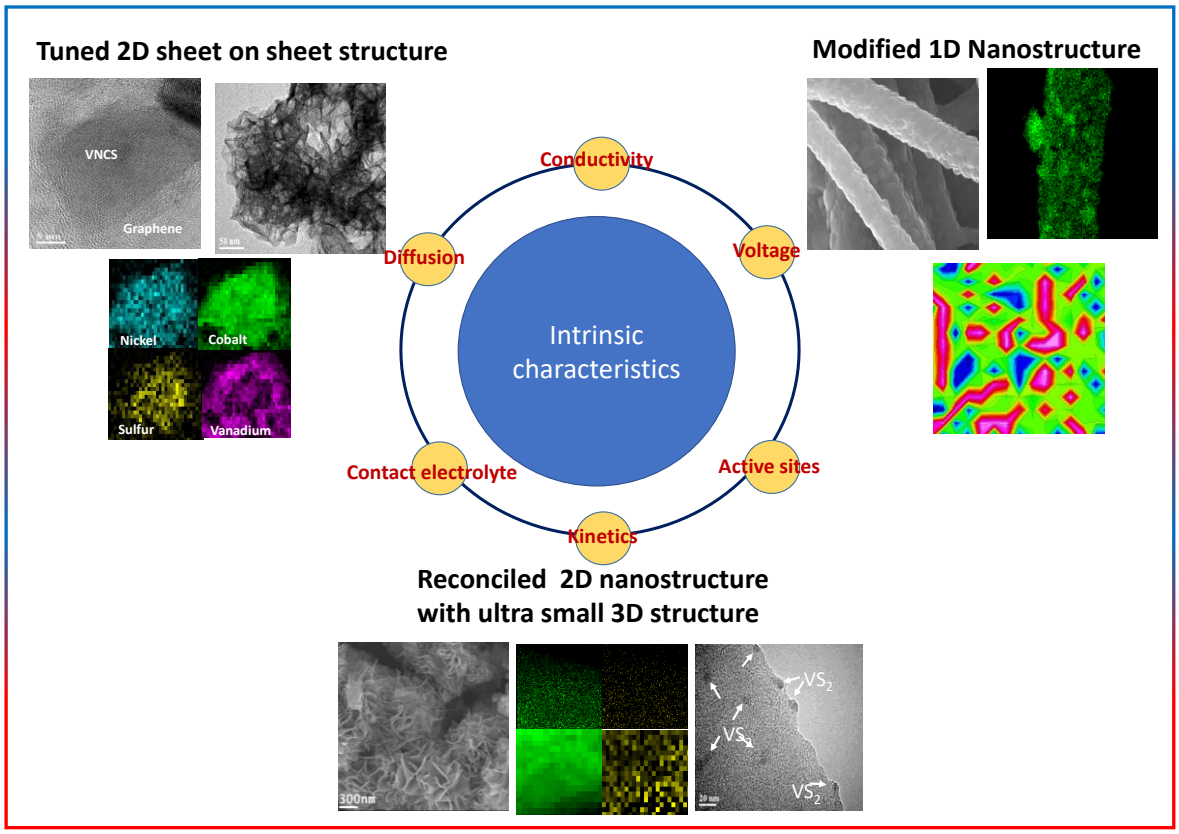

Figure 3-2. Schematic summary showing the three approaches used to develop advanced nanostructure materials meeting the objectives of this thesis.

3.3 Thesis outline

An introduction to the fundamentals of supercapacitors and lithium ion batteries is discussed in chapter 1. Chapter 2 provides information about hybrid supercapacitor fundamentals including structure, working principle and development challenges. Chapter 3 introduces the overall thesis objectives and provides a simplified breakdown of the project tasks. The proceeding chapters will provide detailed information about the work done throughout this thesis. Chapter 4 refers to the experimental procedures, characterization techniques and synthesis methods used in this work. Chapter 5 provides in-depth information about the development of unique 1D multigrain electrospun nickel-doped lithium titanate nanofibers. The development of novel modified 2D chalcogens with tuned nano-architecture rooted on 2D graphene substrate is discussed in chapter 6. Chapter 7 introduces the development of reconciled 2D vanadium disulfide nano-architecture with overlapped anatomy with 3D vanadium disulfide nanoparticles and anchored on 2D graphene nanosheets. Chapter 8 provides the conclusion and summary of the work done throughout the thesis and highlights recommendations for future work that can capitalize on the reported scientific achievements to build commercial HSC devices.

Chapter 4: Experimental Methods and Characterization Techniques

This chapter will introduce the theory of the synthesis methods, electrochemical testing and characterization techniques used in this work. The detailed experimental procedures, performance results and characterization analysis for each one of the developed materials are discussed in the proceeding chapters.

4.1 Synthesis methods

One of the main objectives of this work is the use of simple, scalable and inexpensive production methods. To achieve this, two synthesis methods were employed to produce the developed materials: electrospinning and solvothermal treatment.

4.1.1 Electrospinning

Electrospinning is a facile and low-cost method used to synthesize 1D nanofibers. Typical electrospinning system can be built easily (**Figure 4-1**) from four simple parts: 1) injection pump, 2) syringe containing the precursor solution, 3) power supply, and 4) metallic collector. The principle of electrospinning is based on applying a high voltage between an injected solution droplet and an opposing collector. Charge accumulation on the droplet surface causes electrostatic repulsion with the surface tension force which stretches the droplet to form what is known as Taylor cone.[38] When the applied voltage reaches a critical value, the force of the electric field overcomes the surface tension force and the fiber jet elongates and is deposited on a collector. Electrospinning is affected by a number of parameters, such as:[39,40] 1) solution viscosity and concentration, 2) applied voltage, 3) flow rate, 4) solution conductivity, and 5)

distance between the needle tip and the collector. The main advantages of electrospinning are: 1) low cost, 2) scalability, 3) simplicity of the experimental setup, and 4) the high surface area and small pore size of the synthesized fibers. The main disadvantages of electrospinning are 1) difficulty in obtaining uniform thickness of the fibers, 2) fiber disruption, and 3) formation of large beads.[39,40] It is important to use a sufficiently viscous polymer precursor solution and optimize the experiment parameters to overcome these disadvantages.[41]

4.1.2 Solvothermal

The solvothermal method is a simple, energy efficient and inexpensive process that allows for controlling the physical and chemical characteristics of the end product by controlling the reaction parameters. Solvothermal method refers to the use of organic solvent as a medium for a chemical reaction that involves heating to a temperature higher than the boiling point of the used solvent.[42] The reaction happens in a closed system, where all the reactants are placed in a Teflon liner that is inserted into a stainless steel autoclave. The autoclave is tightened and placed inside a heating oven. The solvothermal reaction occurs under moderate to high temperatures and pressures to magnify the interaction between precursors during synthesis. The design of the solvothermal synthesis procedure depends on a number of factors including:[43] 1) the physical and chemical properties of the used precursors such as solubility and thermal stability, 2) the physical and chemical properties of the used solvent such as viscosity, polarity and decomposition temperature, and 3) the percentage of the volume used in the Teflon liner; it is important not to exceed 80% of the total volume to avoid safety risks.

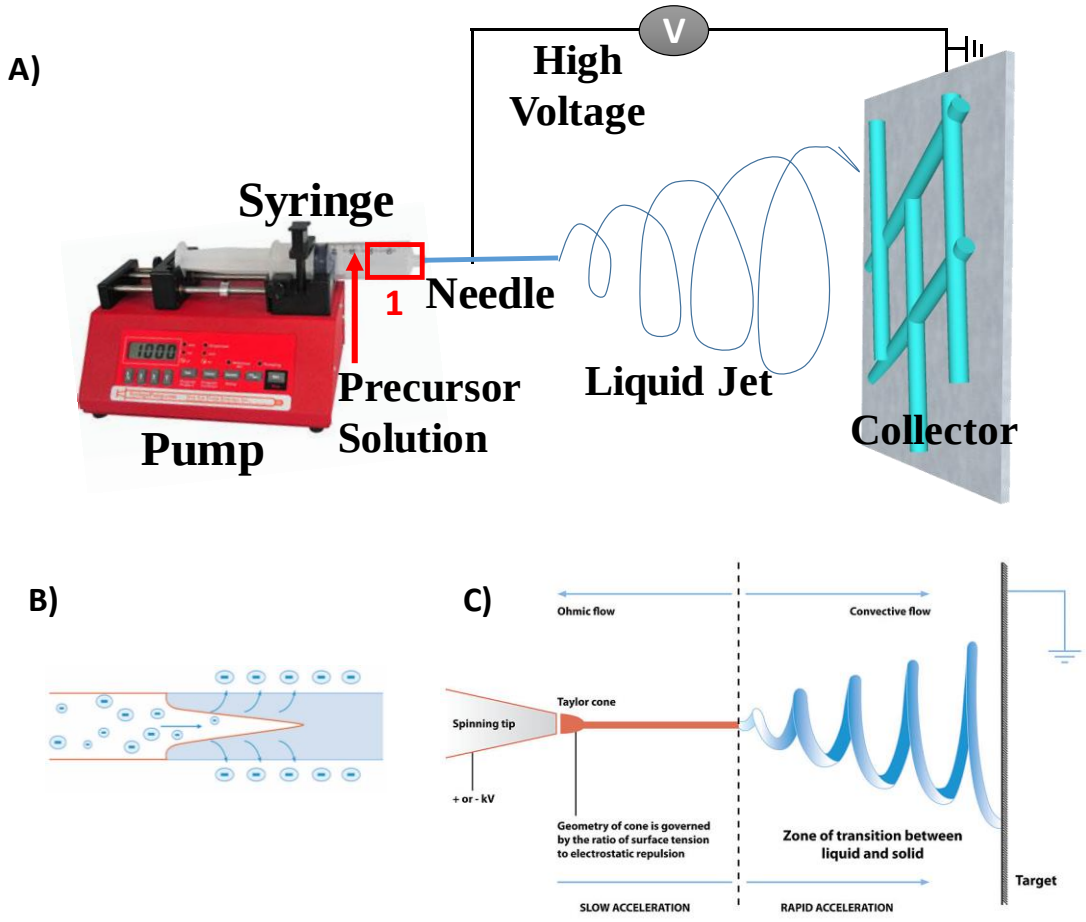

Figure 4-1. A) Schematic illustrating the electrospinning setup with the main four parts shown. B) Schematic representation showing the change in the distribution of charge as the droplets leaves the tip of the needle (area 1 in Figure A), and C) schematic showing the elongation of fibers and the competing forces. (*Figures B and C are obtained from Wikipedia https://en.wikipedia.org*)

4.2 Characterization techniques

Physicochemical characterization is important to understand the relationship between electrochemical performance and the characteristics of the developed materials (*i.e.* chemical composition, physical morphology and structure). Physicochemical investigation is a crucial step in the strategic loop used in this thesis. Understanding the effect of materials' structure and chemical composition on the electrochemical performance is essential to identify the shortcomings of the material. This can help in refining the design of the synthesis procedures. The following sections will introduce the theory and the importance of the used characterization techniques.

4.2.1 Scanning electron microscopy

Scanning electron microscopy (SEM) is a high resolution imaging technique (**Figure 4-2**) used to examine the morphology of materials in the micro and nano scales. The working principle of SEM involves directing a beam of short-waved electrons onto the surface of the inspected sample. The electron beam is generated from an electrons gun (two wires connected to high voltage source, 15-30 KVA), the beam is focused on the sample by set of electromagnetic lenses. When the electrons beam hit the sample's surface; secondary and backscattered electrons will be captured by detectors fixed above the sample. The electrons beam is raster scanned over the inspection area and the detected electrons will be converted into electrical signals which are processed by a data acquisition system to generate the final image of the inspected area.[44]

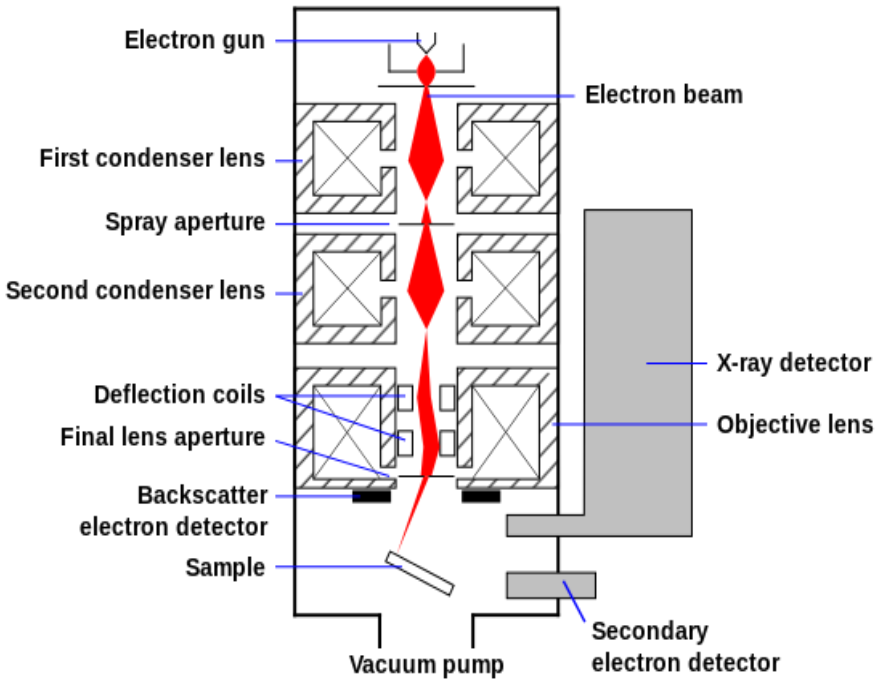

Figure 4-2. Schematic depicts the SEM with the main components shown. (*Source of image: Wikipedia https://en.wikipedia.org*)

4.2.2 Transmission electron microscopy

Transmission electron microscopy (TEM) is a very powerful imaging technique that provides in-depth information about the physical characteristics of the investigated sample at the nano and atomic scales. The working principle is based on directing electrons that are generated by field emission beam onto the sample. When the electrons reach the sample, they will be transmitted through the sample and captured by detectors. The captured electrons will be transformed into electrical signals and converted into high resolution images that can help visualize the material morphology and crystal orientation at the atomic level. TEM imaging techniques include low resolution TEM, high resolution TEM, selected area diffraction (SAD), high angle annular dark-

field scanning transmission electron microscopy (HAADF-STEM), elemental distribution mapping, and electron energy loss spectroscopy (EELS).[45]

4.2.3 Energy dispersive X-ray spectroscopy

Energy dispersive x-ray spectroscopy (EDS) is a quantitative and qualitative analysis technique that is used for the identification of the sample's chemical composition through elementals analysis. EDS is usually coupled with SEM and TEM and can be done simultaneously with imaging. The collision of the electrons with the sample will emit x-rays which can be captured by a detector. The analysis of the binding energy of the emitted x-rays versus reference fingerprints for different elements enables the identification and quantification of the material's chemical composition.[45]

4.2.4 X-ray diffraction

X-ray diffraction (XRD) is an important and fast analytical technique (**Figure 4-3**) that is used to identify the crystal structure of the investigated sample and provide information about unit cell dimensions. X-rays with specific wavelengths are emitted from a beam source at specific angle toward the inspected sample. When the x-rays bombard the sample, they will interact with the material atoms before being reflected with different intensities and creating a pattern. The diffracted x-rays will be collected by a detector and processed to generate spectrum which will be compared versus well known fingerprints for materials to identify the investigated material. The lattice spacing can be found using the relationship between the angle of diffraction and the specific crystal orientation using Bragg's law shown in the following equation:[46]

$$2d\sin\theta = n\lambda \qquad (4\text{-}1)$$

Where n is the order of the spectrum (integer number), λ is x-ray wavelength, d is the distance between the sample plane, and θ is the introduced x-ray angle to the surface of the material.

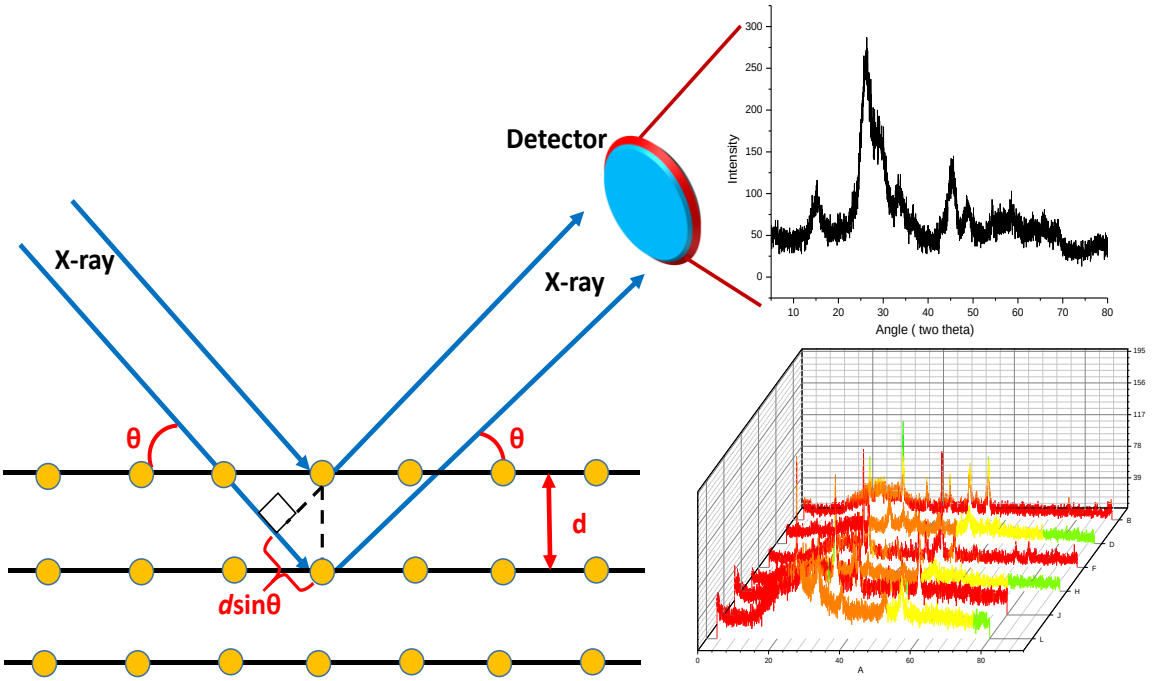

Figure 4-3. Schematic illustrating the XRD working principle and showing examples of the generated XRD pattern spectrums.

4.2.5 X-ray photoelectron spectroscopy

X-ray photoelectron spectroscopy (XPS) also known as electron spectroscopy for chemical analysis (ESCA) is a very powerful analysis technique that can provide qualitative and quantitative information about the investigated materials. XPS is a surface-sensitive technique capable of measuring the elemental composition at a very high precision for the atoms existing

at 0.5 to 10 nm from the surface of the sample. XPS provides detailed information about the chemical formula and chemical state of the materials. The working principle (**Figure 4-4)** is based on sending an X-ray with known energy to bombard the surface of the examined material causing vibrations in the atomic bonding and emissions of electrons. The emitted electrons are counted and their kinetic energy is measured. By calculating the change in total energy between the sent beam and the emitted electrons, the energy needed to excite and emit these electrons can be calculated, which will be equal to the binding energy of these electrons. The binding energy is characteristic of the atom type and chemical state.[47]

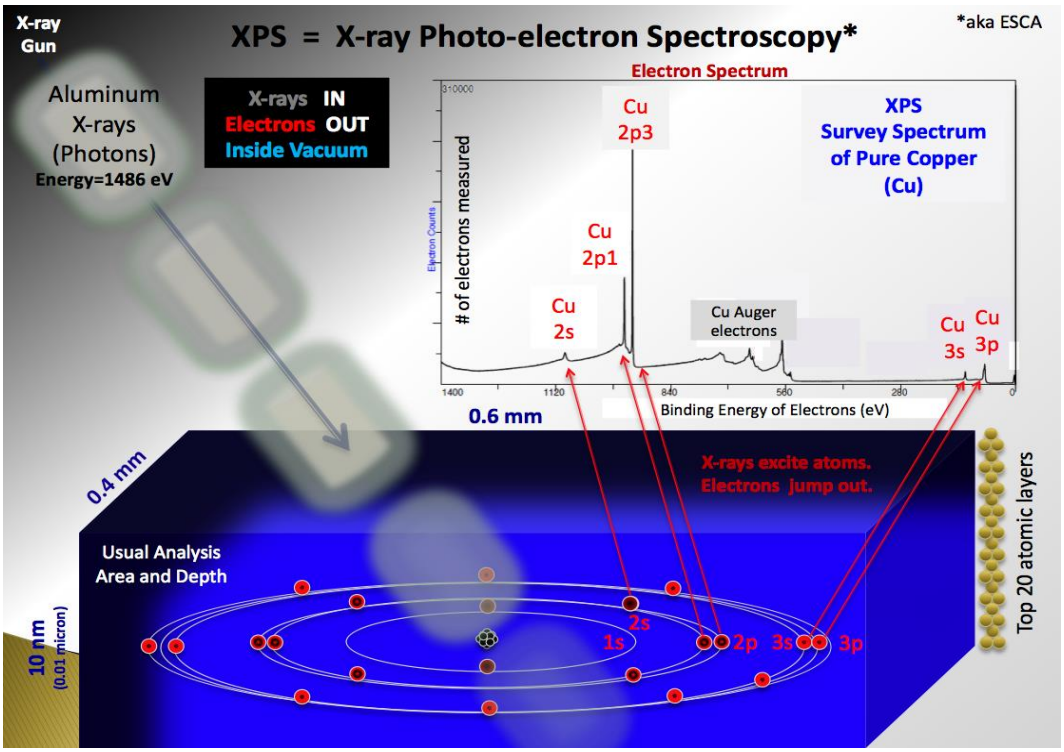

Figure 4-4. Schematic showing the working principle of XPS using copper as an example (*source of image: Wikipedia https://en.wikipedia.org*)

4.2.6 Thermogravimetric analysis

Thermogravimetric analysis (TGA) is an analysis technique that measures the change in the weight of the investigated sample versus temperature increase at fixed rate or versus time at fixed temperature. TGA can provide useful information about the composition of the tested sample as a function of mass loss or mass gain.[48]

4.2.7 Brunauer–Emmett–Teller

Brunauer–Emmett–Teller (BET) is a useful analysis theory that provides information about the specific surface area of the investigated materials. BET is based on measuring the physical adsorption of a nitrogen multilayer as function of relative pressure. The BET instruments are usually equipped with Barrett-Joyner-Halenda (BJH) pore size and volume analyzer that can provide information about the pore area and pore volume from the adsorption-desorption measurement.[49]

4.2.8 Raman spectroscopy

Raman spectroscopy is an analytical technique that can provide qualitative and quantitative information about the chemical composition of the investigated materials based on vibrational spectroscopy. The measurement theory is based on sending a laser monochromatic light at a known frequency onto the material and analyze the intensity of the scattered light. When the laser beam hits molecules in the material, a shift in energy will happen due to the interaction of light with the molecule causing shift in the vibrational energy levels of the excited molecules. Plotting the intensity of the shifted energies versus the frequency of the inbound light will

generate a spectrum that can be used to identify and quantify the investigated material using well known molecular fingerprints.[50]

4.3 Electrochemical performance testing

Number of techniques were utilized to evaluate the electrochemical performance of the developed materials throughout this work. These techniques include cyclic voltammetry, galvanostatic charge-discharge, rate capability, and durability test. This section will introduce the testing theories.

4.3.1 Cyclic voltammetry (CV)

Cyclic voltammetry (CV) is a potentiodynamic electrochemical evaluation technique that is based on sweeping the potential of the working electrode between two voltage limits at a fixed voltage scan rate. In a typical CV experiment (**Figure 4-5A**), the potential of the working electrodes will be increased at specific scan rate until reaching certain potential value. Once the targeted potential value is reached, the process will be reversed and potential will be reduced at the same scan rate until reaching the lower potential value. The process of voltage sweep will create a voltage difference between the working electrode and the counter electrode which will force electrons to move back and forth between the two electrodes generating current in the external circuit. The resulting current, voltage, and time are recorded and analyzed which provide valuable information about the characteristics of the material such as the redox behaviour, reversibility, specific capacitance, charge transfer kinetics, and material stability.[51]

4.3.2 Galvanostatic charge-discharge

Galvanostatic charge-discharge (CD) is a well-established measurement technique that can provide useful information about the electrochemical characteristics of the cell. The test protocol is based on charging and discharging the working electrode at a fixed current density within a specific voltage window. In a typical CD experiment, when the working electrode is charged or discharged at fixed current density, the amount of charge transferred between the electrodes will remain constant. The change in potential and time are measured and varied based on the current density that is applied. The analysis of the voltage and time dynamics with current density can provide useful information about electrochemical characteristics of the investigated materials. The specific capacitance can be calculated from the charge-discharge curve (**Figure 4-5B**) as per the below equation:[19,52]

$$\mathbf{C_S = I /(m\ \Delta V/\ \Delta t)} \qquad \mathbf{(4\text{-}2)}$$

Where C_S is the specific capacitance (F g^{-1}), I is the discharge current (A), m is the mass of the active material (g) and $\Delta V/\Delta t$ is the discharge curve slope (V s^{-1}) obtained after the voltage drop.

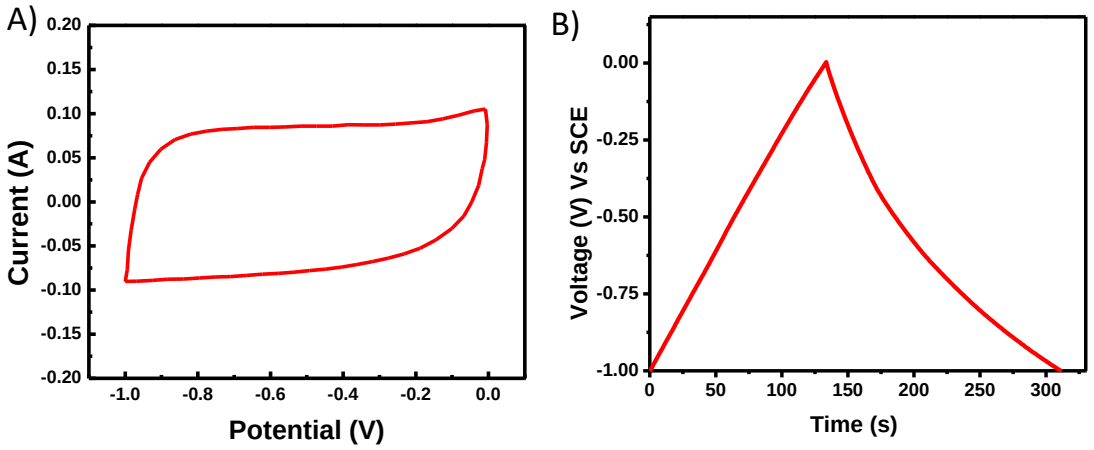

Figure 4-5. Two examples of electrochemical performance evaluation techniques. A) cyclic voltammetry (CV), and B) charge-discharge (CD). The investigated material is activated carbon. (reprinted from Ref.[53] with permission from the Royal Society of Chemistry)

4.3.3 Rate capability

Rate capability refers to the evaluation of the electrochemical performance at various current densities versus the theoretical values of the material or versus performance at low current densities. The analysis of the rate capability behaviour provides useful information about the electrochemical characteristics of the material. For example, retaining high capacitance at high current rates is an indication of the material's high stability and fast charge transfer kinetics. Such material can be good candidate for HSC applications.[52]

4.3.4 Galvanostatic cycling

Galvanostatic cycling or durability test is done by repeating the charge-discharge operation at a fixed current density for a large number of cycles. Every charge and discharge loop is considered as one cycle. The electrochemical performance will be measured after each cycle and compared

to the performance of the first cycle. Durability test is also an indication of stability and reaction reversibility.[52]

4.3.5 Electrochemical impedance spectroscopy

The impedance can be defined as the opposition to current flow or voltage change.[52] Electrochemical impedance spectroscopy (EIS) provides information about the resistance of electrodes and electrolyte, as well as the charge transfer process. EIS measures the impedance of the cell over a range of frequencies.

4.4 Test configurations

Two types of cell configurations were used throughout this work; two-electrode system and three-electrode system. The following section provides insight into each system.

4.4.1 Two electrode cell

Two-electrode setup is a simple configuration to measure the electrochemical performance of the developed materials. It is constructed by placing the two electrodes opposite to each other and separated by membrane and electrolyte. One of the electrodes will be the working electrode under investigation and the other electrode will act as counter and reference electrode at the same time.[52] In this work, we used the two electrodes system to construct a coin cell inside a glove box when organic electrolyte is used.

4.4.2 Three electrode cell

Three electrode system is a basic analysis configuration that is used to study the electrochemical behavior of the investigated material when it is important to fix the potential at the

material/electrolyte interface in order to obtain a high precision measurement. Three electrode setup can be easily used with aqueous electrolytes due to the possibility of running the electrochemical evaluation under regular room conditions. Typical three electrode cell (**Figure 4-6**) consists of working electrode (WE), counter electrode (CE) and reference electrode (RE) immersed in an electrolyte solution. The investigated material is deposited on the working electrode. The role of the CE is to ensure that current will not flow through the RE and change its potential. Depending on the type of electrochemical test, the change in current or potential that happen due to the transfer of charges between the WE and CE will be recorded versus standard values of the reference electrode.[52]

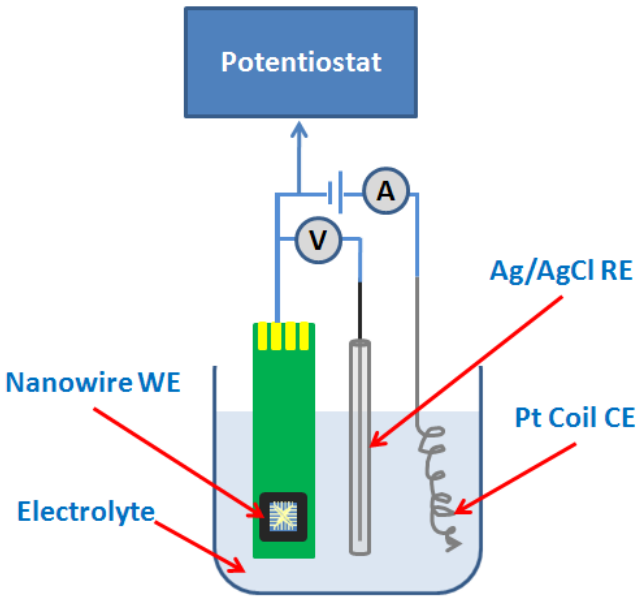

Figure 4-6. Schematic depicting the three-electrode electrochemical evaluation setup. This example uses nanowire WE, Ag/AgCl as RE, and Pt. coil as CE. (reproduced from Ref.[54] with permission from The Royal Society of Chemistry)

Chapter 5: Multigrain Electrospun Nickel Doped Lithium Titanate Nanofibers with High Power Lithium Ion Storage

This chapter is reprinted in adjusted format from Ref.[19], with permission from the Royal Society of Chemistry:

Salah Abureden, Fathy M Hassan, Gregory Lui, Wook Ahn, Serubbabel Sy, Aiping Yu, and Zhongwei Chen, "Multigrain Electrospun Nickel Doped Lithium Titanate Nanofibers with High Power Lithium Ion Storage", Journal of Material Chemistry A, 2016,4, 12638-12647

5.1 Chapter introduction

The developments of portable electronics, electric vehicles, and smart grids are increasing the need for reliable energy storage devices with safe operation and high power capabilities.[2,3] Lithium ion batteries (LIBs) have been studied extensively in the past years as one of the most promising candidates for these applications. However, the current graphite-based electrode technologies used in LIBs suffer from limited power capabilities and safety concerns.[4] To address these challenges, researchers have investigated a number of alternative materials. Spinel lithium titanate (LTO) is one type of material that is chosen for its safety, high power density, and rate capability which stem from its outstanding ability to accommodate lithium ions without significant structural change during charge and discharge operations (zero-strain).[55,56] The theoretical capacity of LTO is 175 mA h g^{-1} with a stable plateau at 1.55 V versus Li/Li^+. This relatively high voltage minimizes the chance of lithium dendrite formation and electrolyte decomposition which usually occur at lower voltages, causing cell failure and

possibly fire due to cell overheating. Although LTO has remarkable characteristics, its electrochemical performance and practical applications are still limited due to its poor electron conductivity and low energy density.[57] Different approaches have been investigated to overcome these limitations such as carbon coating, particle size reduction, and transition metal doping.[4,55] Carbon coating improves conductivity and rate capability of LTO, while particle size reduction shortens the lithium diffusion path which improves intercalation kinetics and improves battery capacity.[55] Doping with transition metals has been found to enhance conductivity and lithium ion diffusivity leading to higher capacity and improved rate capability.[58] Researches in metal doping have been focused mainly on lithium titanate nanoparticles (LTONP), nanowires, and nanotubes. [59-67]

Nickel is a highly abundant and inexpensive dopant that has the potential to improve the performance of LTO-based LIBs. Investigations on nickel doped LTO nanoparticles were conducted in the past. In some studies, nickel doped LTO nanoparticles were found to increase the initial capacity of the battery.[68,69] Other studies found marginal improvement in the rate capability performance of nickel doped LTO nanoparticles synthesized using different methods, including hydrothermal and solid state reaction.[56,70] Co-doping LTO with nickel and manganese was reported to improve capacity and cycling performance.[71] These investigations led to the development of advanced LTO materials. However, their improvements were incremental and no remarkable combined advancements in both rate capability and energy density have been reported yet.

On the other hand, 1D nanofibers are very attractive because they can be easily produced by low cost and facile electrospinning, which makes the electrospun nanofibers highly scalable for large batch production. The 1D nanofibers can be very good choice for LIBs applications because 1D nanofibers show good strain relaxation, shorter Li^+ diffusion paths, interfacial control, and continuous electron transport pathways, which are all very favorable for improving LIB performance.[4,72-75] Number of studies reported using 1D nanofibers in LIBs[59,76,77], however, nickel doped into LTO one-dimensional nanofibers has not yet been investigated and reported in literature[78]. In this chapter, we report successful in-situ doping of nickel into 1D lithium titanate nanofibers (LTONF) using facile and scalable electrospinning technique followed by a heat treatment. We investigated three Ni to LTO molar ratios; 0%, 5% and 10%. It is worth mentioning that 15% doping ratio was not possible at similar electrospinning parameters as the other three doping ratios. This can be attributed to the effect of the additional nickel on the precursor solution conductivity and charge density at the surface of the injected solution droplet. Increasing the nickel amount increases the solution conductivity and charge density beyond the critical value, which hinders the creation of Taylor cone required to initiate the elongation of fiber jets.[79,80]

Our strategy in this work reporting nikel doping to LTO nanofibers for the first time is based on dual improvements for both electronic conductivity and lithium diffusivity of LTO in order to simultaneously enhance rate capability as well as energy density of the LIB. The advantage of our approach is the simplicity and unique coupling of in-situ nickel doping distributed homogenously into the stable 1D LTO nanofibers lattice. The obtained promising results can

open the door for more research in the use of nanofibers for LIB applications. A performance comparison of nickel doped LTO nanofibers with previous studies is shown in **Table A-1** in **Appecnix A**.

The pure LTONF sample with x=0 is referred to as LTONF, the sample with x=0.05 is referred to as Ni-LTONF$_5$, and for x=0.1, the samples is referred to as Ni-LTONF$_{10}$. While LTO nanoparticles is referred to as LTONP

5.1.1 Experimental procedure

All materials were purchased from Sigma Aldrich and used without further purifications. The used precursor solution and the electrospinning experiment setup is shown in **Figure 5-1**.

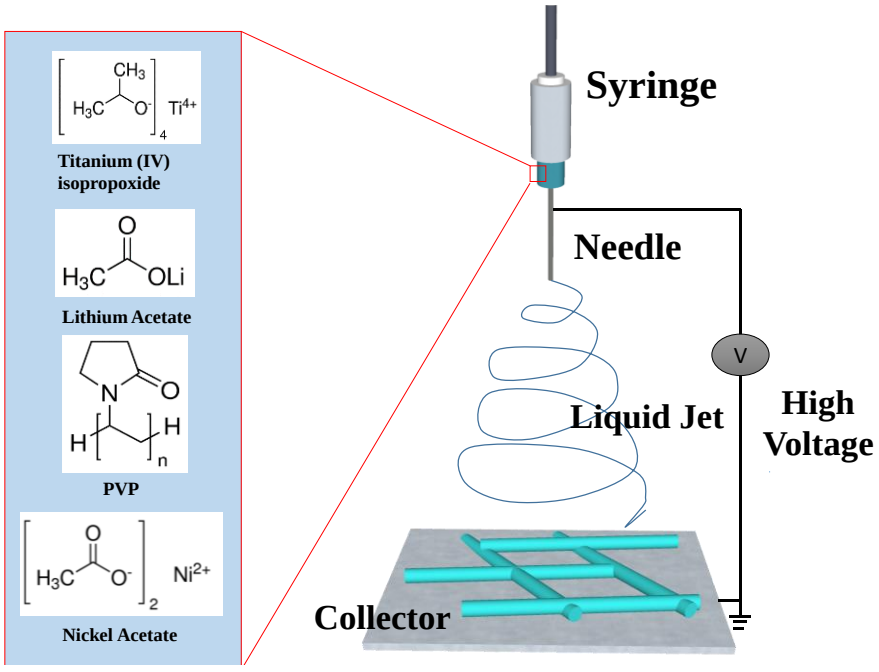

Figure 5-1. Schematic depicting the used precursor solution and electrospinning setup. (reproduced in adjusted format from Ref.[19], with permission from the Royal Society of Chemistry)

5.1.1.1 Synthesis of LTO nanofibers

0.95 g titanium(IV) isopropoxide ($Ti[OCH(CH_3)_2]_4$), 0.1855 g lithium acetate dihydrate ($LiC_2H_3O_2 \cdot 2H_2O$), and 0.51 g poly-vinylpyrrolidone (PVP, MW=1.3 M) were all added to a vial containing 8.5 ml pure ethanol and 2.5 ml acetic acid. The solution was stirred for 6 hours on a hot plat at 35^oC and 1150 rpm. The precursor solution was then moved to a 14.1 mm plastic syringe with metallic needle attached to a high voltage source (19.0 kV). The needle tip was placed 14.5 cm from an aluminum foil current collector and the flow rate was set to 0.15 ml h^{-1}. The collected fibers were moved to a quartz tube and annealed inside a tubular furnace at 780^oC in air for 5 hours (3^oC min^{-1}) to remove all organic materials. Finally, the sample was left to cool naturally before collecting the end product

5.1.1.2 Synthesis of Ni-LTO nanofibers

Nickel doped LTO nanofibers were synthesized by adding (drop wise) a proper amount of nickel acetate solution dissolved in 2 ml ethanol to the precursor solution described in the LTONF synthesis. The rest of steps followed the same procedure as LTONF synthesis. The investigated materials include pure LTO nanofibers (LTONF) and two nickel to LTO mole ratios (1:20 and 1:10)

5.1.1.3 Synthesis of LTO nanoparticles

LTO nanoparticles were synthesized by combining stoichiometric amounts of lithium carbonate (Li_2CO_3) and titanium dioxide (TiO_2) in a planetary ball mill using a 125 ml grinding jar and zirconium balls. The material was ball milled for 12 hours under 300 RPM. The resulting fine powder was then heat-treated at 780^oC at air to produce LTO nanoparticles

5.1.1.4 Cell fabrication

The electrochemical tests of LIBs were conducted by fabricating the electrode materials into coin cells. Each coin cell was made of a working electrode, separator and lithium foil electrode in an organic electrolyte medium. The working electrodes was prepared by mixing the synthesized material with carbon black (super P) using a mortar and pestle for 30 minutes. Polyvinylidene fluoride (PVDF) binder was then added, and the mixture ground again for 20 minutes. The ratio of synthesized material, super P, and PVDF was 80:10:10. N-methyl-pyrrolidone (NMP) solvent was added to make a slurry which was coated on a 1 cm^2 copper current collector. The loading for all electrodes was approximately 1.0 mg cm^{-2}. The coated electrodes were dried at 80^oC for 2 hours followed by overnight drying in a vacuum oven at 110^oC in order to remove all the NMP solvent.

The HSC cells were fabricated from Ni-LTONF_{10} material as the anode, separator and commercial activated carbon (AC) as the cathode. The anodic electrode of HSC was prepared using 80 wt.% active material, 10 wt.% carbon black, and 10 wt.% PVDF binder. Coin cells for both LIBs and HSC were assembled in a glove box filled with argon. 1M lithium hexafluorophosphate ($LiPF_6$) in ethylene carbonate and dimethyl carbonate (EC-DMC 1:1 volume) was used as the electrolyte

5.1.2 Physicochemical characterization

The crystal structure of the samples were characterized by X-ray diffraction (XRD, RIETVELDXRG 3000) and X-ray photoelectron spectroscopy (XPS, PHI Quantera) located at the Ontario Center for Characterization of Advanced Materials (University of Toronto). BET

analysis was performed after samples were degassed at 200°C for two hours under vacum. 2D raman mapping was examined using Senterra 2 Bruker Raman instrument. Sample morphology was examined using scanning electron microscopy (SEM, ZEISS ULTRA PLUS), Raman spectroscopy (SENTERRA 314) and transmission electron microscopy (TEM, JEOL 2010F TEM/STEM field emission microscope) at the Canadian center for electron microscopy (CCEM) located at McMaster University.

The XRD pattern of all samples are shown in **Figure 5-2A**, the results show that all patterns are almost identical. The sharp diffraction peaks located at $2\theta = 18.6^{o}$, 37^{o}, 43^{o}, 58^{o}, and 63^{o} correspond to (111), (311), (400), (511), (440), and (531) planes, respectively. These peaks represent single phase spinel LTO with the Fd3m space group (JCPDS card number 49-0207) which reveals that calcination at 780 °C in air obtains well crystallized LTO with no indication of impurities. The crystallization process has significant effects on LIB performance because crystallinity and material purity affects both lithiation kinetics and lithiation capacity. Studies have shown that the initial crystallinity of TiO_2 can have an effect on the crystallization and purity of $Li_4Ti_5O_{12}$.[81,82] Amorphous materials tend to hinder lithiation because of its disordered structure, while crystalline materials allow more facile lithiation.[82] Although the precursor nanofibers used are structurally amorphous because of low temperature hydrolysis of titanium alkoxide naturally leads to the formation amorphous TiO_2. Heat treatment of amorphous TiO_2 will form a crystalline phase of TiO_2 and then undergo solid-state conversion to crystalline phase of $Li_4Ti_5O_{12}$ via lithiation by the lithium source.[81,82] The similarity in XRD patterns of doped and pure samples also indicate that nickel doping has not obviously changed the crystal

structure of LTONF. However, broader peaks are found in LTONF, Ni-LTONF$_5$, and Ni-LTONF$_{10}$ XRD patterns compared to the LTONP XRD pattern. This difference is attributed to the crystal refinement of the nanofibers samples resulting from a difference in synthesis method. To verify the doping effect of nickel, the specific peak corresponding to the (111) plane for LTONF and Ni-LTONF$_{10}$ is magnified and shown in **Figure 5-2B**. Ni-LTONF$_{10}$ shows a slight shift in the diffraction peak of (111) plane to a lower angle ($2\theta = 18.51^{o}$) compared to the diffraction peak of pure LTONF ($2\theta = 18.6^{o}$). This decrease indicates that the lattice parameter of Ni-LTONF$_{10}$ is slightly higher than that of pure LTONF. This is attributed to the size of nickel (0.69 Å) being slightly larger than titanium (0.60 Å).[61,70,83] The shift in the diffraction peak is additional evidence for the successful doping of nickel which can be also observed in the change of colour of the end product. As seen in the inset of **Figure 5-2B**

The lattice parameters of the pure and doped LTO nanofibers are calculated by mathematical calculations using the following equations: [84,85]

$$\mathbf{2d\,(\sin\Theta) = n\lambda} \qquad \mathbf{(5\text{-}1)}$$

$$\mathbf{1/d^2 = (h^2+k^2+l^2)/a^2} \qquad \mathbf{(5\text{-}2)}$$

Where d is the distance between the atomic layers, θ is the beam angle, n is integer number of wavelengths (1), λ is the wavelength of the incident beam. h, k, l are Miller indices and a is lattice parameter. The lattice parameters are found to be 8.366 Å, 8.373 Å and 8.379 Å for LTONF, Ni-LTONF$_5$ and, Ni-LTONF$_{10}$, respectively. The slight increase in the lattice parameter with increasing doping percentage is attributed to the slight expansion of the lattice due to the partial substitution of titanium with nickel which is also confirmed by XPS results.

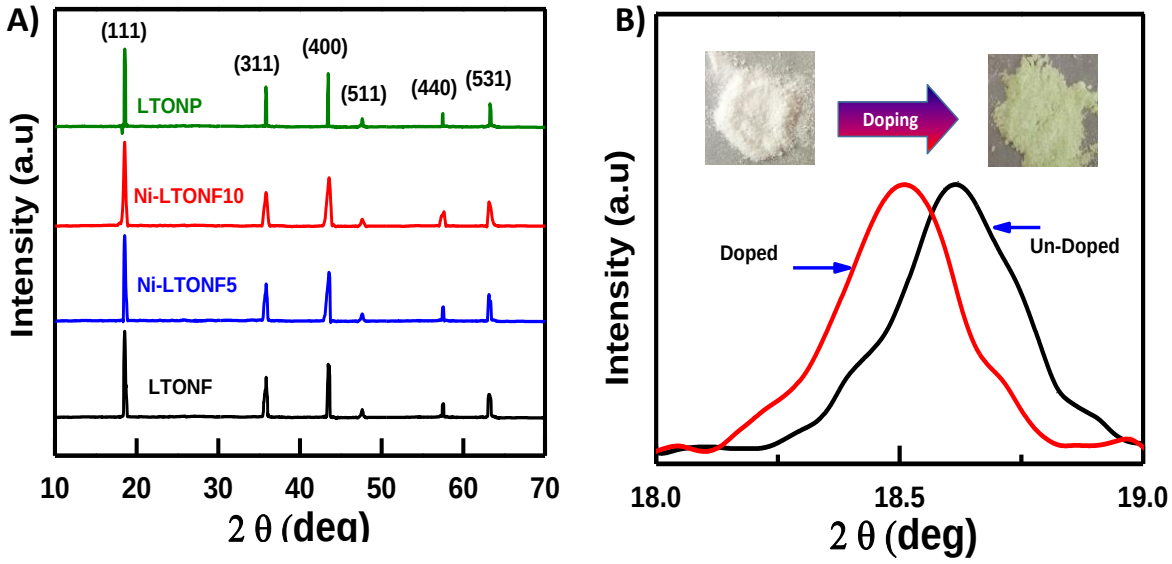

Figure 5-2. A) XRD patterns of LTONP, LTONF, Ni-LTONF$_5$, and Ni-LTONF$_{10}$ and, B) magnification of the XRD peak corresponding to the (111) plane of LTONF and Ni-LTONF$_{10}$ showing a negative peak shift due to nickel doping. The inset shows optical images of LTO nanofibers before and after doping. (reprinted in adjusted format from Ref.[19] , with permission of the Royal Society of Chemistry)

X-ray photoelectron spectroscopy (XPS) was utilized to investigate material composition before and after nickel doping of LTONF as shown in **Figure 5-3A** shows the general XPS spectra of three LTO nanofiber samples, while **Figure 5-3B** shows magnification of the XPS Ti2P peaks. The un-doped LTONF shows two peaks at 458.54 eV and 464.31 eV corresponding to the $2p_{1/2}$ and $2p_{3/2}$ peaks of Ti^{+4}. The peaks were shifted to a lower energy level after nickel doping with 458.21 eV and 463.91 eV for Ni-LTONF$_5$ and 458.07 eV and 463.82 eV for Ni-LTONF$_{10}$ which reveal the effect of nickel doping on changing the valence state of Ti ions from Ti^{+4} to Ti^{+3} leading to enhanced electrochemical properties as well documented in literature. [66,86,87]

The composition change of the LTO nanofibers before and after doping is summarized in **Table 5-1**. The results reveal that nickel doping causes the formation of $Li_4Ti_{(5-x)}Ni_xO_{12}$ (x=0.05 and 0.1) which explains the capacity increase of doped LTO at low current density compared to un-doped LTO

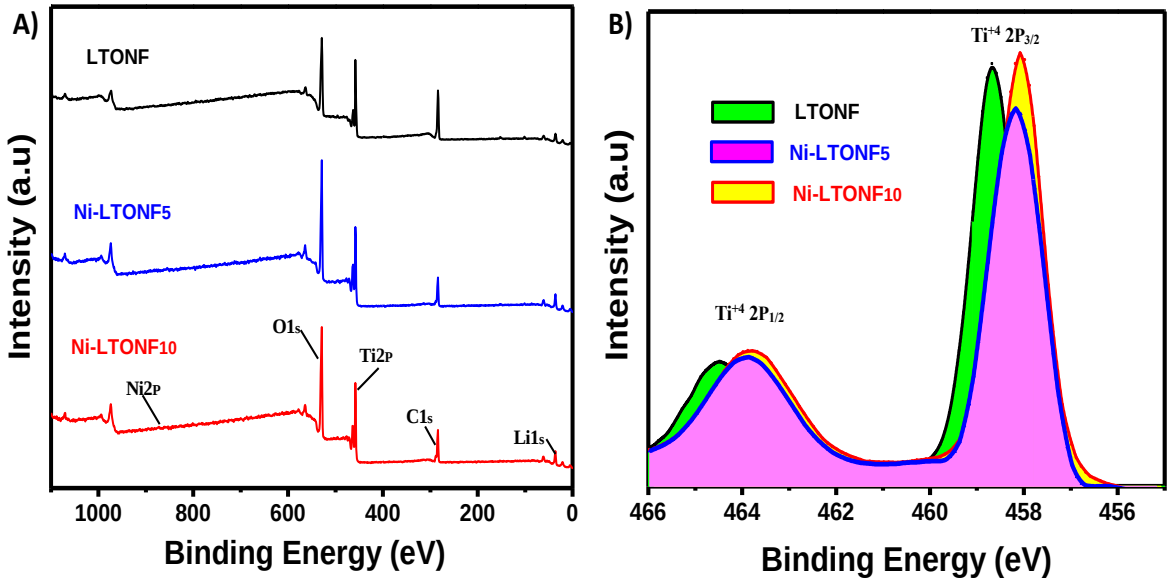

Figure 5-3. A) General XPS spectra of LTONF, Ni-LTONF$_5$ and Ni-LTONF$_{10}$ and, B) magnification of XPS Ti2p peaks of LTONF, Ni-LTONF$_5$ and Ni-LTONF$_{10}$. (reprinted from Ref.[19] , with permission of the Royal Society of Chemistry)

Table 5-1 Elemental composition (atomic percentage) of the LTO nanofibers samples. (reprinted from Ref.[19] , with permission of the Royal Society of Chemistry)

	LTONF	i-LTONF5	-LTONF10
ım %	19.28	19.047	19.02
ium %	22.75	23.57	23.23
en %	57.97	57.14	57.06
l %	0	0.24	0.49

The BET analysis of the three LTO nanofibers samples were measured. **Figure 5-4** shows the nitrogen adsorption/ desorption isotherm curves and the pore size distribution. The surface area for the three sample are found to be almost similar, with surface areas of 8.22, 8.55 and, 7.96 $m^2 g^{-1}$ for LTONF, Ni-LTONF$_5$, and Ni-LTONF$_{10}$, respectively. The average pore size diameter are found to be 5.9, 8.5 and 7.6 nm for LTONF, Ni-LTONF$_5$, and Ni-LTONF$_{10}$, respectively. The similarity in surface area and pore size are more indications that the improvement in electrochemical performance is mainly driven by nickel doping.

The SEM images of LTONF, Ni-LTONF$_{10}$ before and after calcination in addition to LTONP are shown in **Figure 5-5**. The nanofibers samples show continuous, fibrous morphology, with a diameter in the range of 700-800 nm before calcination and 300-400 nm after calcination. This reduction in diameter is due to the removal of PVP. The diameter of Ni-LTONF$_{10}$ is in the range of 750-850 nm before calcination which is reduced to 350-450 nm after calcination. The diameter of Ni-LTONF$_{10}$ before and after calcination maintained an average range of 50-100 nm difference in diameter compared to LTONF. Furthermore, both of the materials after calcination show homogeneous surface roughness, indicating that the granular-like structure

of primary nanoparticles of LTONF maintains a fiber-like structure. This 1D nanofiber structure obtained after calcination at 780°C is suitable for excellent lithium ion diffusion and electrical conductivity as demonstrated by significantly enhanced LIB performance shown later. The SEM images of LTONP confirm the nanoparticles morphology with a particle size range of 100-250 nm.

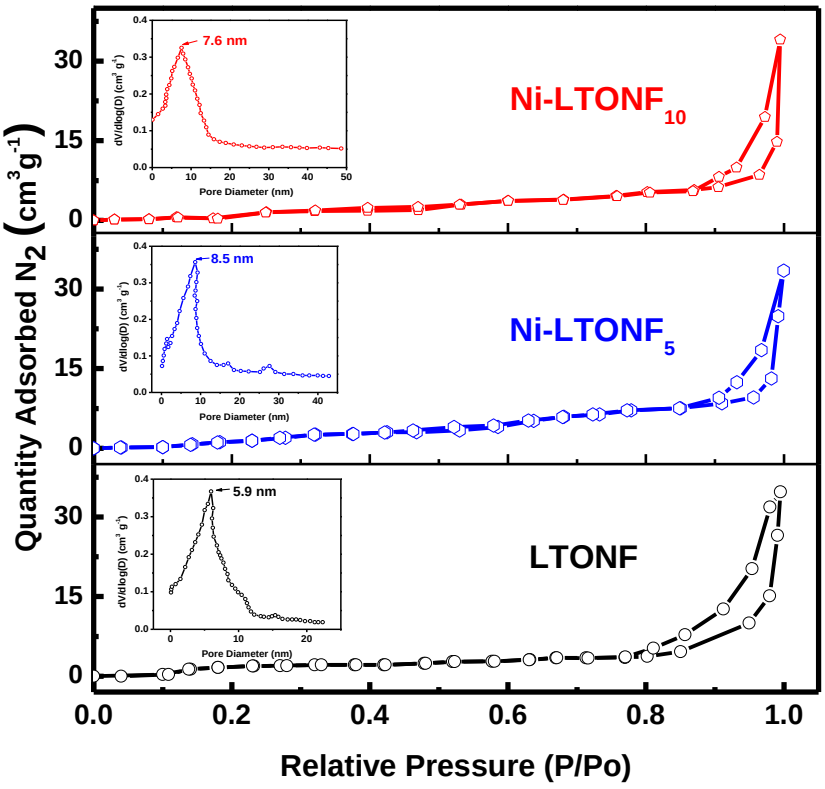

Figure 5-4. Nitrogen adsorption- desorption isotherm curves, the inset of each curve shows the pore size distribution curve. (reprinted from Ref.[19] , with permission of the Royal Society of Chemistry)

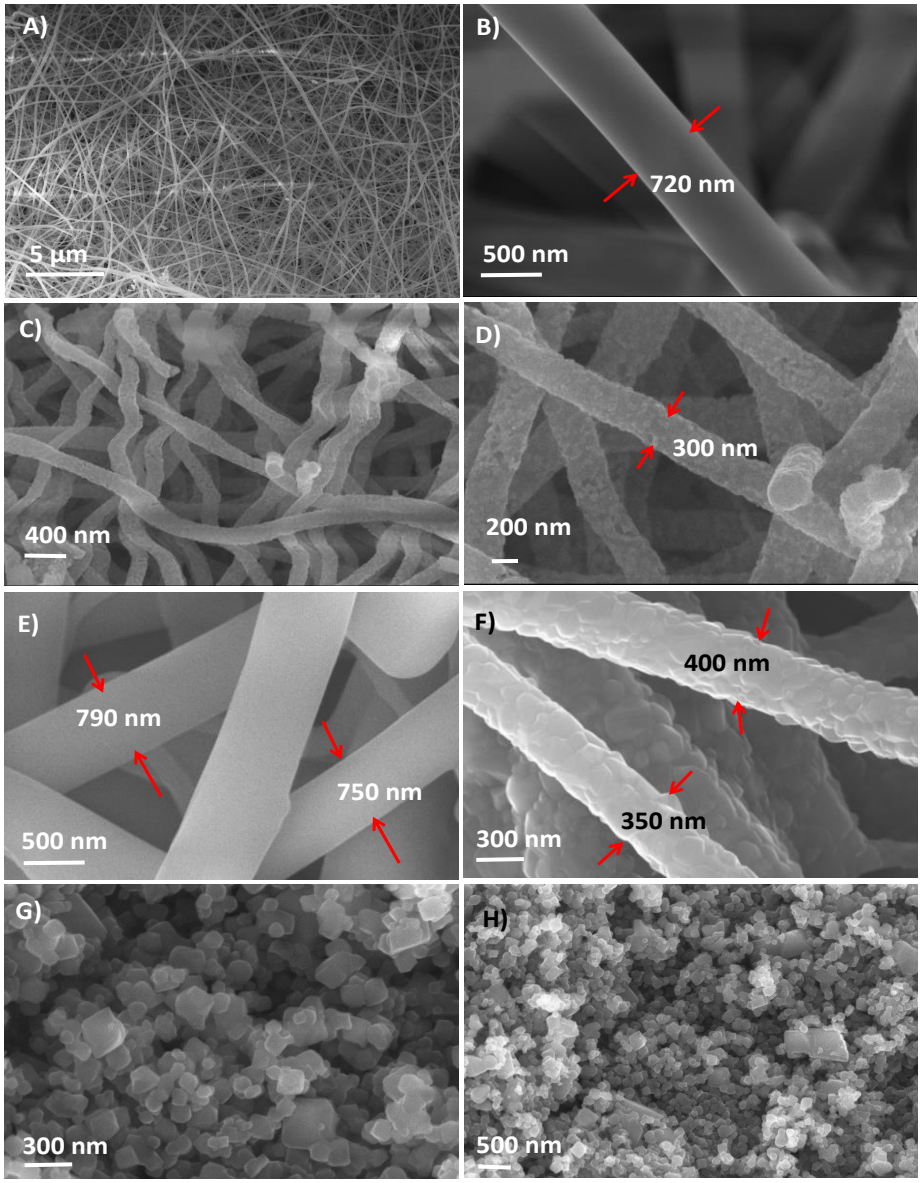

Figure 5-5. A-B) SEM image of electrospun LTONF before heat treatment at low and high magnifications, C-D) SEM images of the LTONF after heat treatment at low and high magnifications, E-F) high magnification SEM images of Ni-LTONF10 before and after heat treatment and, G-H) SEM images of LTONP after heat treatment. (reprinted from Ref.[19] , with permission of the Royal Society of Chemistry)

The TEM image of Ni-LTONF$_{10}$ are shown in **Figure 5-6**. **Figure 5-6A** show the 1D morphology with aligned multigrain of nanoparticles. The lattice fringe fingerprint of HRTEM shown in **Figure 5-6B** indicates that the crystalline structure of Ni-LTONF$_{10}$ with a preferential orientation to plane (111). The polycrystalline structure of the material is revealed in the SAED pattern shown in **Figure 5-6C**. The EDS images shown in **Figure 5-6 (D-G)** are based on high angle annular dark-field scanning transmission electron microscopy (HAADF-STEM) of one nanofiber. Combined with EDS line scan analysis shown in **Figure 5-6K** with the corresponding elemental distribution. Elemental characterization clearly confirms the homogenous distribution of nickel into the lattice of LTO. Electron energy loss spectroscopy (EELS) is a technique that shows atomic resolution of the elemental composition. The EELS mapping for part of the wire in **Figure 5-6D** is shown in **Figure 5-6 (H-J)**, further confirming the uniform distribution of nickel into the lattice of LTO (each pixel in these figures is equivalent to 6 nm x 6 nm). TEM images of Ni-LTONF$_5$ shown in **Figure A-1 (Appendix A)** also confirmed the homogenous distribution of all elements into the lattice of the 1D nanofibers.

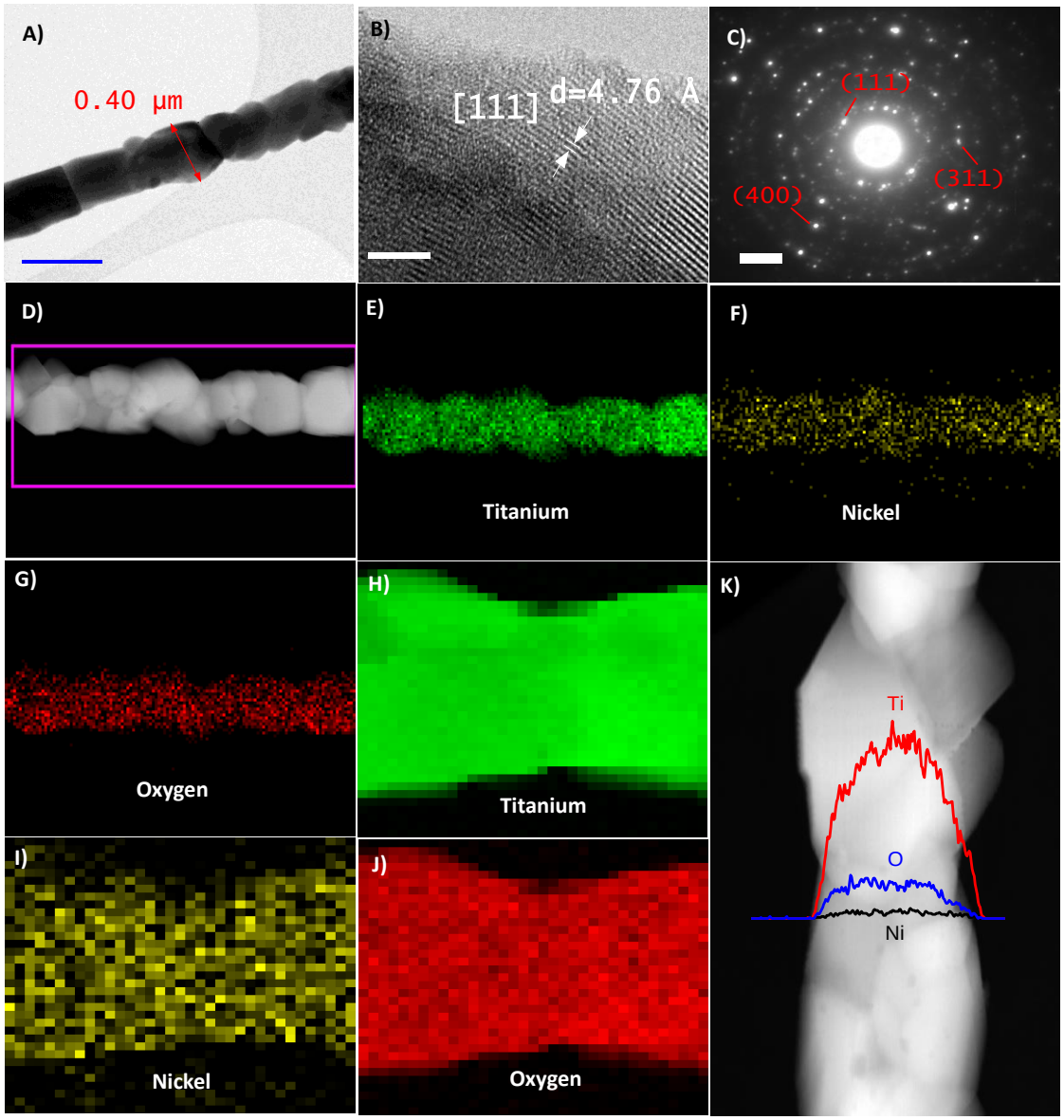

Figure 5-6. A) TEM images of Ni-LTONF10, B) high resolution TEM image of Ni-LTONF10, C) selected area electron diffraction pattern of Ni-LTONF10, D) HAADF-STEM image of Ni-LTONF10, E-G) EDS mapping of the nanofiber in (D) showing the elements titanium, nickel and oxygen, respectively, H-J) electron energy loss spectroscopy mapping of the labelled part in (D) showing the elements titanium, nickel and oxygen, respectively, and K) EDS line scan showing the elements profile across Ni-LTONF$_{10}$, (reprinted from Ref.[19] , with permission of the Royal Society of Chemistry)

5.1.3 Electrochemical performance

The LIB low current density charge-discharge tests were evaluated in potential range of (1- 2.5) V at room temperature using 0.2 C rate as shown in **Figure 5-7A**. LTONP has an energy capacity of 129 mA h g^{-1} while pure LTONF shows 149 mA h g^{-1} reversible capacity. Ni-$LTONF_5$ shows a higher capacity of 164 mA h g^{-1} while Ni-$LTONF_{10}$ shows excellent improvement with 190 mA h g^{-1} reversible capacity which is not only higher than LTONP, LTONF, and Ni-$LTONF_5$, but also higher than the theoretical capacity of LTO (175 mA h g^{-1}). **Figure 5-7B** shows the cyclic voltammetry test which was done in a voltage window of (1-2.5) V and scan rate of 0.5 mV s^{-1} for the 1D LTO electrospun samples to identify the change in redox behavior due to nickel doping. LTO is known to have a reduction peak at around 1.4 V and oxidation peak around at 1.7 V. The experimental results of LTONF show reduction and oxidation peaks similar to the standard LTO peaks indicating high crystallinity of the prepared sample.

Increasing nickel doping causes changes in the redox behavior of the tested materials. The oxidation peaks of the three materials are located at 1.71 V, 1.67 V, and 1.625 V and the reduction peaks are located at 1.43 V, 1.53 V, and 1.52 V for the LTONF, Ni-$LTONF_5$, and Ni-$LTONF_{10}$, respectively. **Table 5-2** shows the voltage hysteresis (ΔV) between the reduction and oxidation peaks of the three samples. Ni-$LTONF_5$ shows 50% reduction in ΔV compared to LTONF while Ni-$LTONF_{10}$ shows outstanding reduction in voltage hysteresis with a value three times smaller than LTONF and sharper redox peaks. These changes indicate improved

lithium diffusion kinetics due to the significant reduction in electrode polarization which allows for much faster rate in lithium uptake and release.[69,88,89]

Figure 5-7C shows the rate capability tests of LTONP, LTONF, Ni-LTONF$_5$ and Ni-LTONF$_{10}$ evaluated in potential range of (1- 2.5) V at room temperature using different current densities. The capacity fading for LTONP was very fast with increasing the C rates, showing only 25 mA h g^{-1} at 5 C only and below 5 mA h g^{-1} at 20 C, the capacity approached zero at C rates higher than 20 C. LTONF also suffered from fast capacity fading as LTONP but with better performance of 48 mA h g^{-1} at 20 C and below 5 mA h g^{-1} at 50. Ni-LTONF$_5$ showed improved performance compared to LTONP and LTONF with 81 mA h g^{-1} at 20 C and 38 mA h g^{-1} at 50 C**.** Lastly, Ni-LTONF$_{10}$ showed outstanding rate capability performance at high C rates with 116 mA h g^{-1} at 20 C and 63 mA h g^{-1} at 50 C.

Table 5-2. The oxidation and reduction peaks of the three samples with the voltage calculated hysteresis. (reprinted from Ref.[19] , with permission of the Royal Society of Chemistry)

	Oxidation	Reduction	ΔV
NF	1.71	1.43	0.29
NF$_5$	1.67	1.53	0.14
NF$_{10}$	1.62	1.52	0.1

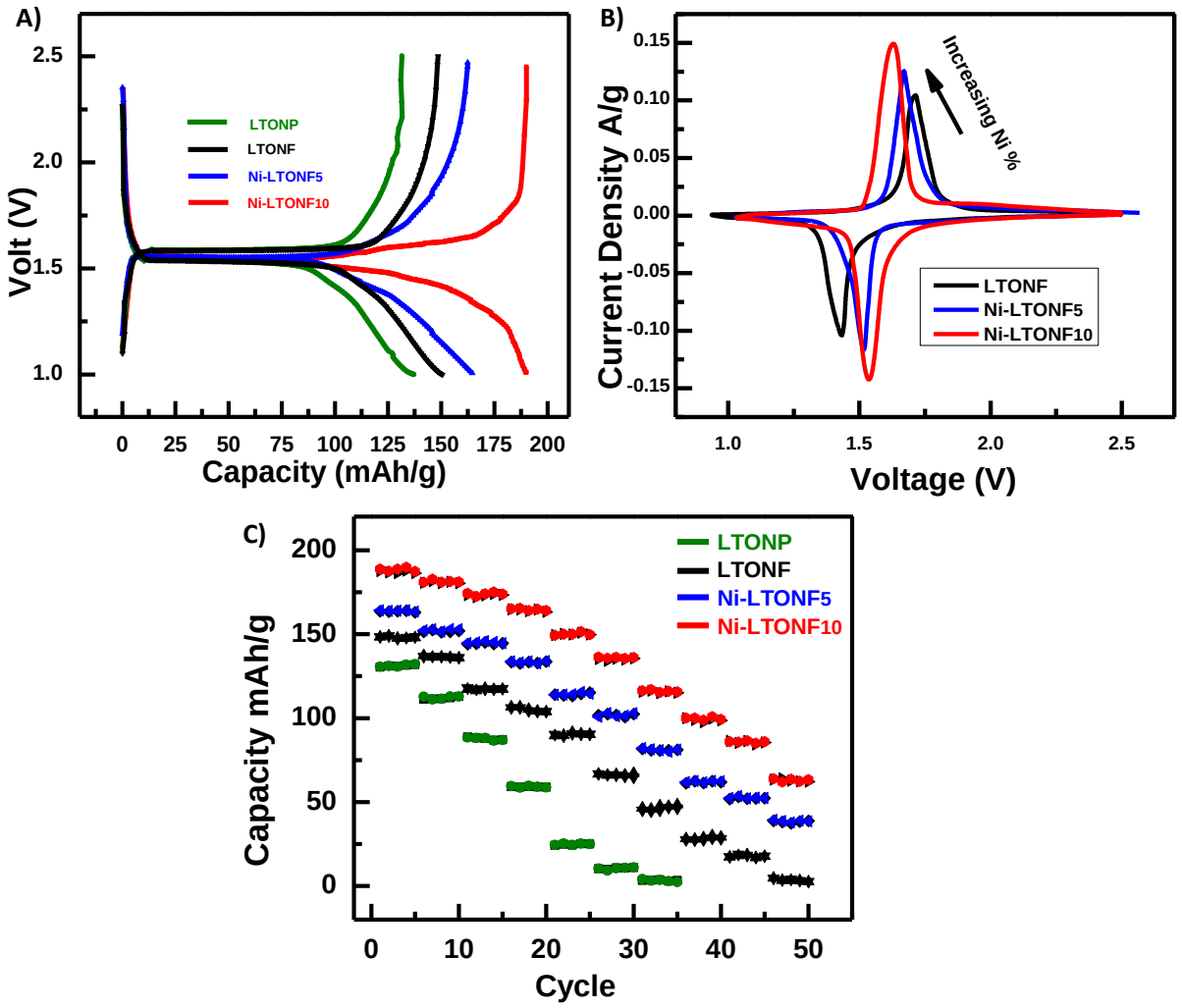

Figure 5-7. A) Galvanostatic charge-discharge profiles of LTONP, LTONF, Ni-LTONF5, and Ni-LTONF10. B) Cyclic voltammetry showing changes in redox behavior of the LTO nanofiber materials with increase in nickel doping and, C) Rate capability of LTONP, LTONF, Ni-LTONF5 and Ni-LTONF10 measured at different current densities. (reprinted from Ref.[19] , with permission of the Royal Society of Chemistry)

A comparison between the performance of LTONF and Ni-LTONF$_{10}$ at low and high C rates is shown in **Figure 5-8A**. The result shows that the performance of Ni-LTONF$_{10}$ at 50 C is 20 times higher than LTONF. **Figure 5-8B** shows a comparison of the discharge capacity values of the 1D nanofiber LTO materials at different C rates as function of their discharge capacities at 0.2 C. The results prove that Ni-LTONF$_{10}$ maintains higher values at all C rates.

For further investigation on the effect of nickel doping on the durability and cycling behavior of the 1D nanofiber materials, the long cycling performance was evaluated at 10 C as shown in **Figure 5-8C**. LTONF maintains a discharge capacity of 57 mA h g^{-1} after 1000 cycles which corresponds to 85 % of the first discharge capacity (67 mA h g^{-1}). Ni-LTONF$_5$ maintains 90.6 mA h g^{-1} discharge capacity, corresponding a capacity retention of 89% (101.8 mA h g^{-1}). Ni-LTONF$_{10}$ shows the highest performance after 1000 cycles with 126.8 mA h g^{-1} discharge capacity corresponding to a capacity retention of 94% (134.9 mA h g^{-1}) and an average capacity loss per cycle equivalent to 8.09 x 10^{-3} mA h g^{-1}.

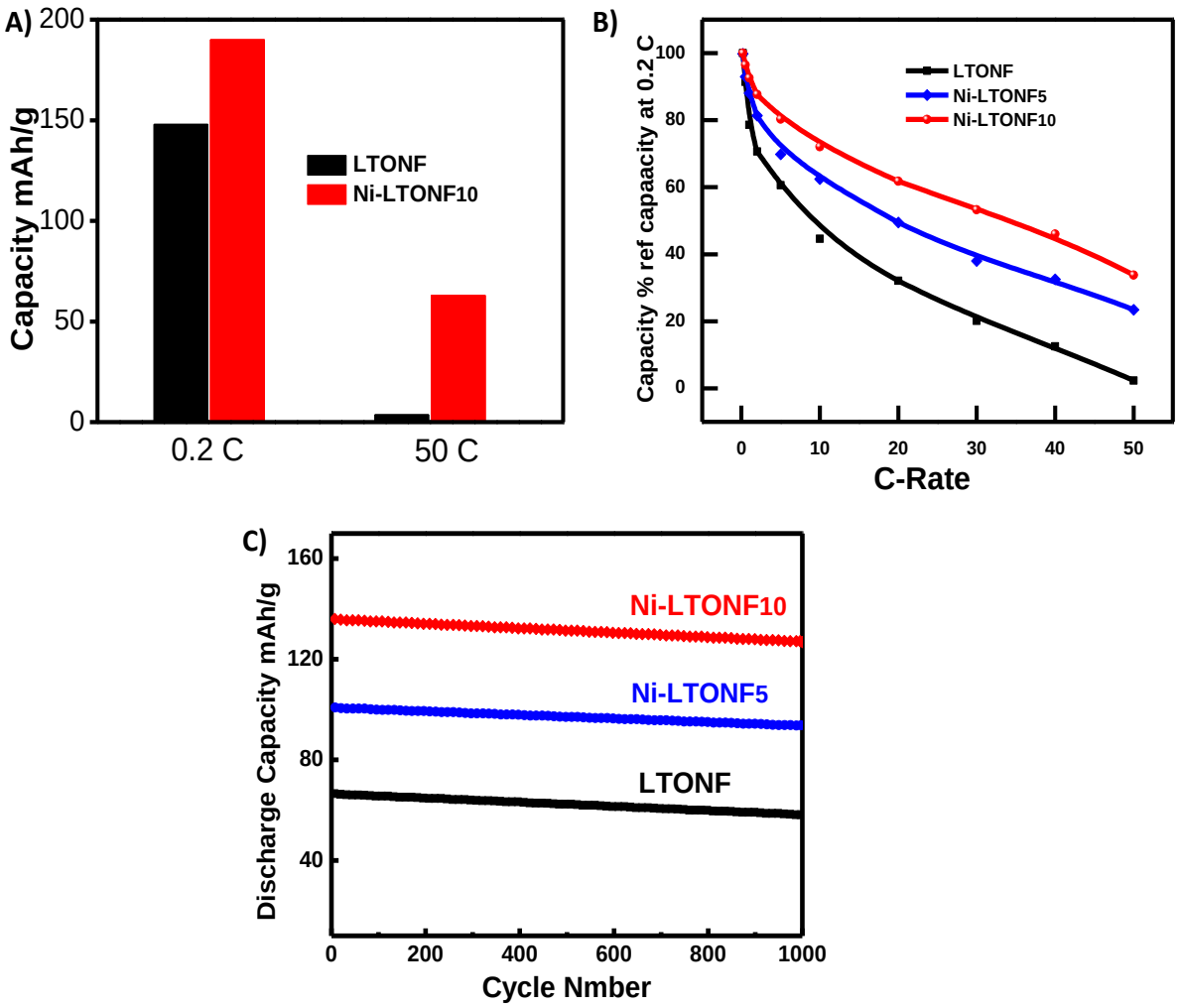

Figure 5-8. A) The performance of LTONF and Ni-LTONF10 at 0.2 C and 50 C showing the significant improvement of nickel doping at high C rates. B) Rate performance of LTONF, Ni-LTONF5, and Ni-LTONF10 at different C rates normalized to capacity at 0.2 C and, C) Long term (1000 cycles) of LTONF, Ni-LTONF$_5$, and Ni-LTONF$_{10}$ at 10 C current density. (reprinted from Ref.[19] , with permission of the Royal Society of Chemistry)

2D Raman mapping was utilized to investigate the stability of the 1D nanofibers morphology of un-doped LTONF and Ni-LTONF$_{10}$ before and after long cycling at high power rate (10 C). **Figure 5-9 (A-B)** show the un-doped nanofibers before cycling at the electrode surface and at 10 µm depth, respectively, while **Figure 5-9 (C-D)** show the un-doped nanofibers at the surface and at 10 µm depth after long cycling. **Figure 5-9 (E-F)** show Ni-LTONF$_{10}$ nanofibers before cycling at the electrode surface and at 10 µm depth. **Figure 5-9 (G-H)** show Ni-LTONF$_{10}$ nanofibers at the surface and at 10 µm depth after long cycling. The results show that 1D longitudinal nanofiber morphology was not damaged after long cycling for both doped and un-doped samples. The stable morphology of both electrode materials after long cycling at the surface and at the deepest point of the electrode indicates that the difference in the ability to maintain improved electrochemical performance between doped and un-doped samples is not attributed to morphological change or electrode deterioration of LTONF from long cycling at 10 C but rather to the effect of nickel in enhancing lithium intercalation thermodynamics for LTONF$_{10}$

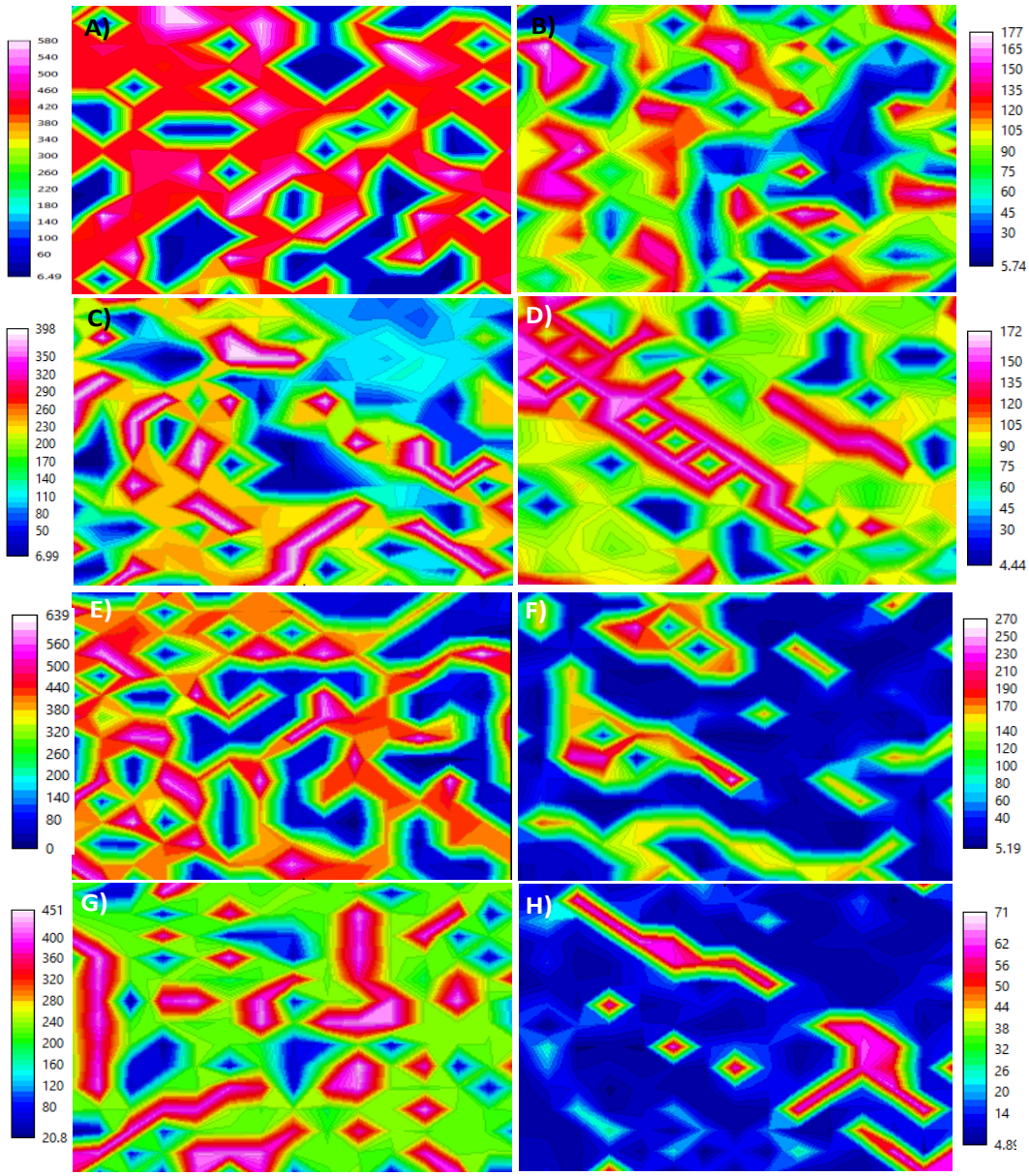

Figure 5-9. 2D Raman mapping for LTONF and Ni-LTONF10 electrode, A-B) LTONF before cycling at the surface and at 10 µm, respectively, C-D) LTONF after cycling at the surface and 10 µm, respectively, E-F) Ni-LTONF10 before cycling at the surface and at 10 µm, respectively and, G-H) Ni-LTONF$_{10}$ before cycling at the surface and at 10 µm, respectively. (reprinted from Ref.[19] , with permission of the Royal Society of Chemistry)

Electrochemical impedance spectroscopy (EIS) was employed to understand the effect of nickel doping on the lithium diffusivity and electrical conductivity. **Figure 5-10A** shows Nyquist plot of the impedance spectra for the three LTO nanofiber materials. All plots have a semicircle in the high frequency region and straight line in the low frequency zone. The low frequency zone is attributed to the diffusion of the lithium ions into the bulk of the electrode. **Figure 5-10B** shows the relationship between real impedance and the reciprocal square root of the lower angular frequencies $\omega^{-0.5}$. Lithium diffusion coefficients are calculated based on the following equations: [90,91]

$$\mathbf{Z_{re} = R_s + R_{ct} + \sigma_w . \omega^{-0.5}} \qquad \mathbf{(5\text{-}3)}$$

$$\mathbf{D = 0.5(RT/An^2F^2 \sigma_w C)^2} \qquad \mathbf{(5\text{-}4)}$$

Where R_s is the electrolyte resistance, R_{ct} is the charge transfer resistance at the surface of the active material, σ_w is Warburg impedance coefficient ($\Omega\ s^{-0.5}$), ω is the angular frequency in the low frequency region ($\omega = 2\pi f$), D is the diffusion coefficient, R is the gas constant, T is the absolute temperature, F is Faraday's constant, A is the area of the electrode surface, and C is the molar concentration of Li^+ ions in 1 cm^3

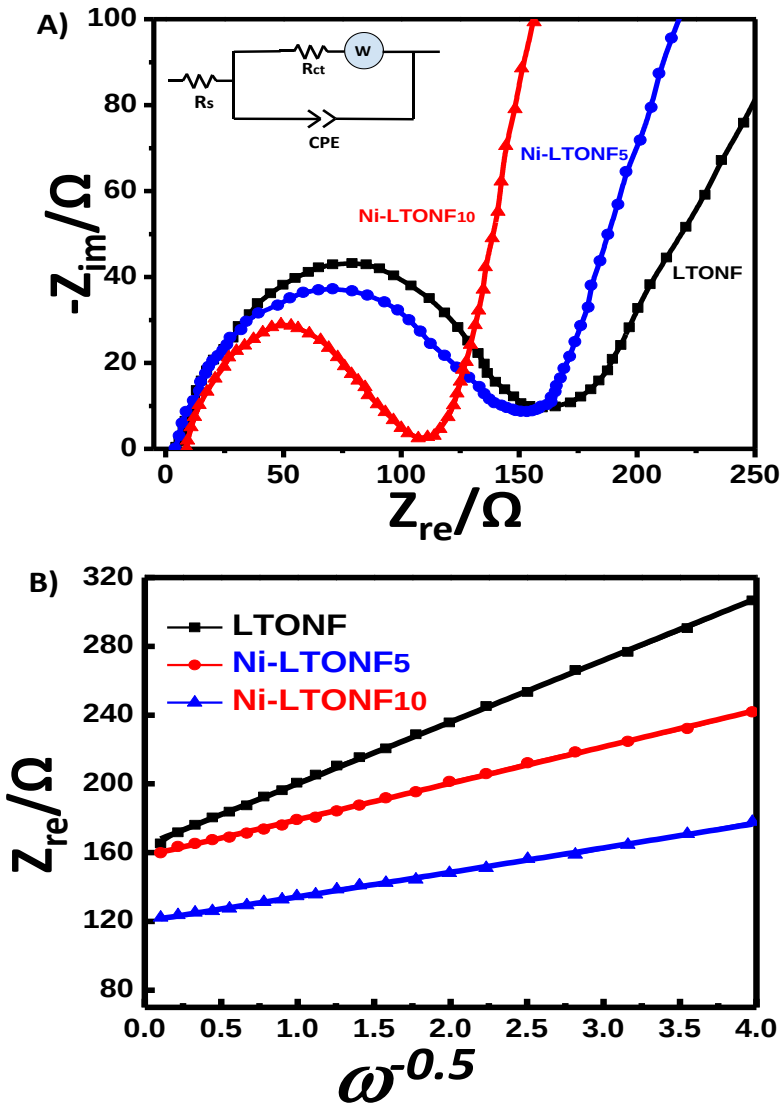

Figure 5-10. A) Nyquist plots of LTONF, Ni-LTONF5 and Ni-LTONF10 measured before cycling with the equivalent circuit shown in the inset, and B) the relationship between real impedance and $\omega^{-0.5}$. (reprinted from Ref.[19] , with permission of the Royal Society of Chemistry)

Table 5-3 shows a summary of the calculated values of R_s , R_{ct}, σ_w and D. Ni-LTONF$_{10}$ shows 5.86 x 10 $^{-12}$ cm^2 s^{-1} which is significantly higher (17 times) than that of pure LTO (3.43 x 10 $^{-13}$ cm^2 s^{-1}). The results clearly show the effect of nickel doping on improving the lithium diffusion coefficient and enhancing the overall electrochemical performance of the LTO nanofibers.[91]

Table 5-3. EIS parameters of the three LTO nanofiber samples (reprinted from Ref.[19] , with permission of the Royal Society of Chemistry)

	LTONF	Ni-LTONF5	Ni-LTONF10
Rs (Ω)	4.26	4.18	5.317
Rct (Ω)	160.1	153.08	114.29
σw ($\Omega S^{-0.5}$)	35.91	21.2	14.22
D (cm^2/S)	3.43 X 10^{-13}	9.67 X 10^{-13}	5.86 X 10^{-12}

5.1.4 Full cell HSC

For further investigation, we fabricated an asymmetric hybrid supercapacitor (HSC) cell made of Ni-LTONF$_{10}$ material as the anode and commercial activated carbon (AC) as the cathode. The specific surface area of AC is 1517 m^2 g^{-1} (**Figure A- 2**, **Appendix A**).The mass of ratio of the Ni-LTONF$_{10}$ to AC was 1:3 to balance the kinetics of the non-faradic and faradic components of HSC as described in the below equations

$$\mathbf{AC + PF_6 \leftrightarrow AC^+.PF_6^- + e^-} \qquad \textbf{(5-5)}$$

$$\mathbf{Li_4Ti_5O_{12} + 3Li^+ + 3e^- \leftrightarrow Li_4Ti_5O_{12}} \qquad \textbf{(5-6)}$$

Figure 5-11A shows the charge-discharge profiles of HSC in voltage window (0–3) V measured at different current densities. All the curves show change in the voltage charge/discharge rates with gradual slope between 2 V and 3 V and sharper slope below 2V which is attributed to the difference in charge/discharge kinetics between battery portion of the HSC and the electrical double layer capacitor (EDLC) portion. The faradic Li^+ intercalation /de-intercalation reaction at the anode side happens concurrently with PF_6 double layer creation at the surface of both electrodes, causing gradual slop in the region (2 – 3) V.

Figure 5-11B shows the Ragone plot obtained from the discharge data in the voltage profile of the HSC measurement shown in **Figure 5-11A** at different current densities using the following equations:[92,93]

$$\mathbf{E = 0.5\ C\ \Delta V^2} \qquad \mathbf{(5\text{-}7)}$$

$$\mathbf{P = E/dt} \qquad \mathbf{(5\text{-}8)}$$

$$\mathbf{C = I.dt\ /m.\Delta V} \qquad \mathbf{(5\text{-}9)}$$

Where E is the energy density, C is the cell capacitance, ΔV is the potential window, P is the power density, dt is the discharge time and m is the total mass of active materials in both anode and cathode. The results represent the average value of multiple measurements and show that the hybridized supercapacitor can deliver an energy density of 60 Wh kg^{-1} at power density of 1.5 kW kg^{-1} and capable of retaining a high energy density of 35 Wh kg^{-1} at 5 kW kg^{-1}. This remarkable performance can be attributed to the additional faradaic reactions, improved conductivity and stability of 1D Ni-LTONF_{10} anode material.

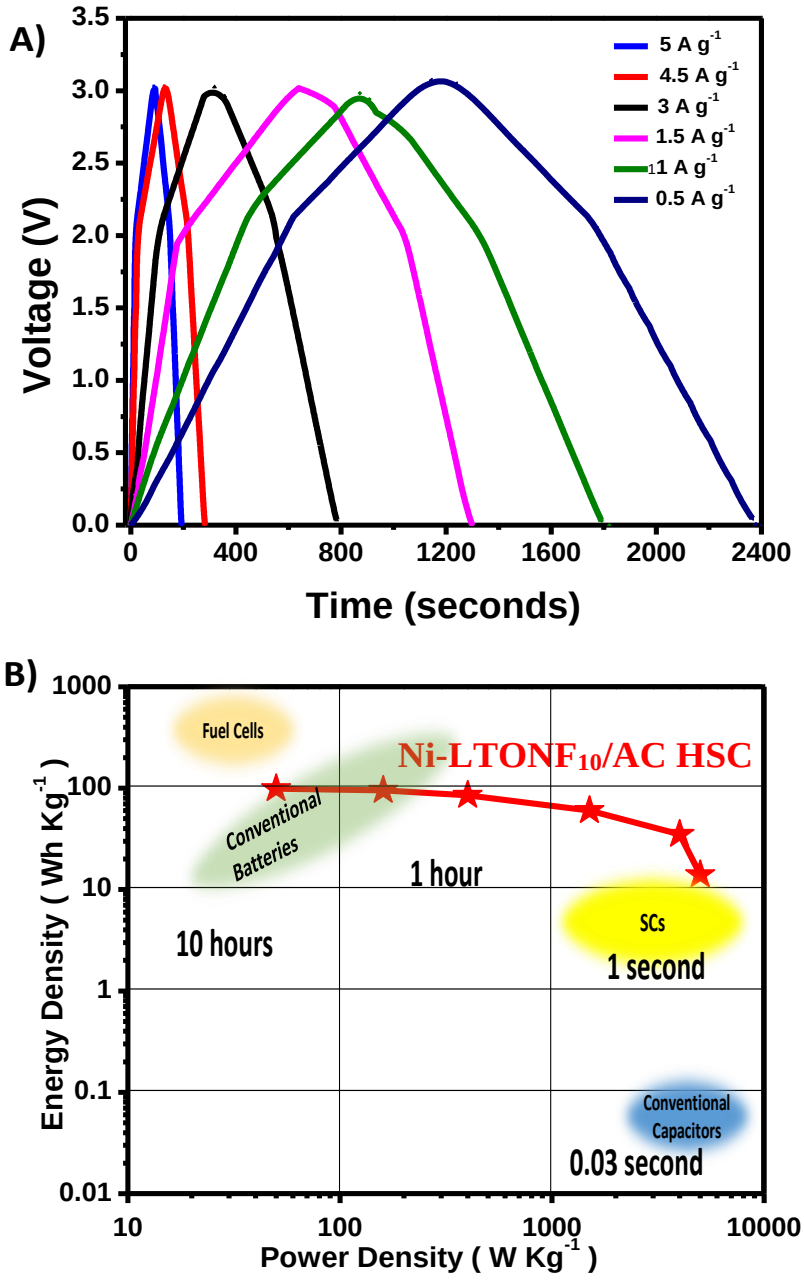

Figure 5-11. A) Charge/discharge profiles of HSC in voltage window (0-3) V measured at different current densities and, B) Ragone plot obtained from the discharge part in the voltage profile of HSC measurement at different current densities shown in Figure A. (reprinted from Ref.[19] , with permission of the Royal Society of Chemistry)

The explanation of all the improvements in electrochemical results shown in the previous results for the nickel doped LTO nanofibers material are attributed to the compositional change that happen to the LTO nanofibers due to the insertion of nickel into its lattice without noticeable effect on its structure in the formation of $Li_4Ti_{5-x}NixO_{12}$ (x=0, 0.05 and 0.1). LTO has Fd3m space group with the 8a tetrahedral sites occupied by lithium ions, 16d octahedral sites shared between lithium ions and titanium ions (Ti^{+4}) with 1:5 ratio of lithium ions to titanium ions and 32e sites are occupied by oxygen[4,55]. The octahedral 16c sites and the tetrahedral 8b and 48f sites are vacant which simplifies the intercalation and de-intercalation of lithium ions into the structure of LTO. This process accommodate up to three lithium ions as per equation (6) shown above. The transfer of lithium ion causes the phase of LTO to change from spinel ($Li_4Ti_5O_{12}$) to rock-salt phase ($Li_7Ti_5O_{12}$). Three lithium atoms at the 8a sites move during discharge to 16c sites and the inserted lithium ions occupy the vacant sites, this process is reversed during charge operation. The lithium ion diffusivity of spinel phase is higher than rock-slat phase because of the full occupancy of lithium sites in rock-salt phase while the electronic conductivity of rock-salt phase is higher because the Ti oxidation state in spinel-phase is (+4) which limits its electronic conductivity while the average oxidation state of Ti in rock-salt phase is (+3.4) due to the existence of both Ti^{+3} (60%) and Ti^{+4} (40%).[94]

The nickel insertion and the formation of $Li_4Ti_{5-x}NixO_{12}$ (x=0.05 and 0.1) and the change in the valence state of Ti ions from Ti^{+4} to Ti^{+3} confirmed by XPS results have positively affected the lithium transfer process and enhanced the efficiency with which LTO is utilized for Li^+ storage by making the entire LTO material accessible for intercalation leading to higher initial

capacity. The dual improvement in electronic conductivity due to nickel doping and improved lithium diffusivity in well crystalized 1D nanofiber morphology with good strain relaxation, shorter distance for Li^+ diffusion, interfacial control, continuous electron transport pathways and structure stability[95,96] further improved the thermodynamics of lithium intercalation reactions because nickel is well distributed across all the LTO structure as shown in the TEM image which not only enhanced and accelerated the intercalation/de-intercalation process of Li^+ ion, but also helped LTO to maintain fast lithium ion diffusion kinetics at high current rates leading to excellent capacity at high power rates as LIB anode material and outstanding energy densities at high power densities in asymmetric hybrid super capacitor. The improved results of Ni-LTONF$_{10}$ compared LTONF$_5$ to can be attributed to the additional amount of nickel which further improved the LTO initial capacity and lithium intercalation thermodynamics

5.1.5 Chapter conlcusion

As a conclusion, dual improvement of LTO properties was done through in-situ nickel doping to 1D lithium titanate nanofibers synthesized by facile electrospinning technique. The nickel insertion changed the chemical composition of LTO nanofibers without affecting the spinel crystal structure. The doped LTO nanofibers show improved capacity and outstanding rate capability at high power rates. The 10% nickel doped LTO nanofibers material showed initial capacity of 190 mAh g^{-1} and 63 mAh g^{-1} at 50 C with smaller voltage gap between the oxidation and reduction peaks compared to LTONF and Ni-LTONF$_5$. The hybridization of the 10% doped material into asymmetric supercapacitor also showed improved energy density at high power rates. Characterization techniques confirmed the homogenous distribution of nickel into the

structure of LTO without affecting the crystal structure or noticeable effect on the LTO lattice size. The nanofibers longitudinally 1D morphology is obtained in both doped and un-doped LTONF with some increase in the nanofibers diameters in nickel doped LTONF. The characterization techniques also confirmed stable nanofiber morphology after long cycling.

Chapter 6: Modified Chalcogens with Tuned Nano-Architecture for High Energy Density and Long Life Hybrid Super Capacitors

This chapter is reprinted in adjusted format from Ref.[53], with permission of the Royal Society of Chemistry.

Salah Abureden, Fathy M Hassan, Gregory Lui, Serubbabel Sy, Rasim Batmaz, Wook Ahn, Aiping Yu, and Zhongwei Chen, "Modified Chalcogens with Tuned Nano-Architecture for High Energy Density and Long Life Hybrid Super Capacitor" Journal of Material Chemistry A, 2017,5, 7523-7532.

6.1 Chapter introduction

The development of reliable and effective energy storage solutions is of paramount importance in today's renewable energy landscape.[97] Specifically, devices with high energy and power densities that can retain high capacities over many cycles are sought after in order to provide stable energy storage for consumer and grid-scale applications.[98-100] Supercapacitors are a class of device that are able to provide relatively good energy densities at high power densities over the course of many cycles.[6-8] However, one of the main shortcomings of supercapacitors is their low energy densities relative to current lithium ion battery technology. Therefore, the majority of recent research has been dedicated to fabricating supercapacitors with enhanced energy densities while still operating at higher power densities.

Supercapacitors are typically fabricated by introducing high surface-area materials (in order to induce electrochemical double-layer capacitance-based storage-EDLC) or pseudocapacitive materials including conducting polymers and metal oxides (in order to induce charge transfer-based storage).[7] In general, pseudocapacitive materials provide higher energy densities due their ability to provide redox-based charge transfer.

Various metal oxides and conducting polymers have been used as pseudocapacitive materials, including RuO_2, MnO_2, NiO, Co_2O_3, polyaniline, polypyrolle, however these materials are often limited by their low conductivity and electrochemical stability when compared to carbon materials. Transition metal sulfides are a relatively recent electrode material that have shown promising pseudocapacitive performance in supercapacitors.[101] $NiCo_2S_4$ is one such metal sulfide that has shown great promise in supercapacitors.[102-104] Binary metal sulfides like $NiCo_2S_4$ (NCS) have been shown to provide higher electron conductivity than their oxide variants, and show further improvement over single component sulfides due to the increased capacity for redox reactions.[105,106] For example, Xiao et al showed that conversion of $NiCo_2O_4$ to NCS nanotube arrays produced an increase in areal capacitance from 0.52 F cm^{-2} to 0.87 F cm^{-2} at 4 mA cm^{-2}.[105] Chen et al found a similar phenomenon with NCS urchin-like nanostructures, achieving a gravimetric capacitance of 761 F g^{-1} at 50 A g^{-1}.[106] Yet, $NiCo_2S_4$ still suffers from low structural stability and cyclability.[107]

These issues can be solved using the following strategies: 1) improving NCS structural stability using a conductive substrate such as graphene.[108,109] In-situ growth of $NiCo_2S_4$ on graphene can also increase the overall surface area of the metal sulfide. 2) improving NCS overall

conductivity via doping, which can greatly improve electrode stability and capacitance[101,110-112]. To the best of our knowledge, metal doping of NCS has yet to be accomplished in literature but can be used to greatly improve its electrochemical properties.

Graphene-based materials are widely investigated for supercapacitor applications due to their superior electrical and mechanical characteristics, and high surface area. On the other hand, vanadium compounds have been widely used in supercapacitors for their remarkable specific capacitance, superior conductivity, excellent long cyclability, and high ability of charge transfer reversibility which are all favorable for achieving high energy densities at high power densities in next-generation energy devices.[108,113-115]

Herein, we report for the first time a novel in-situ vanadium modified $NiCo_2S_4$ rooted on graphene sheets with superior electrochemical performance synthesized using a facile solvothermal process. Three types of materials were synthesized and tested: pure $NiCo_2S_4$ (NCS), graphene wrapped NCS (GNCS), and vanadium-doped graphene wrapped NCS (VNCS). We also synthesized sulfur doped graphene (SG) to examine the effect of sulfur on graphene morphology. The combination of the excellent distribution of NCS on the graphene surface and the vanadium modification (doping) lead to the formation an ordered crystal structures NCS nanosheets, highly improved performance at high power rates, and stability over long cycling periods with high capacitance retention. We also fabricated hybrid supercapacitors (HSC's) using the three materials to further investigate the improvements on electrochemical performance. The VNCS showed superior energy density at high power densities making it an

excellent candidate for hybrid supercapacitor devices and opening the door for more investigation on this material.

6.2 Experimental section

This section will provide details about the material synthesis and electrodes fabrication procedures

6.2.1 Materials

All materials were purchased from Sigma Aldrich and used as-received.

6.2.2 Synthesis of NCS

1 mmol of $Ni(NO_3)_2 \cdot 6H_2O$ dissolved in 1 ml deionized distilled water (DDI) water, 2 mmol of $Co(NO_3)_2 \cdot 6H_2O$ dissolved in 1 mL DDI were added to 4 mmol of Thiourea (Tu) dissolved in 2 ml DDI after being heated for few minutes on hot plate at 60^oC. The mixture was mixed by vortex and then sonicated for 10 minutes before being added to 25 ml ethylene glycol (EG). This precursor solution was sonicated for 1 hour before being placed in a 50 mL Teflon-lined autoclave. The material was heated to 160^oC for 12 hours followed by 220^oC for 12 hours. The solution was then filtered and washed by ethanol and DDI several times. The collected material was dried at 60^oC for 3 hours in a convection oven before drying under vacuum at 80^oC for 12 hours. Lastly, the material was calcined in a tube furnace at 300^oC for 3 hours under Argon atmosphere to improve crystallinity.

6.2.3 Synthesis of GNCS and VNCS

For the GNCS synthesis: 43.6 mg graphene oxide (GO) synthesized using modified Hummers' method was added to the previously described precursor solution before sonicating for 1 h. The rest of steps were similar to above procedure. For VNCS: 43.6 mg GO and 0.2 mmol VCl_4 were added to the precursor solution described in pure $NiCo_2S_4$ before sonicating for 1 h. The rest of steps didn't change. The selection of the synthesis regime is based on the fact that TU is stable below 120^{o}C. TU acts as s reducing and allocating agent. TU molecules have a high dipole moment which helps the precursor molecules self-assemble onto the GO nanosheets where they anchor to the oxygenated groups. Around 190^{o}C, TU starts to decompose along with the precursor and the reduction of GO is accelerated. As a result, nickel, cobalt and vanadium combine with sulfur to form the active material on the surface of rGO[39,116-118]. The reaction medium and conditions help accelerate the reduction of GO[119-121]. The experiment setup is shown in **Figure 6-1**.

6.2.4 Synthesis of sulfur doped graphene (SG)

4 mmol of Tu dissolved in 2 ml DDI were added to 43.6 mg graphene oxide (GO) dispersed in 25 ml EG. The mixture was sonicated for 1 hr. the rest of steps followed the same VNCS procedure described above.

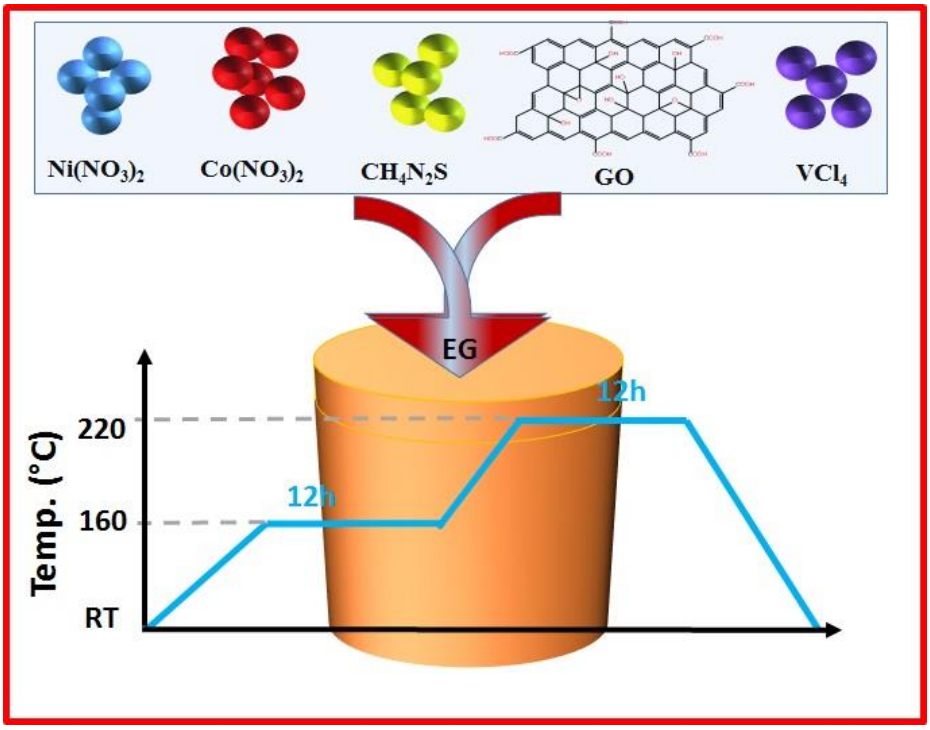

Figure 6-1 Schematic showing the precursor solution and the solvothermal experiment procedure.

(reprinted from Ref.[53] , with permission from the Royal Society of Chemistry)

6.2.5 Electrodes fabrication:

The working electrodes were fabricated using the active material (80wt %), super P carbon (10wt %), and polyvinylidenefluoride (10wt %), with *N*-methyl-pyrrolidone (NMP) solvent to prepare slurry. The slurry was deposited on a pre-cleaned nickel foam (1.5 x 1.5 cm) using a drop casting method before drying at 60^{o}C for 2 hours in a convection oven and 12 hours in a vacuum oven at 80^{o}C. The electrodes were then pressed under 10 MPa. The mass loadings of the three electrodes were 2.25, 2.03 and 2.18 mg cm^{-2} for NCS, GNCS and VNCS, respectively.

This range of mass loadings was selected to give the highest areal capacitance as can be seen in **Figure B- 1A (Appendix B).**

6.3 Characterization

Sample microstructure and morphology were analyzed using X-ray diffractometer (Rigaku Miniflex 600 X-Ray Diffractometer) located at the Clean Energy and Applied Material Laboratory-University of Waterloo. TGA was analyzed using (TGA Q500) located at the analytical lab at University of Waterloo. The X-ray photoelectron spectroscopy (XPS) analysis was done at the Ontario Center for Characterization of Advanced Materials using PHI Quantera XPS spectroscopy located at the Ontario Center for Characterization of Advanced Materials (University of Toronto). Scanning electron microscopy was conducted using a ZEISS ULTRA PLUS SEM located at Waterloo Advanced Technology Laboratory (University of Waterloo). Transmission electron microscopy was performed using a JEOL 2010F TEM/STEM field emission microscope located at the Canadian Center for Electron Microscopy (CCEM) located at McMaster University, Ontario-Canada.

Figure 6-2A shows the XRD pattern of the NCS, GNCS and VNCS samples. All samples showed similar diffraction peaks around 26.75^{o}, 31.50^{o}, 38.10^{o}, 50.35^{o}, and 55.30^{o} corresponding to (220), (311), (400), (511) and (440) planes of the cubic $NiCo_2S_4$ phase (JCPDS Card No. 43-1477) with no sign of impurities. No diffraction peaks can be shown for the graphene which can be attributed to its low diffraction intensity.[122] The similarity of the three XRD patterns reveals that vanadium doping did not cause any noticeable changes to the crystal structure of the cubic NCS. To further investigate this, the peak corresponding to the

(311) plane was magnified as shown in **Figure 6-2B**, a clear shift in the VNCS to a lower angle and higher intensity when compared to GNCS and PNCS samples can be seen. This can be attributed to the successful insertion of vanadium into the lattice of NCS[123,124]. This finding is in agreement with the TEM results discussed below which very clearly show the dislocation in plane (311) in VNCS resulted due from vanadium insertion into the NCS lattice. Another shift is noticed in the (511) plane as seen in **Figure B-** 1**B (Appendix B)**. The other planes showed almost identical peaks. The TGA analysis under air is shown in **Figure B-** 1**B (Appendix B)** and reveals that the vanadium-modified chalcogen is 85.3wt% and rGO is 14.7wt%. The XRD analysis of SG is shown in in **Figure B-3A (Appendix B)** showing typical graphitic peaks.

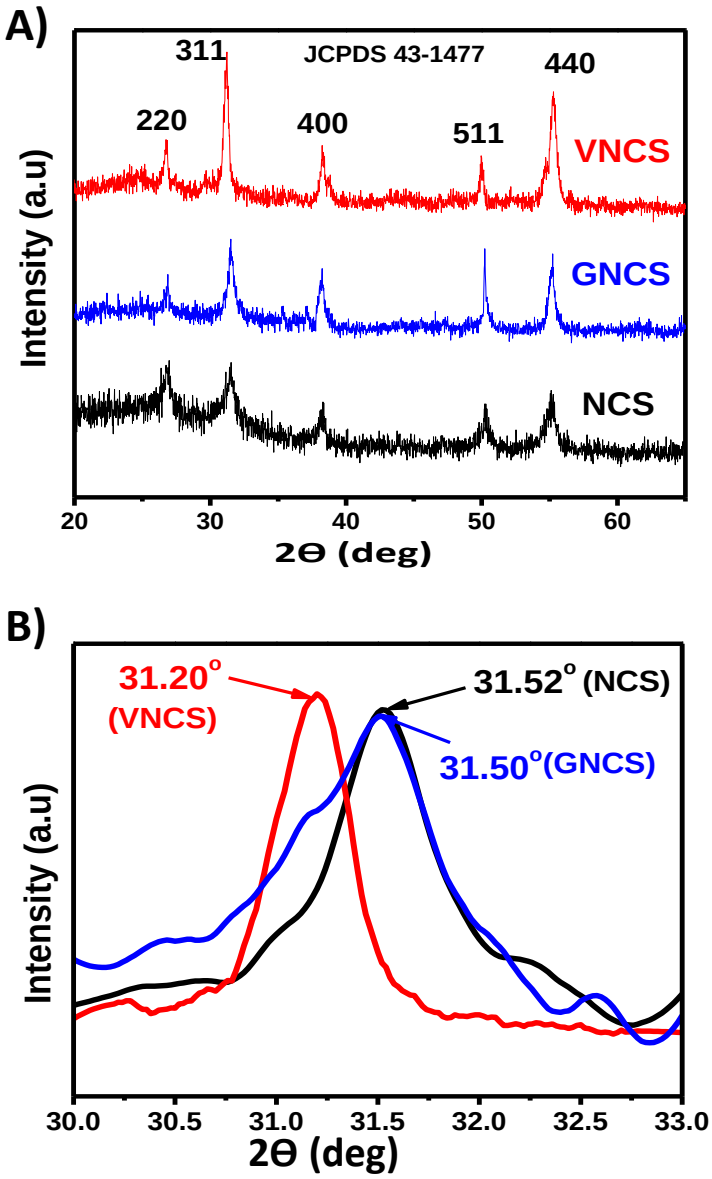

Figure 6-2. A) XRD pattern of all samples, and B) magnification of the XRD peak corresponding to the (311) plane of the three material showing a negative peak for the VNCS. (reprinted from Ref.[53] , with permission from the Royal Society of Chemistry)

SEM images of NCS, GNCS and VNCS can be seen in **Figure 6-3**. **Figure 6-3A** shows that the nanoparticles of NCS have the tendency to aggregate together forming larger size nanoparticles, while **Figure 6-3B** shows how the graphene nanosheets wrap around the nanoparticles (average size of 100 nm) and hinder particle agglomeration in GNCS sample. The morphology in **Figure 6-3C** reveals VNCS nanosheets of wrapped with, and laminated on, graphene nanosheets, leading to stable interfacial contact with the graphene surface. This helps in: hindering particle aggregation; enhancing electron transfer kinetics during charge-discharge operations due to graphene's high conductivity; and, allowing for faster ion diffusion due to the increased contact area and uniform adhesion of VNCS on the graphene surface.[122,125,126] More SEM images showing the graphene wrapping the NCS in GNCS can be seen in **Figure B-2(Appendix B).** SEM image of sulfur doped graphene is shown in **Figure B-3D (Appendix B)**. The results confirm that sulfur alone has no effect on changing the nanosheets morphology of graphene.

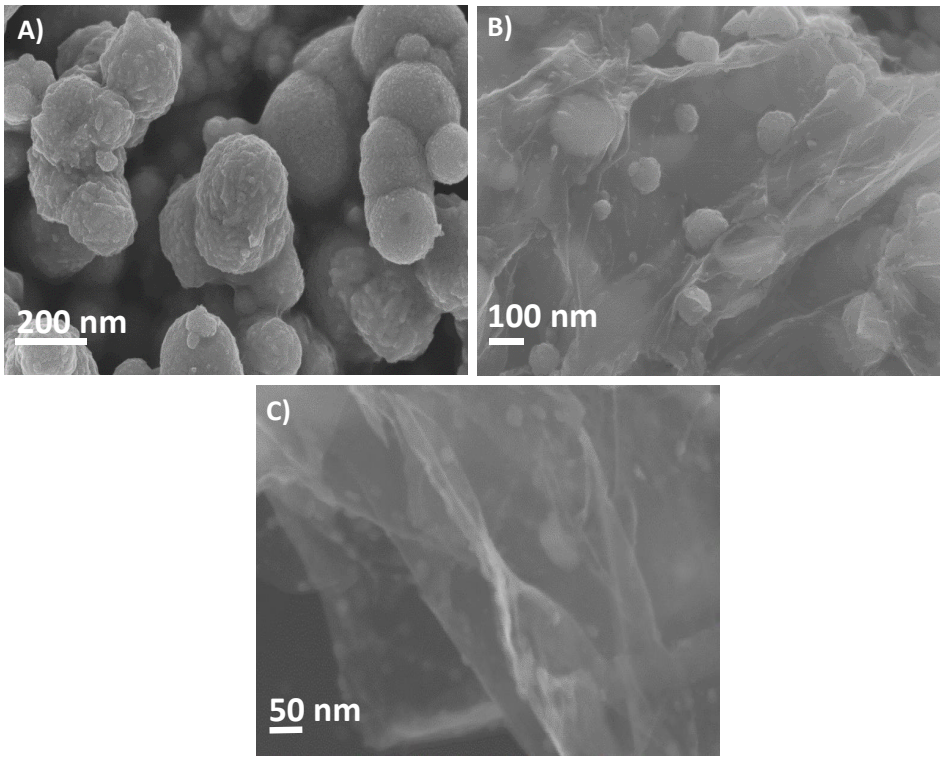

Figure 6-3. A-C) SEM images of NCS, GNCS and VNCS, respectively. (reprinted from Ref.[53] , with permission from the Royal Society of Chemistry)

For more investigation on the effect of V-doping on the chemical composition of the NCS, X-ray photoelectron spectroscopy (XPS) was used to analyze the elemental species and chemical composition changes. **Figure 6-4 (A-E)** shows the XPS spectra of the VNCS sample. The C 1s spectra shown in **Figure 6-4A** reveals sp^2 carbon-carbon double graphite bond (C=C) peak at 284.62 eV. The peak at 286.1 eV is indexed to carbon-oxygen double bond (C=O) and the weak peak at 288.2 eV is indexed to carbon-oxygen single bond (C-O).[107,127] **Figure 6-4B** shows the Ni 2p spectra, where the low energy band peak at 854.05 eV and the high energy band peak at 871.75 eV can be indexed to Ni^{+2}, whereas the low and high energy band peaks at 856.1 and 873.78 eV, respectively are indexed to Ni^{+3}. In the Co 2p spectra (**Figure 6-4C)**,

the peaks at 779.45 and 795.6 are indexed to Co^{+3}, whereas the peaks at 781.68 eV and 797.10 eV are indexed to Co^{+2}. **Figure 6-4D** shows the S 2p spectra where two peaks at 162.05 eV and 163.30 eV are found with one shake up satellite at 169.20 eV. The peak at 162.05 eV is indexed to sulfur ions in low coordination on the surface and the peak located at 163.30 eV is indexed to standard metal-sulfur bond[106,107,128]. The XPS spectra of V 2p is shown in **Figure 6-4E** with two distinguished main peaks at 516.40 eV and 524.10 eV. Both peaks are indexed to pentavalent vanadium.[129-132] The XPS analysis of SG is shown in **Figure B-3B-C (Appendix B)**. The results clearly indicates the introduction of sulfur into graphene. The XPS spectra for NCS and GNCS samples are shown in **Figure B-4(Appendix B).**

Figure 6-4 (F-H) shows comparison of binding energy between NCS, GNCS, and VNCS for Ni 2p, Co 2p, and S 2p, respectively. The results show similar peaks for NCS and GNCS samples whereas VNCS shows shift in the binding energy of Ni 2p, Co 2p, and S 2p to lower values, suggesting a change in the electron cloud density around these elements due to the insertion of pentavalent vanadium[133-135]. The XPS atomic ratio analysis of the three samples shows the following stoichiometric ratios: $Ni_{0.98}Co_{1.99}S_{4.03}$, $NiCo_{2.01}S_{3.99}$, and $Ni_{0.98}Co_{1.98}V_{0.04}S_{4.03}$ for NCS, GNCS, and VNCS samples, respectively. These results suggest that the atomic ratios between Ni, Co, and S very closely match the stoichiometric formula ($NiCo_2S_4$) and that vanadium is successfully inserted into the lattice of NCS without substituting any element. This further explains the crystal dislocation shown in the TEM images and the plane shift shown in the XRD results. More information about the peaks including binding energies, FWHM and atomic ratios can be seen in **Table B-1(Appendix B).**

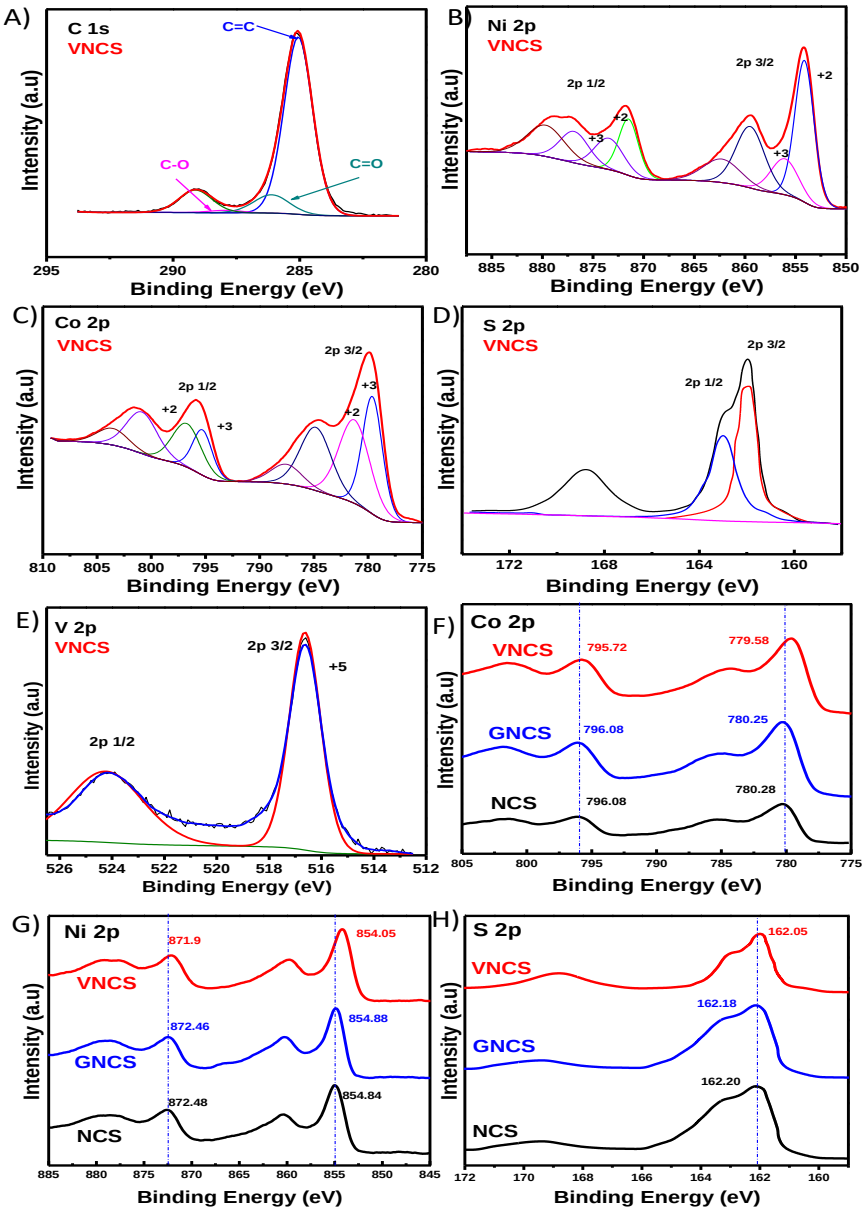

Figure 6-4. XPS spectra measurements A-E) XPS of VNCS showing C 1s, Ni 2p, Co 2p, S 2p and V 2p, respectively, and F-H) XPS spectra comparison of all samples for Ni 2p , Co 2p, and S 2p, respectively showing shift in binding energy of the VNCS sample. (reprinted from Ref.[53] , with permission from the Royal Society of Chemistry).

Figure 6-5 shows the TEM images of VNCS. The low magnification TEM image seen in **Figure 6-5A** reveals the homogenous distribution of NCS nanosheets on the surface of the graphene nanosheets. **Figure 6-5B** shows the TEM image of GNCS with the graphene wrapping the NCS nanoparticles. **Figure 6-5C** shows a higher magnification TEM image of the VNCS nanosheets lying on graphene sheets while **Figure 6-5D** shows the selected area diffraction pattern (SAD) which reveals the polycrystalline structure of the VNCS with the different planes identified. **Figure 6-5E** shows an HRTEM image of the (311) plane and the lattice dislocation. This finding is a very clear evidence of the successful insertion of vanadium into the lattice of NCS which agrees with the XRD and XPS results and explains the reason of the improved electrochemical performance as discussed in the next section. The image in **Figure 6-5F** shows TEM images obtained using high angle dark-field scanning transmission electron microscopy (HAADF-STEM) with the selected area for element distribution scanning which are shown in **Figure 6-5G**. The images reveal the homogenous distribution of all elements in the structure of VNCS that is also uniformly distributed on to the graphene surface, as shown in **Figure 6-5A** and **Figure 6-5C**. For deeper analysis of the atomic distribution within the VNCS structure, electron energy loss spectroscopy (EELS) was used. **Figure 6-5H** shows the EELS investigation area, while **Figure 6-5I** shows the EELS results of Ni, Co, S, and V elements, respectively. The results reveals the excellent distribution of all elements on the atomic level (one pixel in these image is equivalent to 3.6 x 3.6 nm). **Figure B-5 (Appendix B)** shows TEM images of GNCS, the results also confirmed the existence of all elements in a homogenous distribution.

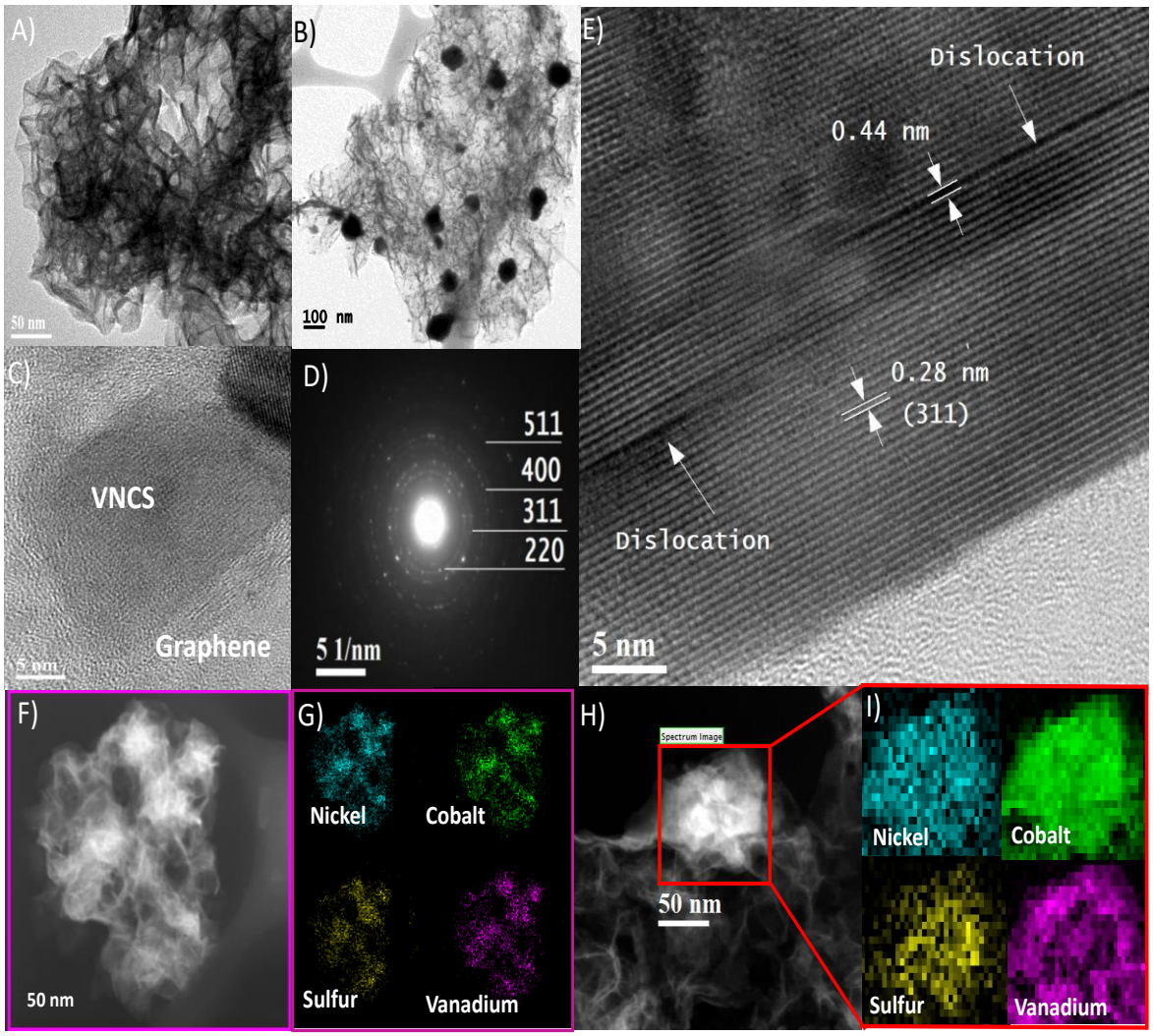

Figure 6-5. TEM images A) TEM image of VNCS showing the sheet-on sheet structure, B) TEM image of GNCS showing graphene wrapped nanoparticles, C) TEM image showing VNCS lying on graphene surface, D) SAD with the different planes identified, E) HRTEM showing the dislocation in crystal, F) HAAD-STEM image showing the EDS investigation area, G) EDS mapping of the image in F showing Ni, Co, S, and V, H) EELS investigation area, and I) EELS mapping of the selected area in image H showing the Ni, Co, S, and V with each pixel equivalent to 3.6x3.6 nm. (reprinted from Ref.[53] , with permission from the Royal Society of Chemistry)

6.4 Electrochemical performance

The electrochemical behavior of half-cell electrodes was analyzed in a three electrode setup using platinum sheet (1.5 cm x 1.5 cm) as a counter electrode, saturated calomel electrode (SCE) as the reference electrode, and the synthesized material as the working electrode. The tests were carried out in 2 M KOH electrolyte. The cyclic voltammetry (CV) of all samples at 20 mV s^{-1} and a voltage range of (-0.2 V – +0.6 V) can be seen in **Figure 6-6A**, while **Figure 6-6B** shows the CV measurements of VNCS at various scan rates. All measurements show two peaks revealing the pseudo-capacitive characteristics resulting from the reversible faradic redox reactions of Co^{+2}/Co^{+3} and Ni^{+2}/Ni^{+3} as per the following equations:[103,104]

$$\mathbf{CoS + OH^- \leftrightarrow CoSOH + e^-} \qquad \mathbf{(6\text{-}1)}$$

$$\mathbf{CoSOH + OH^- \leftrightarrow CoSO + H_2O + e^-} \qquad \mathbf{(6\text{-}2)}$$

$$\mathbf{NiS + OH^- \leftrightarrow NiSOH + e^-} \qquad \mathbf{(6\text{-}3)}$$

The results seen in **Figure 6-6A** reveal that GNCS and VNCS have larger CV curve areas compared to the NCS sample, indicating higher specific capacitance in these samples which is attributed to the additional capacitance added by graphene and vanadium [114,136]. The CV test for the nickel foam alone can be seen in **Figure B-6A (Appendix B)**, indicating the neglible effect of the nickel foam and confirms that the pseudocapacitive characteristics in the CV measurment is mainly from the active material. **Figure B-6B and Figure B-6C (Appendix B)** show the CV data of the CNS and GNCS samples at various scan rates. **Figure 6-6C** shows the galvanostatic charge-discharge measurements of all materials at 10 A g^{-1}, while **Figure 6-6D**

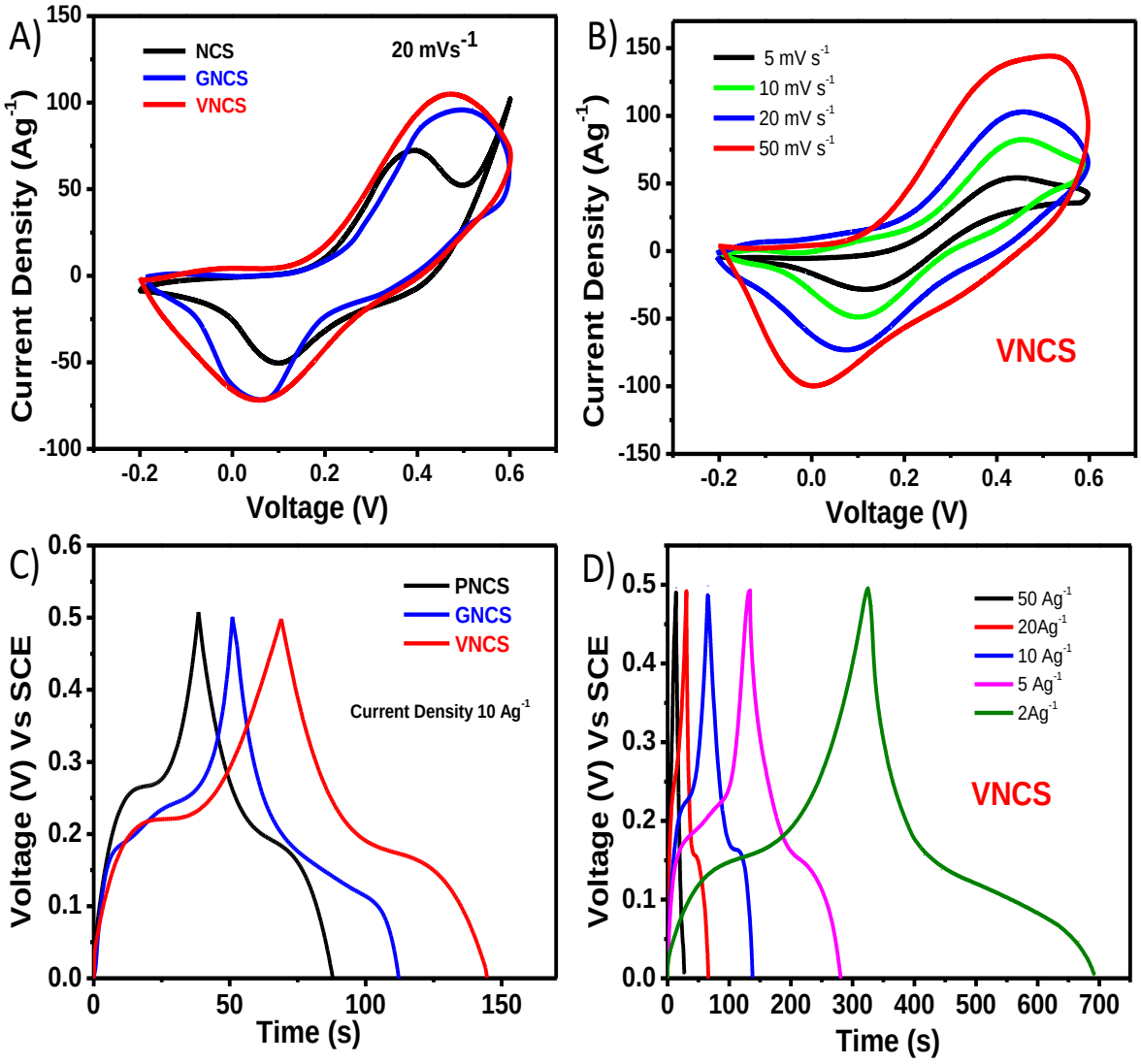

Figure 6-6. Electrochemical measurements: A) CV for the three samples at 20 mV s-1, B) CV curves of VNCS at different scan rates, C) Galvanostatic charge-discharge of all samples at 10 Ag-1, and D) Galvanostatic charge-discharge of VNCS at different current densities. (reprinted from Ref.[53] , with permission from the Royal Society of Chemistry)

shows the charge-discharge measurements of the VNCS sample at multiple current rates. The results show symmetric charge-discharge processes for all samples and revealing stable pseudocapacitive performance of the synthesized materials. **Figure 6-7A** shows the specific capacitance of all samples at various current rates. The specific capacitance is obtained using the equation below: [136,137]

$$C_S = I/(m\,\Delta V/\Delta t) \qquad (6\text{-}4)$$

Where C_S is the specific capacitance (F g^{-1}), I is the discharge current (A), m is the mass of the active material (g) and $\Delta V/\Delta t$ is the discharge curve slope (V s^{-1}) obtained after the voltage drop. It can be seen from the curves that the GNCS shows higher initial capacitance and much better capacitance retention at higher power rates when compared to NCS. This improvement can be attributed to the effect of graphene in reducing particle aggregation, providing larger surface area with more electroactive sites for ions diffusion, enhancing the charge/discharge kinetics, and allowing for faster electron transport.[50,108,122,125]

It is also shown that both GNCS and VNCS show almost similar initial capacitance at 2 A g^{-1}. However, a distinction in performance arose as the current density increased. GNCS retains 75.7% of its capacitance from 2 to 20 A g^{-1}, while VNCS retains 90.2% of its capacitance from 2 to 20 A g^{-1}. The distinguished performance of the VNCS continued as the current rate increased from 20 A g^{-1} to 50 A g^{-1} with only 6.5 % capacitance loss compared to 9.1 % for the GNCS. Moreover, the capacitance of the VNCS remained higher than 1000 Fg^{-1} (1024 Fg^{-1}) even at 50 A g^{-1} compared to 810 F g^{-1} and 237.76 F g^{-1} for GNCS and NCS, respectively. These values represent 23.5%, 61%, and 76.4 % capacitance retention compared to the capacitance of each

sample at 2 A g^{-1}. A comparison between the capacitance values of NCS and VNCS at low and high current densities can be seen in **Figure 6-7B**. The results clearly reveal the outstanding improvement in capacitance at high current density for the VNCS sample with a 430% increase compared to NCS sample. The charge-discharge data of NCS and GNCS at various current rates can be seen at **Figure B- 7 (Appendix B).** The summary of specific capacitance values of all materials at various current rates is shown in **Figure B-8A (Appendix B).** The capacitance retention at various current rates compared to capacitance at 2 A g^{-1} is shown in **Figure B-8B (Appendix B).** The results reveal that VNCS showed superior performance at all current rates compared to NCS and GNCS. The cycling stability of all samples was examined at 10 A g^{-1} (**Figure 6-7C**). The capacitance retention values after 10,000 cycles are 64.7%, 80.8%, and 90.5% for NCS, GNCS, and VNCS, respectively. The VNCS showed around 140% higher capacitance retention than NCS and remarkably higher than the GNCS sample, losing only ~10^{-3} F/cycle. All samples showed high coulombic efficiency throughout the cycling test as can be seen in **Figure B-9 (Appendix B)** indicating high material stability. VNCS and GNCS showed higher coulombic efficiency compared to NCS which can be attributed to the graphene and vanadium doping effect, providing improved reversible charge and discharge kinetics.

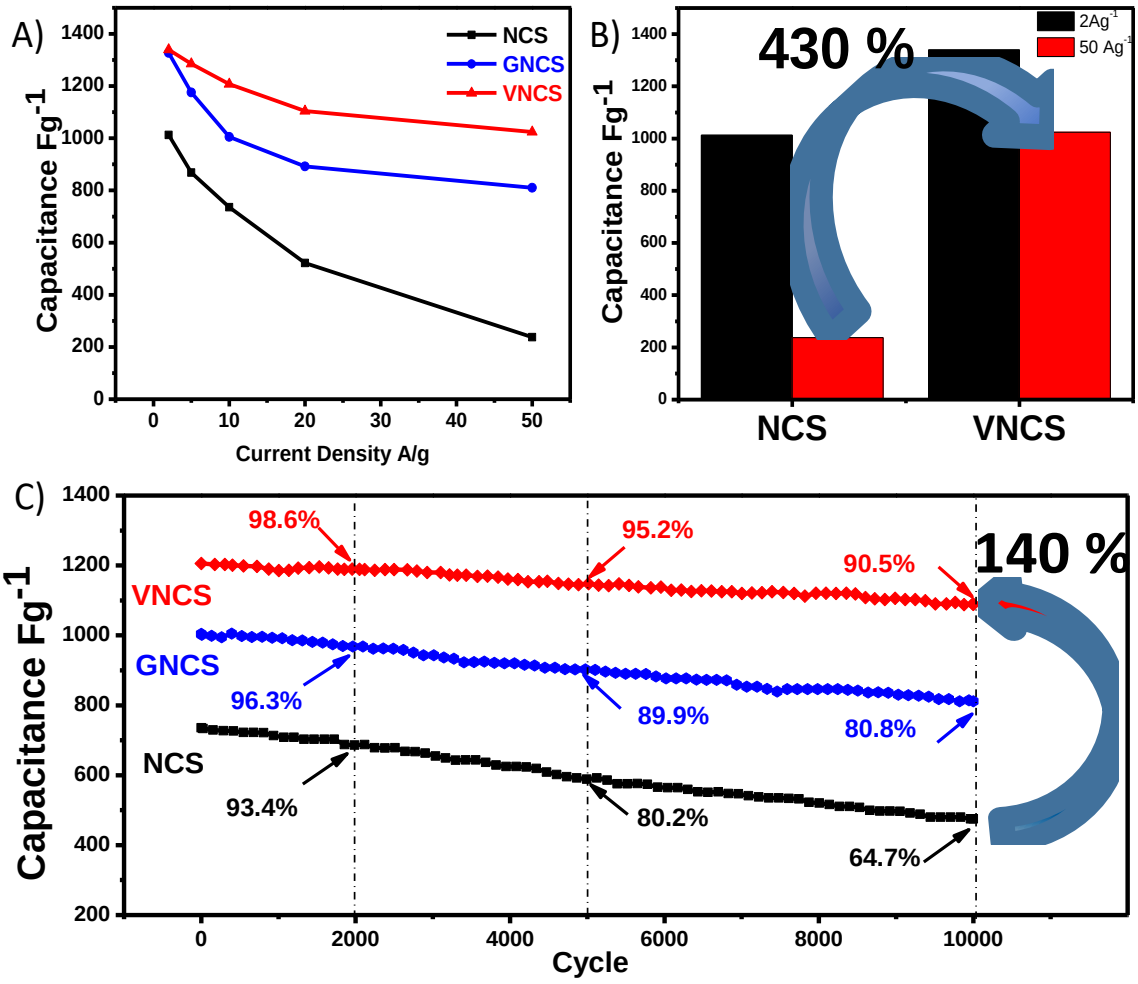

Figure 6-7. A) Specific capacitance of all samples at different current densities, B) Performance comparison between NCS and VNCS at low and high current densities and, C) long cycling performance of the three samples for 10,000 cycles. (reprinted from Ref.[53] , with permission from the Royal Society of Chemistry)

The charge-discharge and long cycling results clearly demonstrate the impact of graphene and vanadium doping in enhancing the electrochemical performance of the device. We believe that the improved sheet-on-sheet interaction is behind the high stability and performance presented by VNCS, which results in the following: 1) allows for faster ion diffusion due to the increased number of electroactive sites resulted from the increased contact area between the VNCS sheets and graphene sheets in addition to the uniform distribution of all elements of VNCS[122]. 2) Generating strong covalent interaction of the transition metal chalcogens onto graphene surface, explaining the long cycling stability[138,139]; and, 3) Improving the overall conductivity, pseudocapacitance, and stability through vanadium doping.[114,124,136] A comparison with recent reports is shown in **Table B-2 (Appendix B),** our work is the first report of its kind to report V-doped graphene wrapped NCS and among the highest performance obtained so far.

To further investigate the effect of graphene wrapping and V-doping on the electrochemical performance of NCS, we fabricated asymmetric hybrid supercapacitors (HSCs). The positive electrode in each one of these HSCs was made from one of the three synthesized materials, while the negative electrode for all HSC devices was made from a composite of activated carbon and graphene (AC/G) with a mass ratio of 9:1. The AC/G material was also coated on nickel foam using a drop casting method. The mass ratio of active material in the cathode to active material in the anode was controlled to balance the charge on both electrodes ($q^+ = q^-$) because of the difference in charge storage mechanism in each electrode (faradic and EDLS) using the following well known charge balance equations:

$$q = C \Delta V m \quad (6\text{-}5)$$

$$m^+/m^- = C^- \Delta V^- / (C^+ \Delta V^+) \quad (6\text{-}6)$$

Where q is the charge, m is the mass, C is capacitance and ΔV is the voltage window. The capacitance of AC/G is 173 F g^{-1} obtained from the charge-discharge test that can be seen in **Figure B-10B (Appendix B).** The N2 adsorption- desorption isotherm of AC/G electrode is shown in **Figure B-10C (Appendix B)** (BET surface area 1565 $m^2 g^{-1}$).

The electrochemical measurements were conducted using similar electrolyte medium (2 M KOH) but in a higher voltage window (0 - 1.6) V. The voltage range was increased after the AC/G electrode showed excellent electrochemical reversibility in a voltage window (-1.0 to 0) V for both CV and CD tests **(Figure B-10 (A-B), Appendix B).** The CV results for the three HSCs at 20 mV s^{-1} can be seen in **Figure 6-8A**. All curves show hybrid capacitance from both EDLC and faradic redox reactions where the two redox peaks are still present. **Figure 6-8B** shows the CV results for the VNCS-HSC device at various scan rates. It is noticed that the behavior of the curves do not change with increasing scan rate suggesting excellent reversible charge-discharge operations and stable hybridization between the two reactions mechanisms at the cathode and anode.[104,140] **Figure B-11 (Appendix B)** shows the CV test of CNS-HSC and GNCS-HSC devices at various scan rates. The charge-discharge measurements of all HSCs at 10 A g^{-1} is shown in **Figure 6-8C**, while **Figure 6-8D** shows the charge-discharge measurements of VNCS-HSC at various current rates. Both figures demonstrate that all devices have symmetric charge-discharge profiles at all current rates, revealing stable and well balanced reaction kinetics between the pseudocapacitive and EDLC parts of the HSC.

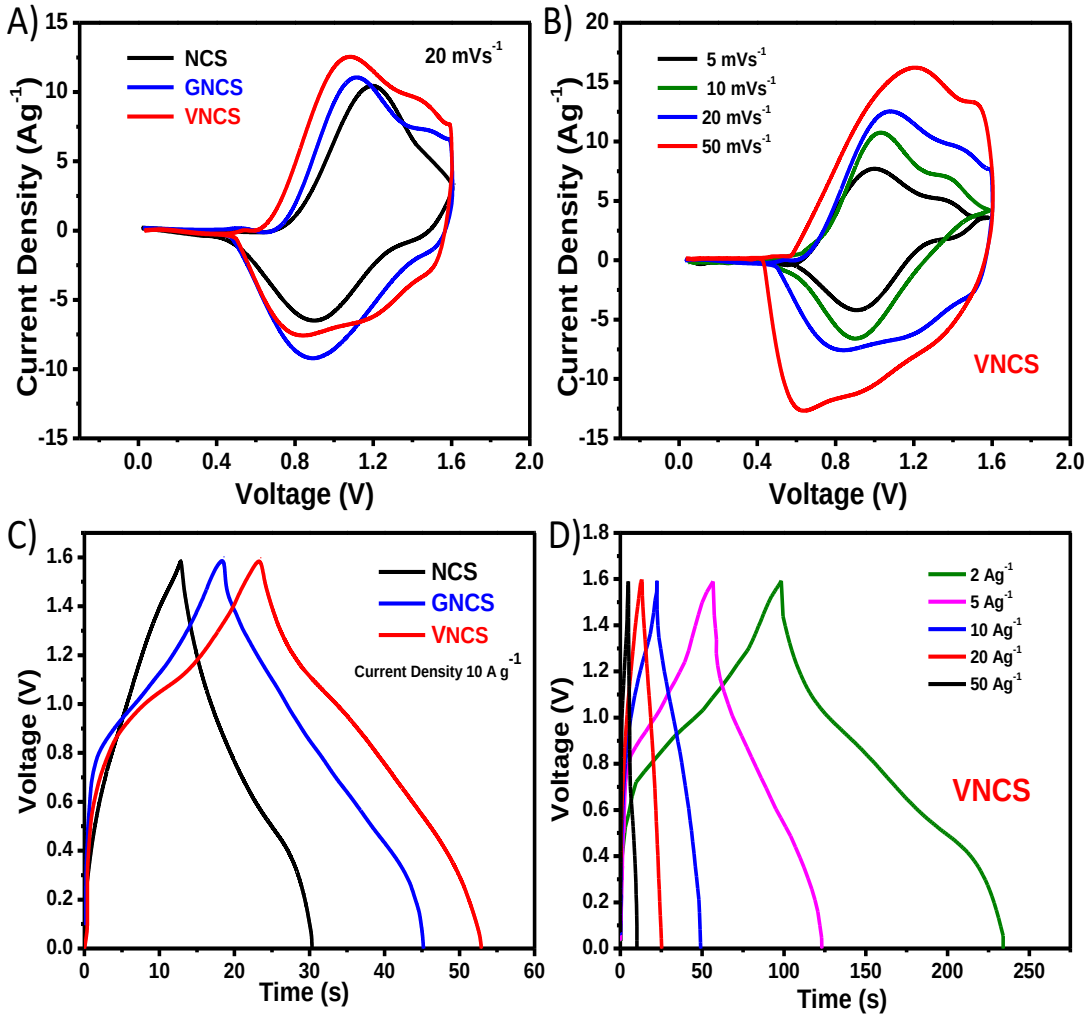

Figure 6-8. Electrochemical measurements of HSCs devices, A) CV of all devices at 20 mVs-1, B) CV of VNCS-HSC at different scan rates, C) Galvanostatic charge-discharge of all devices at 10 Ag-1, and D) Galvanostatic charge-discharge of VNSC-HSC sample at differet current densities. (reprinted from Ref.[53] , with permission from the Royal Society of Chemistry)

The calculated specific capacitance is shown in **Figure 6-9A** using **Equations 5** & **6** above using the total mass of the active material in both cathode and anode. The results show that the VNCS-HSC exhibited higher initial capacitance and remarkable capacitance retention at higher current densities compared to the other two devices. This significant improvement can be attributed to the crucial effect of vanadium's high specific capacitance and higher conductivity.[132] The results also shows the effect of graphene wrapping in improving the initial capacitance and capacitance retention in the GNCS-HSC compared to NCS-HSC. **Figure 6-9B** shows a comparison between the capacitance of NCS-HSC and VNCS-HSC devices at 2 A g^{-1} and 50 A g^{-1}. It is noticed that the VNCS-HSC shows around 260% higher specific capacitance at a high current rate of 50 A g^{-1} compared to the NCS-HSC, which further demonstrates the important effect of vanadium doping on electrochemical performance at high power rates.

The charge-discharge curves for NCS-HSC and GNCS-HSC at various current rates are shown in **Figure B-12 (Appendix B)**. **Figure B-13A (Appendix B)** shows the specific capacitance values of all HSCs devices at various current rates, while **Figure B-13B (Appendix B)** shows the capacitance retention of all HSC's devices at different current densities compared to the capacitance of each device at a low current rate of 2 A g^{-1}. All of these results further demonstrate the superior performance of the VNSC-HSC device at all current densities.

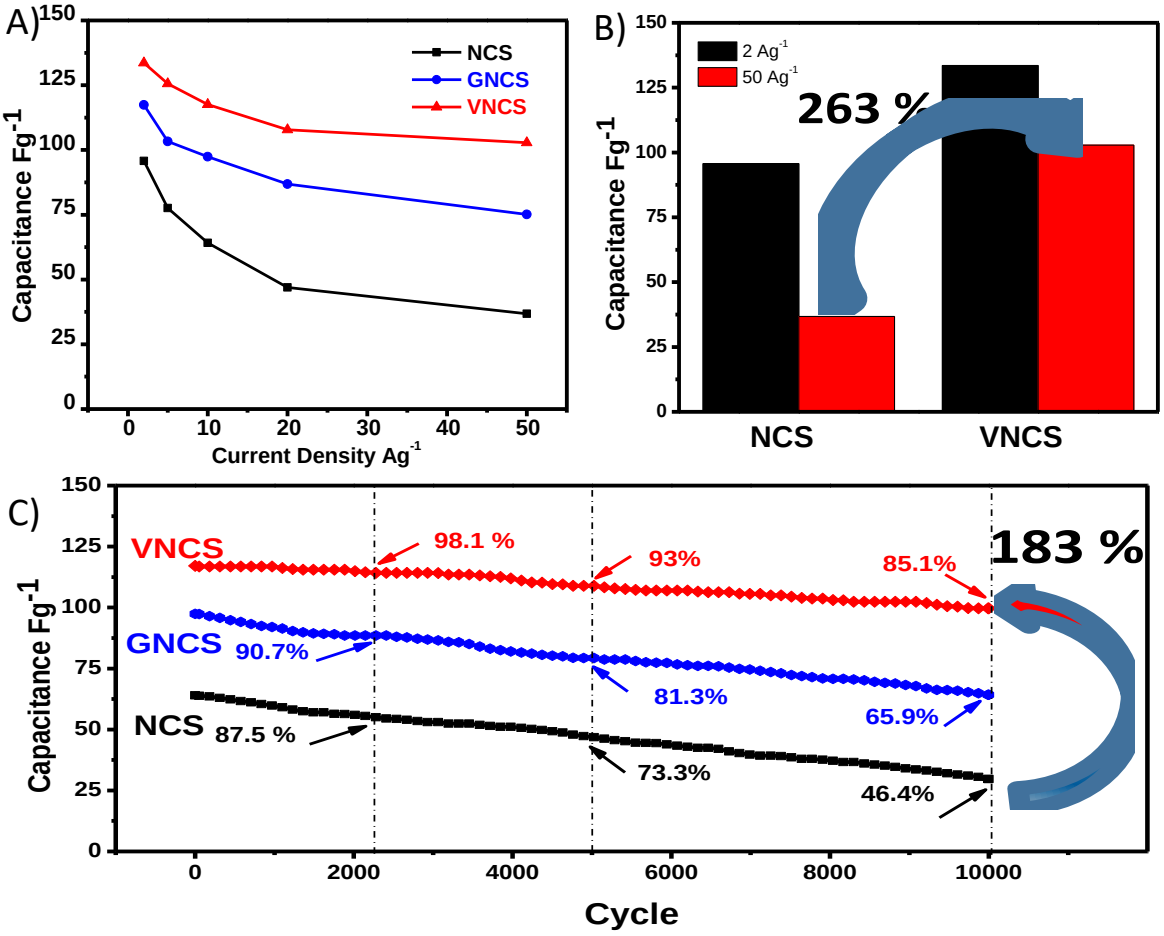

Figure 6-9. A) Specific capacitance of all HSCs devices at different current densities, B) Performance comparison between NCS-HSC and VNCS-HSC devices at low and high current densities and, C) long cycling performance of the three devices for 10,000 cycles. (reprinted from Ref.[53] , with permission from the Royal Society of Chemistry)

Figure 6-9C shows the long-term cycling stability of all devices at 10 A g^{-1}. The NCS-HSC shows 46.4% capacitance retention after 10,000 cycles while GNCS-HSC shows 65.9% retention. The VNCS-HSC continued to show impressive improvements in electrochemical performance with 85.1% capacitance retention after 10,000 cycles which is not only higher than NCS-HSC and GNCS-HSC, but also among the highest results reported in literature.[28,103,104,106,108,122,140-143]

Figure 6-10 shows a Ragone plot of all HSCs devices. The calculations are based on the discharge curves using the followings equations:

$$\mathbf{E = 0.5\ C\ \Delta V^2} \qquad \mathbf{(6\text{-}7)}$$

$$\mathbf{P = E/dt} \qquad \mathbf{(6\text{-}8)}$$

Where *E* represents the energy density, *C* is the specific cell capacitance calculated according to **Equation (6-4**) using the total mass of both electrodes, ΔV is the voltage window, *P* is the power density, and *dt* is the discharge time.

The obtained results represent the average value of multiple measurements. Energy densities of 33 Wh kg^{-1}, 41.7 Wh kg^{-1}, and 44.9 Wh kg^{-1} were obtained for NCS-HSC, GNCS-HSC, and VNCS-HSC devices, respectively, at an average power density of 0.87 kW kg^{-1}. VNCS-HSC still exhibits outstanding performance with an energy density of 33.6 Wh kg^{-1} at a high power density of 9 kW kg^{-1}. This remarkable result is 8 times higher than that of NCS-HSC (4.2 Wh kg^{-1}) and significantly higher than that of GNCS-HSC (21.7 Wh kg^{-1}). These results clearly demonstrate that the VNCS-HSC device can provide high power density while

maintain excellent energy density. This excellent performance make VNCS a superior candidate for commercial applications of hybrid supercapacitors.

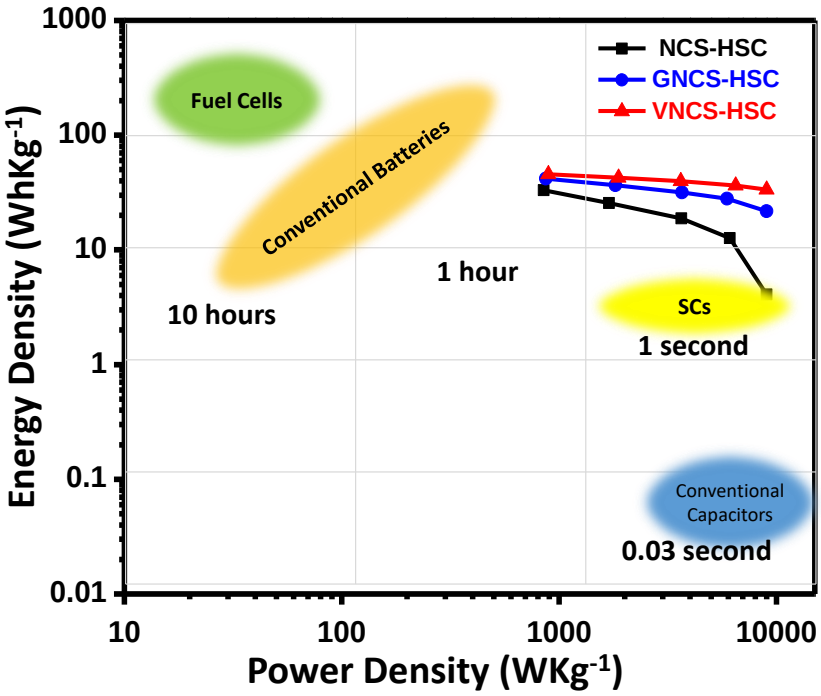

Figure 6-10. Ragone plot showing the relationship between the power density and energy density of all HSC's devices. (reprinted from Ref.[53] , with permission from the Royal Society of Chemistry)

6.5 Chapter conclusion

In conclusion, vanadium-modified $NiCo_2S_4$ nanosheets attached to the surface of graphene sheets was synthesized using a facile solvothermal method, resulting in a homogenous distribution of vanadium even at the atomic level. The V-doped sample showed outstanding

electrochemical performance with a specific capacitance of 1340 F g^{-1} at a low current density of 2 Ag^{-1} and 1024 F g^{-1} at 50 Ag^{-1}. The vanadium-modification of $NiCo_2S_4$ significantly improved the long cycling performance with less than 10^{-3} F/cycle capacitance loss after 10,000 cycles. The material was also tested in a full cell hybrid supercapacitor and showed outstanding electrochemical performance and harmonized synchronization between the EDLC and faradic charge storage kinetics. The resulting hybrid supercapacitor had improved electrochemical performance during charge-discharge operations, remarkable improvement in cycling stability and high energy density at high power densities, making it superior material for hybrid supercapacitors and a potential candidate to bridge the energy/power gap between batteries and supercapacitors.

Chapter 7: Reconciled Nanoarchitecture with Overlapped 2D Anatomy for High Energy Hybrid Supercapacitors

This chapter is reprinted in adjusted format from Ref.[144] with permission from Energy Technology Journal.

Salah Abureden, Fathy M Hassan, Aiping Yu, and Zhongwei Chen, "Reconciled Nanoarchitecture with Overlapped 2D Anatomy for High Energy Hybrid Supercpacitors", accepted manuscript online, May 8 2017, Energy Technology Journal-Wiley-VCH.

7.1 Chapter introduction

The global energy challenges and the increasing demand for reliable and cost-effective energy storage and conversion devices have inspired researchers to explore new materials to meet the growing demand[145]. Lithium ion batteries (LIBs) are one kind of energy storage device based on faradic reactions and are capable of delivering high energy densities with limited power densities[98]. On the other hand, supercapacitors are another kind of energy storage device based on the electrical double layer (EDLC) storage mechanism, and can deliver high power densities with limited energy densities[146]. The idea of creating a hybrid device that can combine the characteristics of both the batteries and supercapacitors have attracted the attention of researchers in the last decade. Researchers have investigated different materials in the faradic parts of the HSC including: metal oxides such as RuO_2,[30] MnO_2,[31] $Li_4Ti_5O_{12}$,[19] V_2O_5[32] and Co_2O_3;[33] metal sulfides such as MoS_2,[34] $NiCo_2S_4$;[35] and, conducting polymers such as polyaniline[36] and polypyrolle.[37] However, despite the recent success in improving the energy

density of the HSC, the low power density and limited cycle life are still challenging factors in energy demanding applications of hybrid supercapacitors.[22]

These changes can be met by the following strategies: 1) use of highly conductive substrate such as graphene can enhance charge transfer kinetics leading to increased stability at higher power rates.[108,122] 2) use of advanced morphologies that can provide wide contact with electrolyte like sheet structure can increase the number of electroactive sites with short diffusion paths.[147,148] 3) the growth of ultra-small nanosize particle on the surface of sheet structure can enhance material stability and provide additional electroactive sites.[149,150] The combination of all these strategies together can lead to increasing the energy density without significant loss of power density

One of the materials that can combine these strategies together is vanadium disulfides which is one type of layered transition-metal dichalcogenides (TMDs) and have great potential in hybrid supercapacitor devices because of its excellent conductivity, distinctive nanosheets structure, and high ion diffusion kinetics.[132,137] However, the difficulty of vanadium disulfide synthesis which requires the use of H_2S atmosphere at high temperatures has limited the interest of researchers in investigating the potential of VS_2 in supercapacitor applications.[151-153] Only two reports have successfully investigated the use of VS_2 in supercapacitor applications using simple synthesis methods. Feng et al.[151] reported the synthesis of few layers VS_2 nanosheets using all in solution route in hydrothermal reaction. The synthesized VS_2 showed high conductivity and considerable specific capacitance of 4760 μFcm^{-2}. Masikhwa et al.[107] reported the use of hydrothermal reaction to synthesis VS_2 nanosheets which was used for the first time

in the fabrication of an asymmetric supercapacitor showing a specific capacitance of 155 F g^{-1} and an energy density of 42 WhKg^{-1} at a power density of 0.70 KW Kg^{-1}. On the other hand, the superior electrical and mechanical characteristics of graphene in addition to its large surface area have motivated enormous number of researchers to investigate its uses in electrochemical devices.

To the best of our knowledge, no report in literature has investigated the use of VS_2 on graphene in a HSC. We here report, for the first time, a unique flower bouquet like structure VS_2 nanosheets with ultra-small VS_2 nanoparticles attached to it and anchored to the surface of graphene nanosheets synthesized using a facile solvothermal method for supercapacitor applications. The material showed superior electrochemical performance achieving 211 F g^{-1} at 1 A g^{-1} and maintaining high capacitance of 135 F g^{-1} even when the current density increased to 20 A g^{-1}. Moreover, the material showed 97 % capacitance retention after 8000 revealing the high potential of this material in HSC applications and opening the door for more investigation in its possible uses.

7.2 Experimental section

This section will introduce the details of the used synthesis method and the electrodes fabrication procedure.

7.2.1 Materials

All chemicals were procured from Sigma Aldrich and used as-received.

7.2.2 Synthesis of VS_2/G:

1 mmol VCl_4 was dissolved in 3 ml DDI and 2 mmol of Thiourea (TU) was dissolved in 2 ml DDI. These two solutions, along with 15 mg of graphene oxide synthesized by modified Hummers' method, were added to 25 ml of ethylene glycol (EG). The mixture was sonicated for 30 minutes and then transferred to a 50 mL Teflon-lined stainless steel autoclave and heated to 120°C for 12 h followed by 220°C for another 12 h (**Figure 7-1**). The solution was left to cool down to room temperature and then filtered and washed by ethanol and DDI three times. The filtered powder was dried at 60°C for 2 h in convection oven followed by 12 h in vacuum oven at 80 °C. Finally, the material was heat-treated in a tube-furnace under argon atmosphere to 300°C for 2 h to improve material purity and crystallinity.

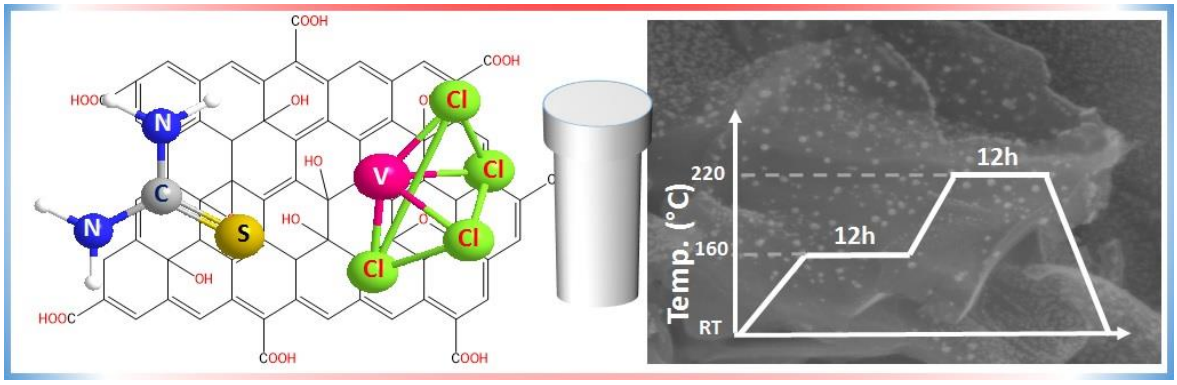

Figure 7-1. Schematic depicting the contents of the precursor solution and the solvothermal treatment parameters. (reproduced in adapted format from Ref.[144] with permission from Energy Technology Journal).

7.3 Characterization

Morphology and chemical structure characteristics were examined by X-ray diffractometer (Rigaku Miniflex 600 X-Ray Diffractometer). BET analysis was done using Folio BET (Micromeritics ASAP 2020). TGA measurement was done with TGA Q500. The XPS was investigated using a PHI Quantera XPS spectrometer. SEM was performed using a ZEISS ULTRA PLUS SEM and TEM analysis was done using a JEOL 2010F TEM/STEM field emission microscope.

Figure 7-2A shows the XRD spectra of VS_2/G. The peaks at 15.38º, 32.10 º, 35.65 º, 45.25 º, 57.20 º, 58.30 º, 59.63 º, 64.85 º and 69.30 º are indexed to (001), (100), (011), (012), (110), (103), (111), (004) and (201) planes respectively indicating pure VS_2 with no impurities (JCPDS 89-1640). However, an additional peak is found at 26.60 º which can be indexed to graphene. The composition and bonding characteristics of the VS_2/G are examined by X-ray photoelectron spectroscopy (XPS). **Figure 7-2 (B-D)** show the XPS spectra of C 1s, S 2p, and V 2p, respectively. The C 1s spectra seen in **Figure 7-2B** reveals a C=C peak at 284.72 eV, the weak peak at 286.28 eV is indexed to C-OH and the peak at 288.80 eV is indexed to the O=C-OH group.[154] **Figure 7-2C** shows the S 2p spectra with two peaks at 162.15 eV and 163.25 eV in addition to a shakeup satellite at 167.08 eV. The peak at 162.15 eV indicates the existence of low coordination sulfur ions at the surface, the other peak at 163.25 eV indicates metal bonding of sulfur.[106,155] The V 2p XPS spectra in **Figure 7-2D** shows two peaks at 513.38 eV and 520.65 eV indicating the +4 valance state of vanadium.[107,129] The XPS chemical

composition measurement revealed 1:1.99 atomic ratio of V: S which is almost identical to stoichiometric ratio of VS_2.

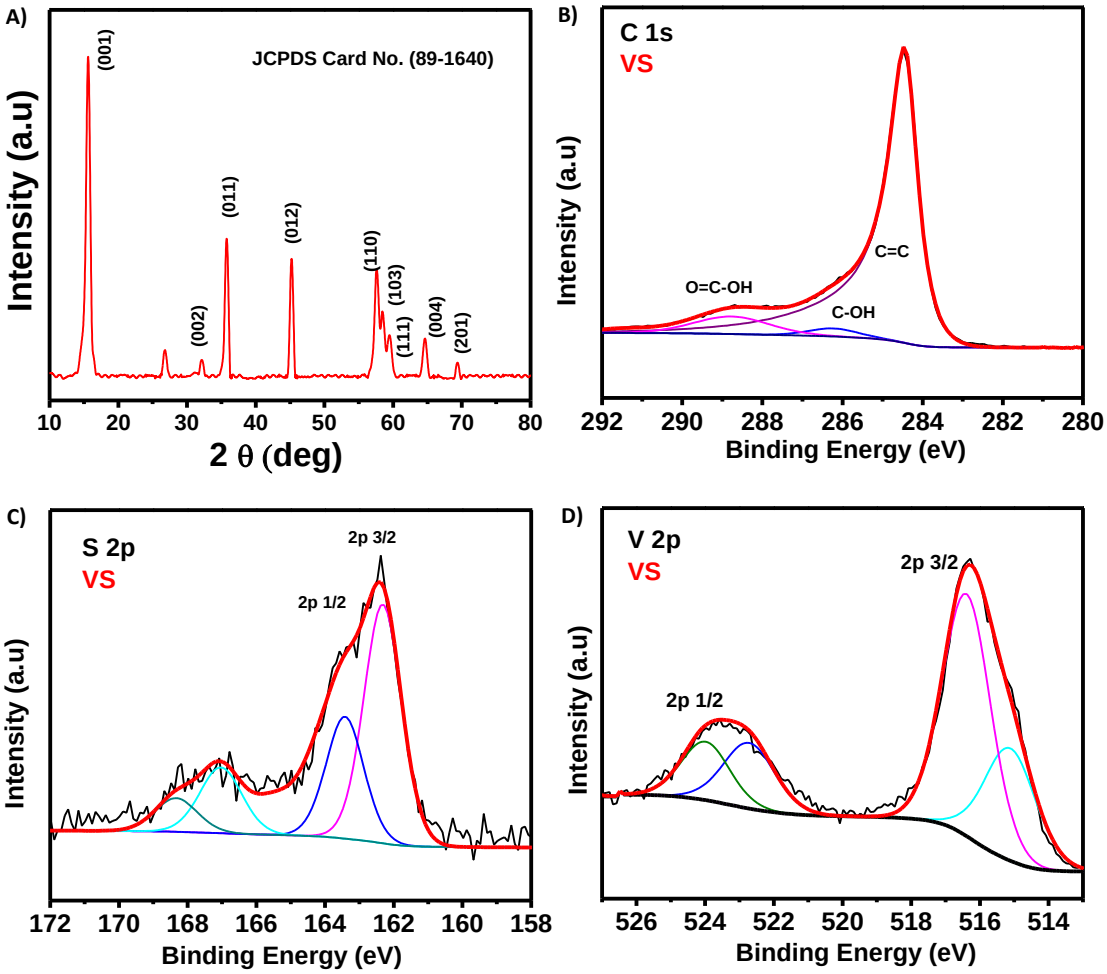

Figure 7-2. A) XRD pattern for the VS2/G showing the standard peaks of VS2 (JCPDS 89-1640) with additional peak at 26.60o indexed to graphene, and B-D) XPS spectra of C 1s, S 2p, and V 2p, respectively. (reproduced in adapted format from Ref.[144] with permission from Energy Technology Journal).

To examine the VS_2 and graphene percentage in the VS_2/G, thermal gravimetric analysis (TGA) was utilized as shown in **Figure 7-3A**. The measurement was carried out under air from room temperature up to 700^{o}C with of 10^{o}C min^{-1} ramp rate. The result shows that the VS_2 is 90.10% (wt. %) of the material. The BET analysis shown in **Figure 7-3B** was conductuted by degassing at 200^{o}C for two hours under vacum. The N_2 adsorption-desorption isotherm is of type IV with an H3 hysteresis loop,[156] the measured BET surface area is 32.3 m^2 g^{-1}.

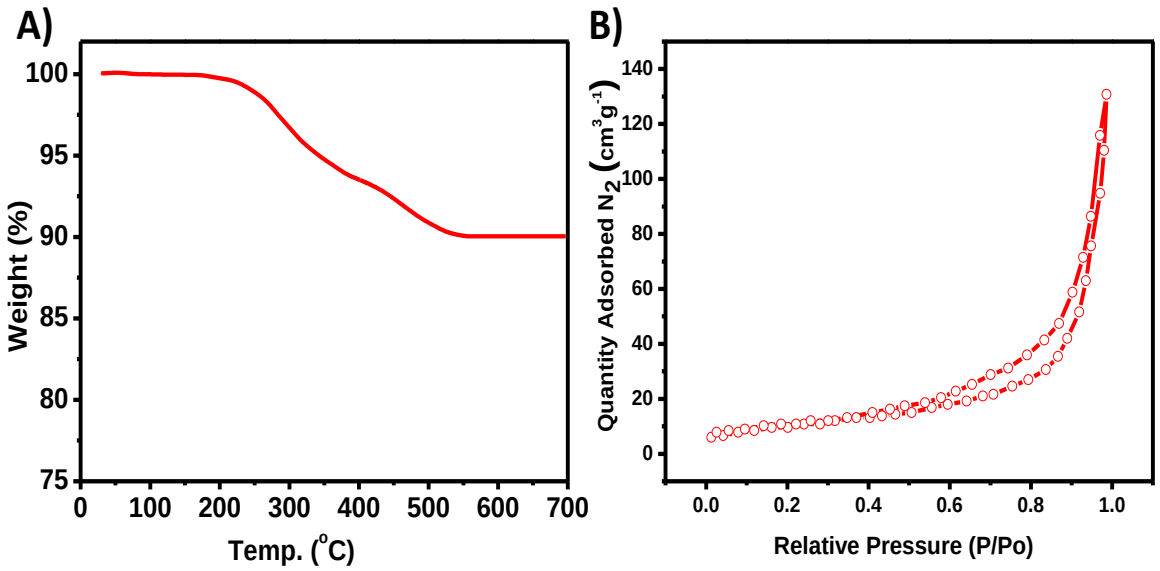

Figure 7-3. A) Thermal gravimetric analysis (TGA) of VS_2/G showing that VS_2 is 90.1 % (wt. %), and B) BET analysis showing type IV N_2 adsorption-desorption isotherm. (reproduced in adapted format from Ref.[144] with permission from Energy Technology Journal).

Figure 7-4 shows the SEM images of VS_2/G. The flower bouquet like nanosheets structure of the material is seen in **Figure 7-4A**. This morphology allows for wider contact area between the electrolyte and the material, leading to an increased number of ion transfer sites and faster charge transfer kinetics.[157,158] **Figure 7-4B** shows how the ultra-small VS_2 nanoparticles are

anchored on the surface of the sheets in a homogenous distribution without agglomeration. **Figure 7-4C** is a higher magnification of the image in **Figure 7-4B** showing the VS_2 nanoparticles in the range of 10-25 nm.

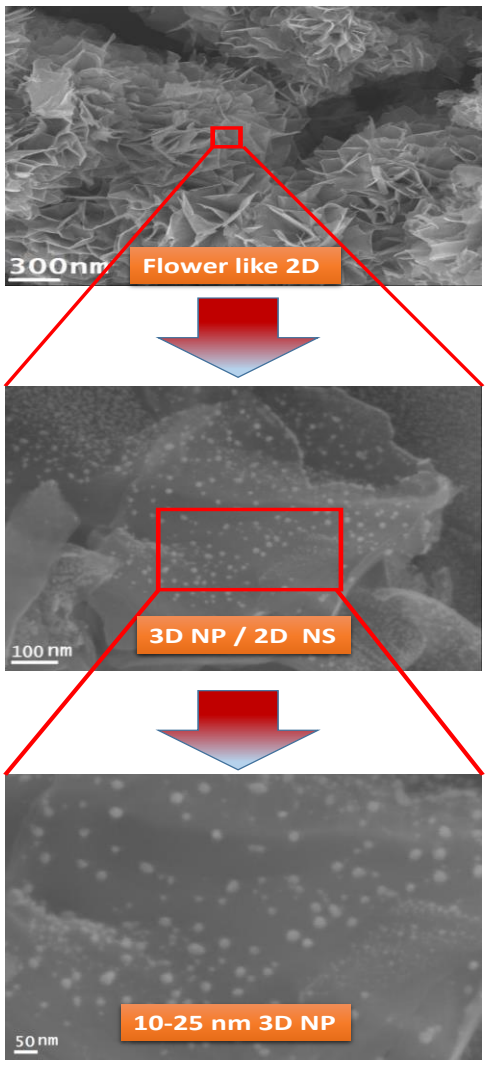

Figure 7-4. A) SEM of the VS_2/G showing the flower bouquet like nanosheets structure in, B) image showing homogenous distribution of VS_2 NP on the surface of the sheets, and C) higher magnification SEM image showing the ultra-small VS_2 NP in the size of 10-25 nm. (reproduced in adapted format from Ref.[144] with permission from Energy Technology Journal).

TEM images are shown in **Figure 7-5**. The TEM image in **Figure 7-5A** shows the VS_2 sheets on graphene nanosheets morphology with the VS_2 prominent nanoparticles adherent to the nanosheets. The inset of **Figure 7-5A** shows the selected area diffraction (SAD) pattern revealing the typical hexagonal symmetry of VS_2/G basal planes.[94] **Figure 7-5B** is a higher magnification HRTEM image of the edge of **Figure 7-5A** clearly showing the ultra-small VS_2 nanoparticles (10-25) nm anchored to the surface of the sheets which agrees with the SEM findings. **Figure 7-5C** shows the lattice spacing of 0.29 nm indexed to plane (001). The high angle annular dark field scanning transmission electron microscopy (HAADF-STEM) image is shown in **Figure 7-5D.** The phase signal **(**bright field) clearly shows the brighter VS_2 nanosheets and nanoparticles on darker graphene sheets, confirming the sheet on sheet structure with prominent nanoparticles. To further investigate this, HAADF-STEM elemental quantification was investigated on area 1 containing prominent nanoparticle and area 2 containing nanosheets (**Figure 7-5E**). The result confirmed the existence of VS_2 in both areas in a stoichiometric ratio of VS_2. Energy dispersive spectroscopy (EDS) analysis was done on the area shown in **Figure 7-5E**. The EDS mapping of carbon, sulfur and vanadium are shown in **Figure 7-5 (F-H)** respectively. The results clearly show the continuous and homogenous distribution of these elements which further confirms the existence of VS_2 across the whole material structure. The electron energy loss spectroscopy (EELS) technique was used to investigate the elemental distribution at the atomic level. The EELS investigation area is shown in **Figure 7-5I**, while **Figure 7-5 (J-L)** show the EELS mapping of carbon, sulfur and vanadium, respectively.

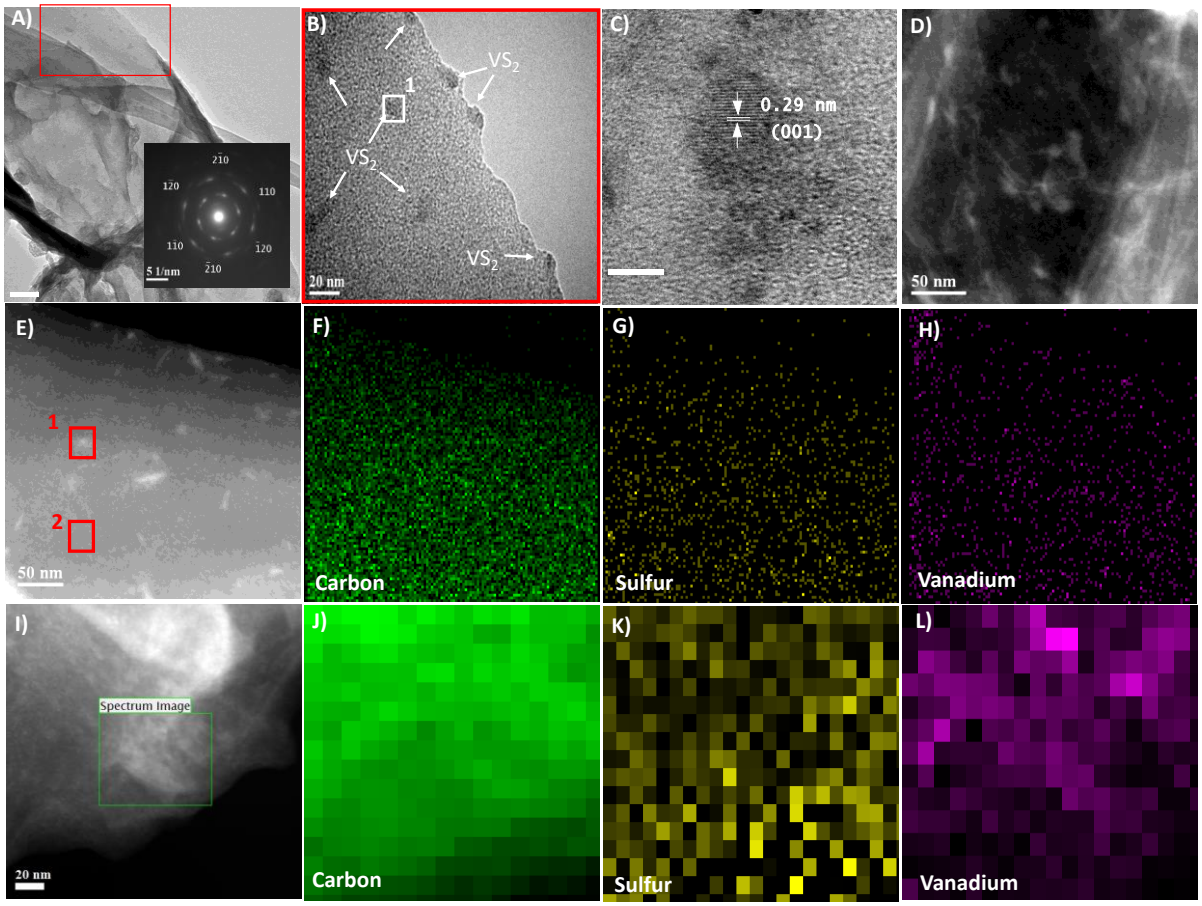

Figure 7-5. A) low magnification TEM showing VS_2/G sheet on sheet with NP morphology, the inset shows the SAD hexagonal structure pattern, B) Higher magnification HRTEM image of the edge of Figure 2D clearly showing the ultra-small VS_2 nanoparticles (10-25) nm on the surface of sheets, C) TEM images showing the d-spacing of plane (001), D) HAADF-STEM image showing contrast in brightness between VS_2 and graphene, E) HAADF-STEM image with elemental quantification on areas 1 and 2. The image was also used for EDS mapping, F-H) EDS mapping of the complete area of image shown in in E for carbon, sulfur and vanadium, respectively, I) EELS investigation area, and J-L) EELS mapping of carbon, sulfur and vanadium, respectively (each pixel is 4 x 4 nm). (reproduced in adapted format from Ref.[144] with permission from Energy Technology Journal).

The results show the harmonized distribution of the elements at the atomic level (each pixel in these images is equivalent to 4 x 4 nm).

The formation of such unique morphology is influenced by the synthesis material and reaction conditions described in the experimental section. The Thiourea (TU) is a reducing and allocating agent and anchors to the surface of the graphene oxide (GO) sheets during the solvothermal treatment due to its high dipole moment[116,159]. This leads to the introduction of sulfur into the basal plane of GO simultaneously with its reduction, yielding sulfur doped graphene (SG).[119-121] When sulfur is introduced into the basal plane of graphene, it is associated with defects.[159] Carbon atoms located on these defects will have higher charge density than the bulk carbon.[159] These sites (containing sulfur and defects) act as nucleation sites for the assembly of the vanadium disulfide nanosheets when TU starts decomposition around 190^{o}C during the solvothermal reaction.[39,116-118] The material morphology suggests that the formation of VS_2 may have followed the Volmer-Weber mode[160-163] where the precursors are populated and anchored to the S-sites on SG, leading to the formation of small nanoparticles of VS_2 over time.[116,164] The particles grow laterally until they eventually coalesce, forming continuous sheets of 2D VS_2, on top of which remain some particles that grown perpendicular to the plan of the 2D sheets of VS_2 as separated islands.[160-162,165] This growth mode has number of advantages. For example: 1) hinders the agglomeration of the material and provides large contact area with electrolyte; and, 2) generates strong covalent interaction of the VS_2 with the graphene surface which explains the long cycling stability.

7.4 Electrochemical performance

The electrochemical performance was evaluated using a three-electrode setup and 2 M KOH electrolyte. For half-cell measurements, active material was used as the working electrode, platinum foil was utilized as counter electrode, and saturated calomel electrode (SCE) acted as reference electrode. For full cell measurements, the working electrode was made of the active material and the counter electrode was made of activated carbon/graphene (AC/G) composite. The working electrodes were made by mixing the active material with super P carbon and polyvinylidenefluoride (PVDF) in 80:10:10 ratio (wt. %). *N*-methyl-pyrrolidone (NMP) was used as the solvent to prepare the slurry which was casted (drop wise) on previously cleaned nickel foam (1.5 x 1.5 cm). The electrodes were then dried in a vacuum oven for 12 hours before being pressed under 0.1 bar. The mass loading of the working electrodes was around 2.10 mg cm^{-2}

Figure 7-6A shows the cyclic voltammetry (CV) measurements of the VS_2/G at several scan rates in a voltage window of (-0.2 – 0.6) V. All curves show two redox peaks indicating faradic behaviour of the material: the anodic peaks resulting from the oxidation of V^{+3} to V^{+4} and the cathodic peak resulting from the reverse process. **Figure 7-6B** shows the galvanostatic charge-discharge measurements at different current densities. All curves show symmetric behaviour during charge and discharge operations, revealing stable charge transfer kinetics and indicating high material stability.[166] It is noticed that all discharge curves show similar behaviour represented in the voltage drop from 0.5 V to ~0.35 V followed by stable voltage decline below 0.35 V until ~0.25 V where a voltage plateau is noticed. This observation is in agreement with

the behaviour of the CV measurements. The voltage plateau is seen more clearly at low current densities of 1 A g^{-1} and 2 A g^{-1} and less clear at higher current densities, which can be attributed to the fast reaction transfer kinetics at high current densities.[167,168] The specific capacitance values shown in **Figure 7-6C** were obtained from the discharge curves using the following well-known equation:[35]

$$C_S = I / (m \Delta V / \Delta t) \qquad \textbf{(7-1)}$$

Where C_S is the specific capacitance (F g^{-1}), I is the discharge current (A), m is the mass of the active material (g), ΔV is the voltage window during discharge measured after the IR drop (V), and Δt is the discharge time (s). A capacitance value of 211 F g^{-1} is achieved at 1 A g^{-1}. This superior capacitance is significantly higher than previously reported capacitance in literature[107,151]. The capacitance maintains 96% of its value at 1 A g^{-1} when the current density is doubled (2 A g^{-1}). 81 % capacitance retention (C.R) was achieved even when the current density increased to 10 A g^{-1} and 64% C.R was achieved at 20 A g^{-1}.

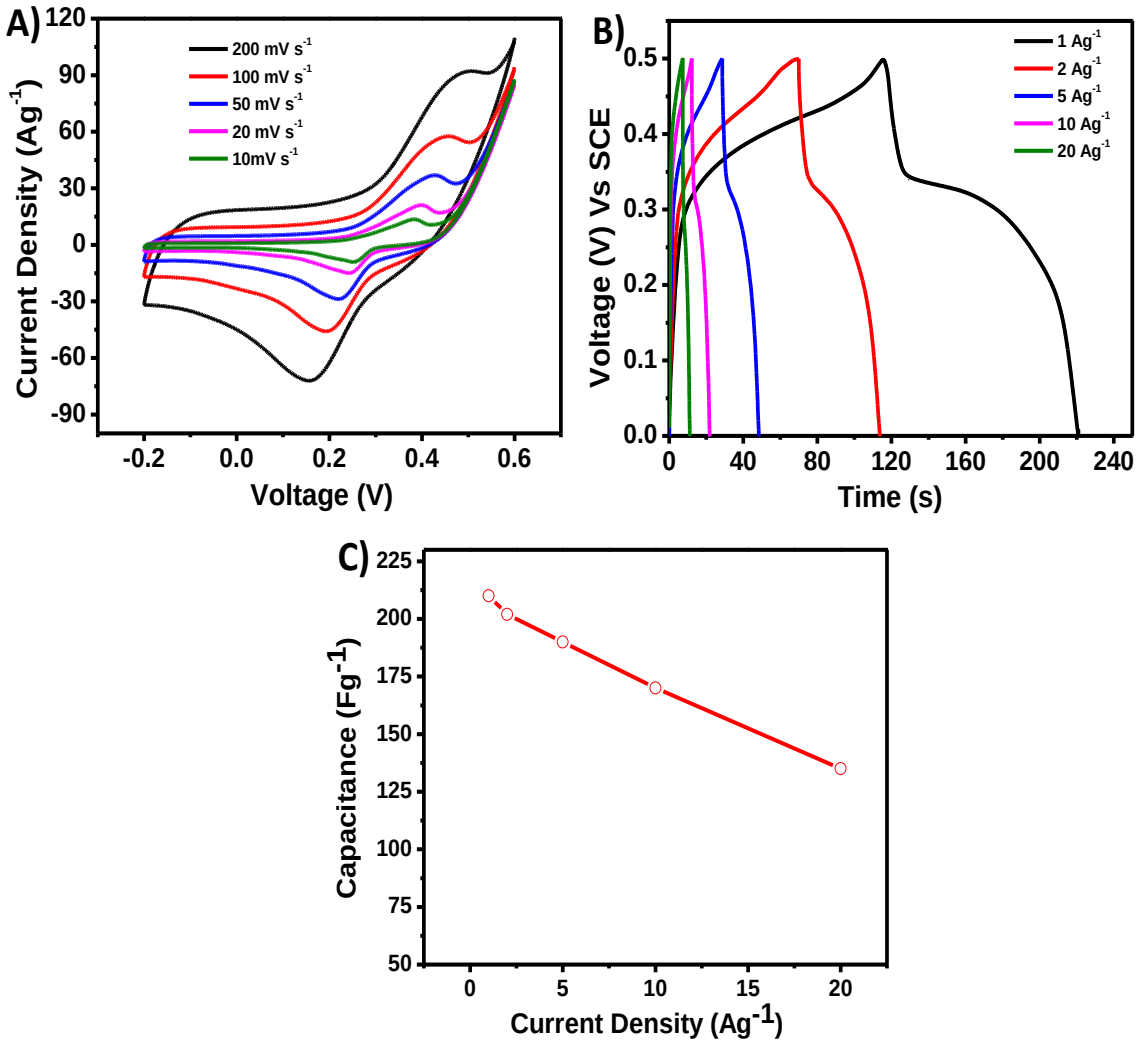

Figure 7-6. A) CV measurements of the VS_2/G at different scan rates, B) CD measurements at different current densities, and C) specific capacitance values at different current densities. (reproduced in adapted format from Ref.[144] with permission from Energy Technology Journal).

The long cycling stability test was performed at 5 A g^{-1} for 8000 cycles as shown in **Figure 7-7.** The result reveals remarkable stability with C.R equal to 98.5 % at cycle 4000 and 97% at cycle 8000. The columbic efficiency was 99.2% and 98.5% at cycles 4000 and 8000, respectively. These results further confirm the high stability of the material and the excellent reversible reaction kinetics.

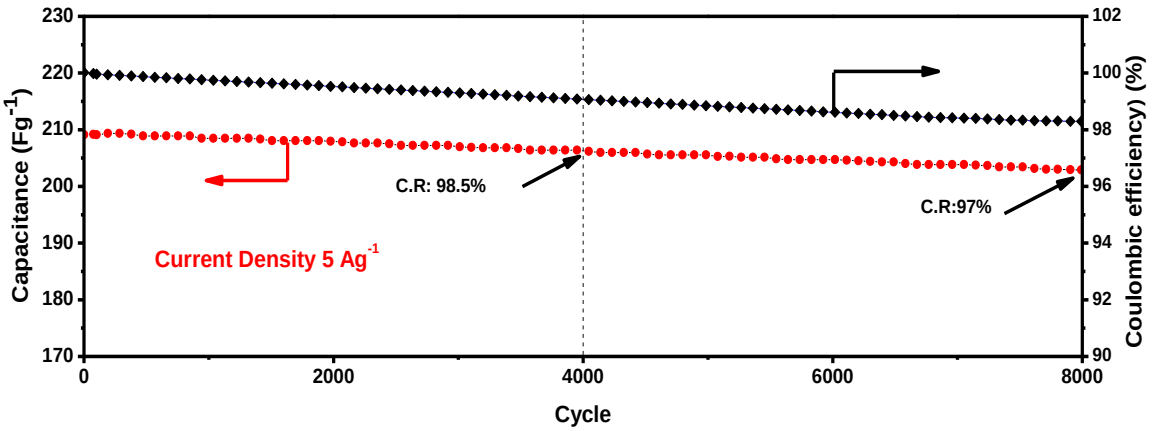

Figure 7-7. Long cycling stability test at 5 A g^{-1} for 8000 cycles. (reproduced in adapted format from Ref.[144] with permission from Energy Technology Journal).

These distinguished results can be attributed to the unique morphology of VS_2/G, the use of graphene as highly conductive substrate and the presence of ultra small nano-size VS_2 nanoparticles uniformly attached to the sheets. These characteristics lead to an increase in capacitance due to the increase in the number of electroactive sites, improved the charge transfer kinetics and provided shorter ion diffusion pathway resulting in stable and reversible charge transfer processes.[155,169] For further investigation on the electrochemical performance of VS_2/G, we fabricated a hybrid supercapacitor (HSC) using VS_2/G as the positive electrode and activated carbon/graphene (AC/G) composite as the negative electrode (AC:G is 9:1

wt.%), electrodes were prepared using the same drop casting method and weight ratio described earlier. The mass ratio of the two electrodes on the sides of HSC was carefully controlled to balance the charge resulting from the two different charge transfer kinetics, where VS_2/G generates charge using faradic reactions and AC/G generates charge using EDLC. The specific capacitance of AC/G is 168 F g^{-1} calculated from the charge-discharge measurement seen in **Figure 7-8A.** The N2 adsorption- desorption isotherm of AC/G electrode is shown in **Figure B-10C (Appendix B)** (BET surface area 2120 m^2g^{-1}).The mass ratio was balanced using the following equations:[170]

$$\mathbf{q = C\,\Delta V\,m} \qquad \mathbf{(7\text{-}2)}$$

$$\mathbf{m^+/m^- = C^-\,\Delta V^-\,/\,(C^+\,\Delta V^+)} \qquad \mathbf{(7\text{-}3)}$$

Where *q* is the charge, *m* is the mass of the material on the electrode, *C* is specific capacitance (F g^{-1}) and ΔV is the voltage range.

The electrochemical performance investigations were done in 2 M KOH electrolyte and in a wider voltage window of (0-1.6) V determined based on the voltage range of the individual electrodes of the HSC device. **Figure 7-8B** shows the CV measurement of HSC at different scan rates. Both battery like behaviour obtained from faradic reactions and standard EDLC behaviour can be seen in the CV curves indicating the contribution of both electrodes simultaneously in the overall capacitance of the HSC device. The behaviour of the curves did not change noticeably at all scan rates, indicating highly efficient reversible charge exchange processes between the two sides of the HSC and harmonized synergy between the two reaction mechanisms at the cathode and anode.[104,140] **Figure 7-8C** shows the galvanostatic charge-

discharge measurements of the HSC at several current rates, the curves show symmetric processes of charge gain and release with both faradic and EDLC behaviours observed. This further confirms the high synergy between the different reactions mechanisms on both sides of HSC attributed to the high stability of electrodes. The specific capacitance values shown in **Figure 7-8D** were calculated using **Equation 7-1** above based on the total mass of active material on both electrodes. The HSC shows excellent stability and capacitance retention as current density increases, with 91.0% C.R at 2 A g^{-1} compared to the capacitance at 1 A g^{-1} and 51.0% C.R when the current density increased 20 times (20 A g^{-1}). **Figure 7-9** shows the long cycling test at 5A g^{-1}. The HSC device shows outstanding C.R of 99.5 % after 4000 cycles and 99.1 % even after 8000 cycles compared to the capacitance at cycle 1.

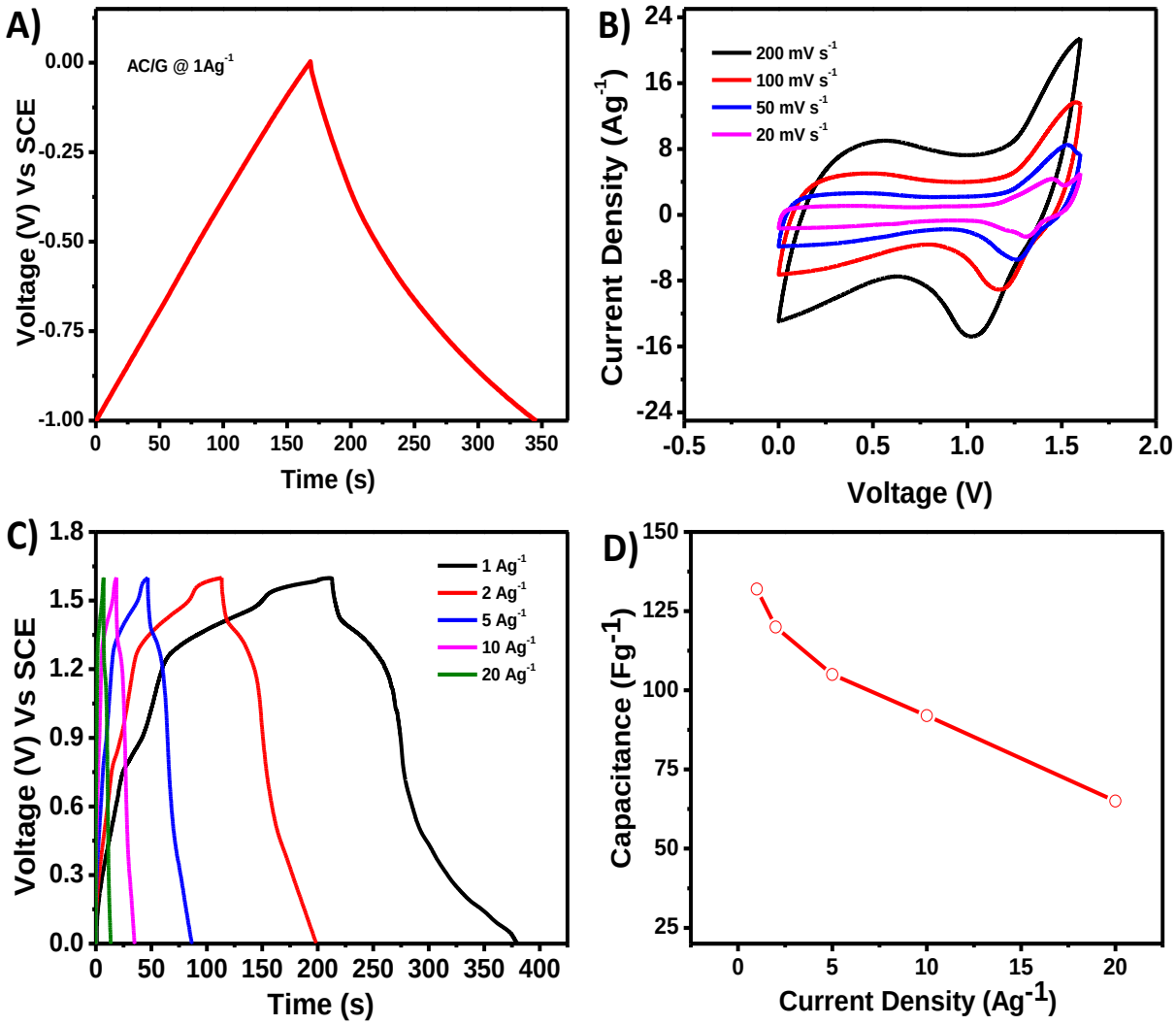

Figure 7-8. A) CD measurement of AC/G electrode at 1A g^{-1}, B) CV measurement of HSC at different scan rates, C) CD measurement of HSC at different current densities, and D) HSC specific capacitance values obtained at different current densities. (reproduced in adapted format from Ref.[144] with permission from Energy Technology Journal).

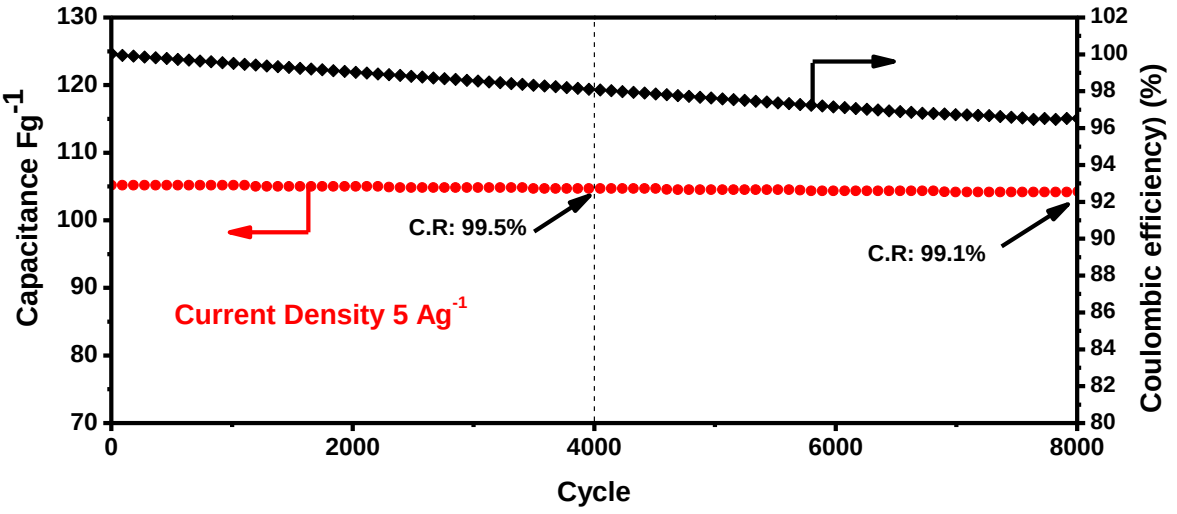

Figure 7-9. Long cycling test of HSC for 8000 cycles at 5A g^{-1}. (reproduced in adapted format from Ref.[144] with permission from Energy Technology Journal).

The electrochemical impedance spectroscopy (EIS) measurement before and after long cycling is shown in **Figure 7-10A**. The Nyquist plot reveals a small change in the solution resistance (Rs) and charge-transfer resistance (Rct) before and after cycling. The Rs values were 0.85 Ω before cycling and 1.55 Ω after the long cycling. While Rct value were 3.25 Ω before cycling and 4.75 Ω after cycling. The high slope of the curves in the low frequency region before and after cycling suggests a small diffusion resistance.[171] These results indicate high device stability.

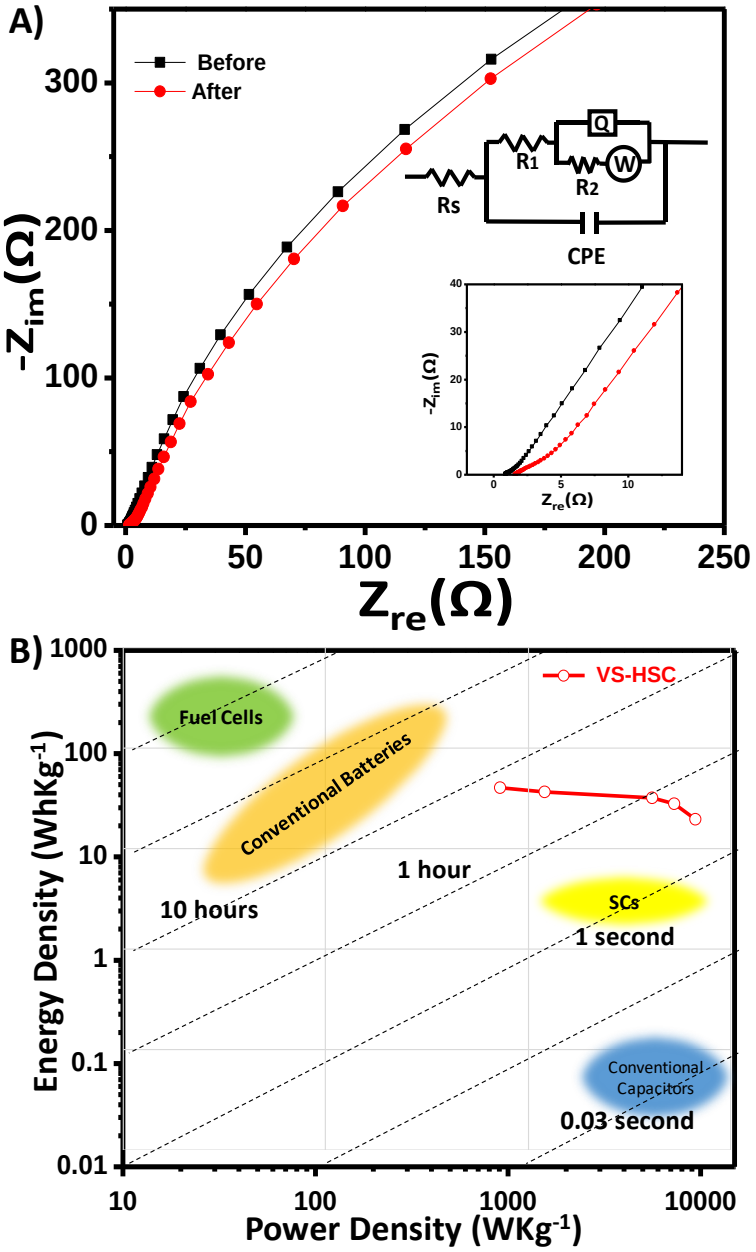

Figure 7-10. A) EIS measurement of the HSC device before and after long cycling with the circuit model showed, the inset shows the low frequency region in the Nyquist plot, and B) Ragone plot of the HSC device. (reproduced in adapted format from Ref.[144] with permission from Energy Technology Journal).

Figure 7-10B shows a Ragone plot of the HSC device. The energy and power densities were obtained using the following equations:[172]

$$E = 0.5\ C\ \Delta V^2 \qquad (7\text{-}4)$$

$$P = E/dt \qquad (7\text{-}5)$$

Where E is the energy density, C is the specific capacitance, ΔV is the discharge voltage range, P is the power density, and dt is the discharge time. The obtained results represent the average value of multiple measurements. The HSC showed an energy density of 46.93 Wh kg^{-1} at a power density of 0.91 kW kg^{-1} and retained a high energy density even when the power density was 10 times higher, showing 23.11 Wh kg^{-1} at 9.40 kW kg^{-1}. This remarkable retention of energy density demonstrates that such material can be ideal for applications requiring long life and high energy retention at high power rates.

The outstanding electrochemical performance can be ascribed to the inimitable material morphology. The nanosheets on nanosheets structure, the ultra-small size of VS_2 nanoparticles and the presence of graphene nanosheets have improved ion migration inside the electrode material,[173] enhanced charge transfer kinetics,[174,175] provided large accessibility of electrolyte ions to charge the double layer, and increased the number of electroactive sites with shorter diffusion paths leading to improved capacitance and faster charge transfer kinetics.

7.5 Chapter conclusion

In conclusion, we have successfully synthesised a distinctive flower bouquet-like VS_2 nanosheets structure with ultra-small VS_2 nanoparticles (10-25 nm) adherent to it and laying on the surface of graphene nanosheets using simple solvothermal process. The material showed

superior electrochemical performance with 211 F g^{-1} at 1 A g^{-1} and superior long cycling performance (8000 cycles) at 5 A g^{-1} with 97% capacitance retention and excellent columbic efficiency. The material was used to fabricate a hybrid supercapacitor (HSC) showing outstanding capacitance of 132 F g^{-1} at 1 A g^{-1} with remarkable cyclability and capacitance retention. The HSC gave an energy density of 46.93 Wh kg^{-1} at a power density of 0.91 kW kg^{-1} and an excellent energy density of 23.11 Wh kg^{-1} even at a high power density of 9.40 kW kg^{-1}. To the best of our knowledge, this is the first report of such a material for HSC applications. This material is a very promising candidate for bridging the gap between battery and supercapacitor technologies.

Chapter 8: Conclusion and Future Work

This chapter provides a summary of the work reported throughout this thesis and recommendations for future projects in order to capitalize on the scientific achievements reported.

8.1 Summary and conclusion

The main objective of this thesis is to develop new and unique nanostructure faradic materials capable of providing high energy density without sacrificing the power density for hybrid supercapacitor applications. The hypothesis is to combine half a battery, made of novel materials, and half a supercapacitor, made from carbon-based materials, in one cell. This will enable operation at larger voltage windows, and coupled with careful control of the charge transfer kinetics on each electrode in HSC device will lead to the delivery of higher energy densities at high power densities, and a longer life cyclability with minimal capacitance reduction. To achieve this, effective modifications to the intrinsic characteristics of selected materials were made so that the developed materials can have increased number of electroactive sites, improved conductivity, wider contact area with electrolyte, short diffusion pathways and fast charge transfer kinetics. The research strategy process included “cyclic-investigation” approach with in-depth analysis of the output for the continuous improvements analysis. Using simple, safe, inexpensive and scalable production methods are also important objectives in this work. All the developed materials were synthesized meeting the above criteria. This can open the door for future commercialization of the developed materials.

Number of characterization techniques were utilized to investigate the morphology and chemical composition of the developed materials including XRD, XPS, Raman spectroscopy, TGA, SEM and TEM. The electrochemical performance was evaluated using different techniques including galvanostatic charge- discharge, cyclic voltammetry, rate capability, long cycling durability and electrochemical impedance spectroscopy.

Three classes of materials with tuned structure and morphology were developed using. The developed materials are: 1) multigrain electrospun nickel doped 1D lithium titanate nanofibers, 2) vanadium-modified chalcogens with 2D/2D tuned nano-architecture, and 3) reconciled vanadium-disulfide 2D nanosheets on graphene nanosheets with 3D prominent vanadium-disulfide nanoparticles anchored to the surface of the sheets. The summary and conclusion for the work done on each one of these materials is discussed below.

8.1.1 Multigrain electrospun nickel doped lithium titanate nanofibers

A novel in-situ nickel doped 1-D lithium titanate nanofibers (Li_4Ti_5-xNi_xO_{12}, where x=0, 0.05 and 0.1) have been successfully synthesized using a facile electrospinning process. Physical characterization reveals that nickel is homogeneously incorporated into the lattice of lithium titanate nanofibers (LTONF), which significantly improves their properties yielding an outstanding electrochemical performance in a lithium ion battery at high rate rates and a significant reduction in the voltage gap between the oxidation and reduction peaks. A capacity of 190 mA h g^{-1} has been obtained at 0.2 C for the 10% nickel doped nanofibers (Ni-$LTONF_{10}$), which is higher than the theoretical capacity of pristine lithium titanate (175 mA h g-1). This highlights the superior rate capability resulting in 63 mA h g^{-1} obtained at 50 C, which is 20

times higher than that of un-doped pristine LTONF and lithium titanate nanoparticles (LTONP). Lastly, a hybrid supercapacitor was fabricated using Ni-LTONF$_{10}$, showing superior energy density of 60 Wh kg^{-1} at power density of 1.5 kW kg^{-1} and retained a high energy density of 35 Wh kg^{-1} at 5 kW kg^{-1}.

8.1.2 Modified chalcogens with tuned nano-architecture

Vanadium-modified $NiCo_2S_4$ wrapped with graphene sheets (VNCS) was synthesized using a simple solvothermal technique. The VNCS demonstrated superior electrochemical performance over graphene-wrapped $NiCo_2S_4$ (GNCS) and pure $NiCo_2S_4$ (NCS) samples, with a specific capacitance of 1340 F g^{-1} at a current density of 2 Ag^{-1}. The VNCS also showed outstanding capacitance retention at 50 Ag^{-1} (1024 Fg^{-1}), which is 430 % higher than NCS sample. The cycling stability of VNCS significantly improved by more than 140% compared to that of the NCS sample, with less than 10^{-3} F/cycle loss in capacitance after 10,000 cycles. We also report the fabrication of a hybrid supercapacitors (HSC's) using the three different materials for the faradic electrode. The VNCS-HSC showed significant improvements in all electrochemical performance measurements compared to NCS-HSC. The capacitance retention at 50 Ag^{-1} improved by more than 260% and the long cycling stability improved by more than 180% after 10,000 cycles. The VNCS-HSC delivered an energy density of 45.9 Wh kg^{-1} at 0.87 kW kg^{-1} and maintained a superior energy density of 33.6 Wh kg^{-1} at 9 kW kg^{-1} indicating the excellent potential of this material in hybrid super capacitor applications.

8.1.3 Reconciled nanoarchitecture with overlapped 2D anatomy vanadium di-sulfide

A unique and novel, flower bouquet-like, vanadium di-sulfide (VS_2) nanosheets structure with ultra-small prominent VS_2 nanoparticles (10-25 nm) on its surface and anchored on the surface of graphene nanosheets (VS_2/G) was synthesized by a facile solvothermal method. The material showed superior electrochemical performance when tested in supercapacitors, achieving 211 F g^{-1} at 1 A g^{-1}, 135 F g^{-1} at 20 A g^{-1} and 97 % capacitance retention after 8000 cycles at 5 A g^{-1} with high columbic efficiency. The material was used to fabricate a full cell, hybrid supercapacitor (HSC) showing 132 F g^{-1} at 1 A g^{-1} with remarkable cyclability up to 8000 cycles at 5 A g^{-1} losing less than $1x10^{-4}$ F/cycle. The HSC demonstrated an excellent energy density of 46.93 Wh kg^{-1} at a power density of 0.91 kW kg^{-1} and retained a high energy density of 23.11 Wh kg^{-1} even when the power density increased ten-fold (9.40 kW k g^{-1}). This unique material synthesized by a facile method is a very promising candidate for the next generation of energy storage technologies that can fill the gap between batteries and supercapacitors devices.

8.2 Proposed future work

The achievements reported in this thesis are the first important step in a long term approach to manufacture high performance hybrid supercapacitors devices capable of bridging the technology gap between LIBs and SCs. It is suggested that future work be built upon the findings of this thesis. Future projects should focus on the followings: 1) development of thick electrodes with high mass loadings; such project can evaluate the promising potential of the developed materials in providing higher energy and power densities. 2) design and development

of multi-stack structure HSC device; such project will entail a framework to scale up the developed materials from lab-scale to industrial-scale. Lastly, 3) to investigate further improvements on the developed materials and their uses in other energy storage technologies.

8.2.1 Thick electrodes

The changes to intrinsic properties of the developed materials helped in matching and maintaining synchronized rates of charge transfer on both sides of the HSC device even at high power rates. Building on this, and with the synthesis methods and physicochemical properties of the developed materials well established, it is highly recommended to exploit this to fabricate thick electrodes which can provide higher energy and power densities. This can be achieved by introducing changes to the design of the HSC device in order to accommodate the additional mass loading. For example, pouch cell implementations can be a good choice for such undertaking. However, the high mass loading on thick electrodes require additional amounts of active materials, binders and conductive carbon. This makes it is extremely important for such a study to carefully control the colloidal chemistry and adhesion properties, to ensure electrode stability and minimal energy density reduction.

8.2.2 Multi-stack device

The simplicity, scalability and low cost of the synthesis methods in addition to the availability of the used raw materials in abundant amounts pave the way for the scale-up of the developed materials from lab scale to industrial scale. It is also recommended to investigate the design and development of multi-stack HSC device, similar to the design in **Figure 8-1**. Such project can focus on optimizing the production parameters to produce larger quantities of the materials.

This should be done simultaneously with the design and development of a compact device, i.e. using thinner current collectors to minimize the weight and size of the device and to allow for more layers of the active material to be stacked together. For large-scale production, it is also important to study the possibility of using water as a solvent during the cell assembly as an alternative to N-methyl pyrrolidone (NMP) which can generate flammable vapors when produced in large quantities. The use of water can also reduce the production cost. However, the solubility of materials in water need to be taken into consideration in such study.

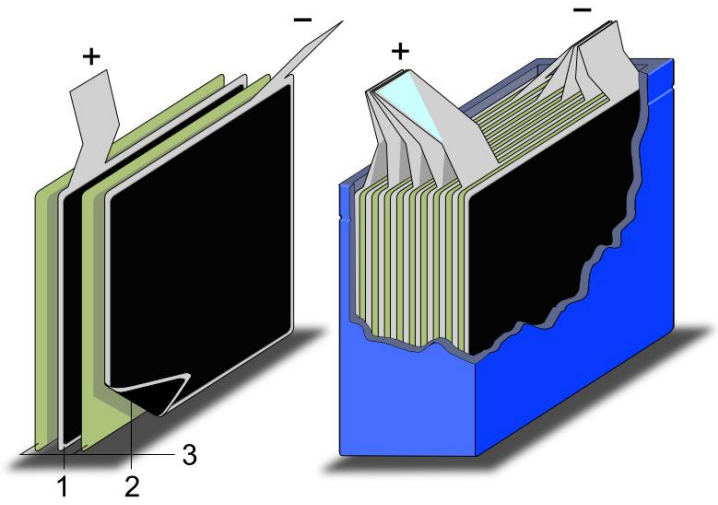

Figure 8-1. Schematic illustration for supercapacitor with stacked electrodes, 1. Positive electrode, 2. Negative electrode and, 3. Separator. (Source is Wikipedia, www.wikipedia.com)

8.2.3 Further material development and application

While the developed materials reported in this work showed remarkable electrochemical performance in hybrid supercapacitor applications. There is still room for improvements in the material design and production methods to attain further improved performance. For example, in the case of 1D Ni-LTONF, the use of modified core-shell electrospinning (**Figure 8-2**) with

Ni-LTONF precursor in the outer needle and the nickel salt precursor in the inner needle might allow for the encapsulation of nickel inside the Ni-LTONF nanofibers.

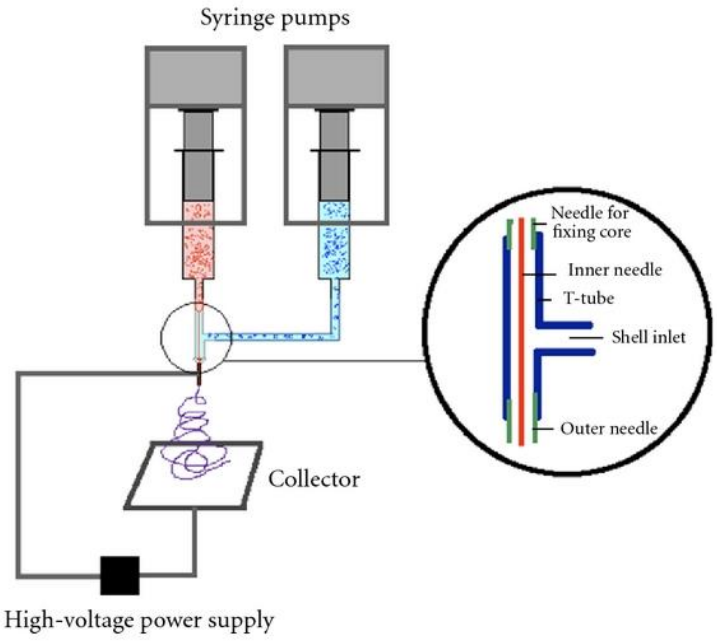

Figure 8-2 Schematic illustration of the core-shell setup for electrospinning hollow fibers. (reprinted from Ref.[176] with permission from Journal of Nanotechnology, open access distributed under the creative commons attribution license)

If this is achievable, it might lead to enhanced conductivity and cyclability. However, such a project will need a thorough investigation of the effect of the production parameters on the produced nanofibers. For example, the effect of the competing electrical forces on the outer diameter of the nanofibers need to be considered. The relationship between the material

viscosity and applied voltage versus the injection speed and distance and their effect on the physicochemical properties and material nanofibers stability should also be evaluated.

In the case of modified binary chalcogens and VS_2/G materials, it is suggested that the future work should consider the development of 3D nano-architectures, by growing 1D structure (i.e. carbon nanotubes or silicon nanowires) vertically on the surface of a developed 2D material, as incubation substrate. The 1D material will act as accelerated ion delivery network providing additional capacitance and faster reaction kinetics. Chemical vapor deposition might be a good approach for this material preparation.

Finally, it is also suggested that future projects should investigate the use of the developed materials in other energy storage devices such as lithium sulfur and sodium ion batteries.

Reference

1 Chu, S. & Majumdar, A. Opportunities and challenges for a sustainable energy future. *Nature* **488**, 294-303 (2012).

2 Zhu, G.-N., Wang, Y.-G. & Xia, Y.-Y. Ti-based compounds as anode materials for Li-ion batteries. *Energy & Environmental Science* **5**, 6652-6667, doi:10.1039/c2ee03410g (2012).

3 Ding, Z. *et al.* Towards understanding the effects of carbon and nitrogen-doped carbon coating on the electrochemical performance of Li4Ti5O12 in lithium ion batteries: a combined experimental and theoretical study. *Physical Chemistry Chemical Physics* **13**, 15127-15133, doi:10.1039/c1cp21513b (2011).

4 Yi, T.-F., Yang, S.-Y. & Xie, Y. Recent advances of Li4Ti5O12 as a promising next generation anode material for high power lithium-ion batteries. *Journal of Materials Chemistry A* **3**, 5750-5777, doi:10.1039/c4ta06882c (2015).

5 Choi, J. W. & Aurbach, D. Promise and reality of post-lithium-ion batteries with high energy densities. *Nature Reviews Materials* **1**, 16013, doi:10.1038/natrevmats.2016.13 http://www.nature.com/articles/natrevmats201613#supplementary-information (2016).

6 Sharma, P. & Bhatti, T. S. A review on electrochemical double-layer capacitors. *Energy Conversion and Management* **51**, 2901-2912, doi:http://dx.doi.org/10.1016/j.enconman.2010.06.031 (2010).

7 Wang, G., Zhang, L. & Zhang, J. A review of electrode materials for electrochemical supercapacitors. *Chem. Soc. Rev.* **41**, 797-828, doi:10.1039/c1cs15060j (2012).

8 González, A., Goikolea, E., Barrena, J. A. & Mysyk, R. Review on supercapacitors: Technologies and materials. *Renewable and Sustainable Energy Reviews* **58**, 1189-1206, doi:http://dx.doi.org/10.1016/j.rser.2015.12.249 (2016).

9 Newswire, P. in *PR Newswire* (2014).

10 report, R. a. m. a. Global batteries & supercapacitors in consumer electronics market 2013-2023: Forecasts, opportunities, innovation. *Entertainment Close - Up* (2014).

11 Kumar, A. & Jena, H. M. Preparation and characterization of high surface area activated carbon from Fox nut (Euryale ferox) shell by chemical activation with H3PO4. *Results in Physics* **6**, 651-658, doi:http://doi.org/10.1016/j.rinp.2016.09.012 (2016).

12 Yu, A. *Electrochemical supercapacitors for energy storage and delivery : fundamentals and applications*. (CRC press, 2013).

13 Goodenough, J. B. & Park, K.-S. The Li-Ion Rechargeable Battery: A Perspective. *Journal of the American Chemical Society* **135**, 1167-1176, doi:10.1021/ja3091438 (2013).

14 Mekonnen, Y., Sundararajan, A. & Sarwat, A. I. in *SoutheastCon 2016*. 1-6.

15 Deng, D. Li-ion batteries: basics, progress, and challenges. *Energy Science & Engineering* **3**, 385-418, doi:10.1002/ese3.95 (2015).

16 Yoshino, A. The Birth of the Lithium-Ion Battery. *Angewandte Chemie International Edition* **51**, 5798-5800, doi:10.1002/anie.201105006 (2012).

17 Vlad, A. *et al.* Hybrid supercapacitor-battery materials for fast electrochemical charge storage. *Scientific Reports* **4**, 4315, doi:10.1038/srep04315 http://www.nature.com/articles/srep04315#supplementary-information (2014).

18 Yi, R. *et al.* High-Performance Hybrid Supercapacitor Enabled by a High-Rate Si-based Anode. *Advanced Functional Materials* **24**, 7433-7439, doi:10.1002/adfm.201402398 (2014).

19 Abureden, S. *et al.* Multigrain electrospun nickel doped lithium titanate nanofibers with high power lithium ion storage. *Journal of Materials Chemistry A* **4**, 12638-12647, doi:10.1039/C6TA04046B (2016).

20 Choudhary, N. *et al.* Asymmetric Supercapacitor Electrodes and Devices. *Advanced Materials*, 1605336-n/a, doi:10.1002/adma.201605336 (2017).

21 Hsu, L. C. & Sheibley, D. W. Inexpensive Cross-Linked Polymeric Separators Made from Water-Soluble Polymers. *Journal of The Electrochemical Society* **129**, 251-254, doi:10.1149/1.2123807 (1982).

22 Yan, J., Wang, Q., Wei, T. & Fan, Z. Recent Advances in Design and Fabrication of Electrochemical Supercapacitors with High Energy Densities. *Advanced Energy Materials* **4**, 1300816-n/a, doi:10.1002/aenm.201300816 (2014).

23 Jiang, H., Li, C., Sun, T. & Ma, J. A green and high energy density asymmetric supercapacitor based on ultrathin MnO2 nanostructures and functional mesoporous

carbon nanotube electrodes. *Nanoscale* **4**, 807-812, doi:10.1039/C1NR11542A (2012).

24 Augustyn, V. *et al.* High-rate electrochemical energy storage through Li+ intercalation pseudocapacitance. *Nat Mater* **12**, 518-522, doi:10.1038/nmat3601 http://www.nature.com/nmat/journal/v12/n6/abs/nmat3601.html#supplementary-information (2013).

25 Zhi, M., Xiang, C., Li, J., Li, M. & Wu, N. Nanostructured carbon-metal oxide composite electrodes for supercapacitors: a review. *Nanoscale* **5**, 72-88, doi:10.1039/C2NR32040A (2013).

26 Dubal, D. P., Ayyad, O., Ruiz, V. & Gomez-Romero, P. Hybrid energy storage: the merging of battery and supercapacitor chemistries. *Chemical Society Reviews* **44**, 1777-1790, doi:10.1039/C4CS00266K (2015).

27 Naoi, K., Ishimoto, S., Miyamoto, J.-i. & Naoi, W. Second generation 'nanohybrid supercapacitor': Evolution of capacitive energy storage devices. *Energy & Environmental Science* **5**, 9363-9373, doi:10.1039/C2EE21675B (2012).

28 Yang, C.-S., Jang, Y. S. & Jeong, H. K. Bamboo-based activated carbon for supercapacitor applications. *Current Applied Physics* **14**, 1616-1620, doi:http://dx.doi.org/10.1016/j.cap.2014.09.021 (2014).

29 Faraji, S. & Ani, F. N. The development supercapacitor from activated carbon by electroless plating—A review. *Renewable and Sustainable Energy Reviews* **42**, 823-834, doi:http://dx.doi.org/10.1016/j.rser.2014.10.068 (2015).

30 Subramanian, V., Hall, S. C., Smith, P. H. & Rambabu, B. Mesoporous anhydrous RuO2 as a supercapacitor electrode material. *Solid State Ionics* **175**, 511-515, doi:http://dx.doi.org/10.1016/j.ssi.2004.01.070 (2004).

31 Yu, G. *et al.* Enhancing the Supercapacitor Performance of Graphene/MnO2 Nanostructured Electrodes by Conductive Wrapping. *Nano Letters* **11**, 4438-4442, doi:10.1021/nl2026635 (2011).

32 Wei, D. *et al.* A Nanostructured Electrochromic Supercapacitor. *Nano Letters* **12**, 1857-1862, doi:10.1021/nl2042112 (2012).

33 Dong, X.-C. *et al.* 3D Graphene–Cobalt Oxide Electrode for High-Performance Supercapacitor and Enzymeless Glucose Detection. *ACS Nano* **6**, 3206-3213, doi:10.1021/nn300097q (2012).

34 Acerce, M., Voiry, D. & Chhowalla, M. Metallic 1T phase MoS2 nanosheets as supercapacitor electrode materials. *Nat Nano* **10**, 313-318, doi:10.1038/nnano.2015.40 http://www.nature.com/nnano/journal/v10/n4/abs/nnano.2015.40.html#supplementary-information (2015).

35 Abureden, S. A. *et al.* Modified Chalcogens with Tuned Nano-Architecture for High Energy Density and Long Life Hybrid Supercapacitor. *Journal of Materials Chemistry A*, doi:10.1039/C7TA00897J (2017).

36 Wang, R. *et al.* Hydrothermal synthesis of nanostructured graphene/polyaniline composites as high-capacitance electrode materials for supercapacitors. *Scientific Reports* **7**, 44562, doi:10.1038/srep44562

http://www.nature.com/articles/srep44562#supplementary-information (2017).

37 Huang, Y. *et al.* Nanostructured Polypyrrole as a flexible electrode material of supercapacitor. *Nano Energy* **22**, 422-438, doi:http://dx.doi.org/10.1016/j.nanoen.2016.02.047 (2016).

38 Wilm, M. S. & Mann, M. Electrospray and Taylor-Cone theory, Dole's beam of macromolecules at last? *International Journal of Mass Spectrometry and Ion Processes* **136**, 167-180, doi:10.1016/0168-1176(94)04024-9.

39 Wu, J., Wang, N., Zhao, Y. & Jiang, L. Electrospinning of multilevel structured functional micro-/nanofibers and their applications. *Journal of Materials Chemistry A* **1**, 7290-7305, doi:10.1039/C3TA10451F (2013).

40 Zhang, B., Kang, F., Tarascon, J.-M. & Kim, J.-K. Recent advances in electrospun carbon nanofibers and their application in electrochemical energy storage. *Progress in Materials Science* **76**, 319-380, doi:http://doi.org/10.1016/j.pmatsci.2015.08.002 (2016).

41 Gupta, P., Elkins, C., Long, T. E. & Wilkes, G. L. Electrospinning of linear homopolymers of poly(methyl methacrylate): exploring relationships between fiber formation, viscosity, molecular weight and concentration in a good solvent. *Polymer* **46**, 4799-4810, doi:http://dx.doi.org/10.1016/j.polymer.2005.04.021 (2005).

42 Sochalski-Kolbus, L. M. *et al.* Solvothermal Synthesis and Surface Chemistry To Control the Size and Morphology of Nanoquartz. *Crystal Growth & Design* **15**, 5327-5331, doi:10.1021/acs.cgd.5b00882 (2015).

43 Demazeau, G. Solvothermal processes: new trends in materials chemistry. *Journal of Physics: Conference Series* **121**, 082003 (2008).

44 Polcari, D., Dauphin-Ducharme, P. & Mauzeroll, J. Scanning Electrochemical Microscopy: A Comprehensive Review of Experimental Parameters from 1989 to 2015. *Chemical Reviews* **116**, 13234-13278, doi:10.1021/acs.chemrev.6b00067 (2016).

45 Ramachandramoorthy, R., Bernal, R. & Espinosa, H. D. Pushing the Envelope of In Situ Transmission Electron Microscopy. *ACS Nano* **9**, 4675-4685, doi:10.1021/acsnano.5b01391 (2015).

46 Bunaciu, A. A., Udriştioiu, E. g. & Aboul-Enein, H. Y. X-Ray Diffraction: Instrumentation and Applications. *Critical Reviews in Analytical Chemistry* **45**, 289-299, doi:10.1080/10408347.2014.949616 (2015).

47 Sarma, D. D., Santra, P. K., Mukherjee, S. & Nag, A. X-ray Photoelectron Spectroscopy: A Unique Tool To Determine the Internal Heterostructure of Nanoparticles. *Chemistry of Materials* **25**, 1222-1232, doi:10.1021/cm303567d (2013).

48 Coats, A. W. & Redfern, J. P. Thermogravimetric analysis. A review. *Analyst* **88**, 906-924, doi:10.1039/AN9638800906 (1963).

49 Dutcher, C. S., Ge, X., Wexler, A. S. & Clegg, S. L. Statistical Mechanics of Multilayer Sorption: Extension of the Brunauer–Emmett–Teller (BET) and

Guggenheim–Anderson–de Boer (GAB) Adsorption Isotherms. *The Journal of Physical Chemistry C* **115**, 16474-16487, doi:10.1021/jp203879d (2011).

50 Bumbrah, G. S. & Sharma, R. M. Raman spectroscopy – Basic principle, instrumentation and selected applications for the characterization of drugs of abuse. *Egyptian Journal of Forensic Sciences* **6**, 209-215, doi:http://doi.org/10.1016/j.ejfs.2015.06.001 (2016).

51 Aristov, N. & Habekost, A. Cyclic Voltammetry - A Versatile Electrochemical Method Investigating Electron Transfer Processes. *World Journal of Chemical Education* **3**, 115-119, doi:10.12691/wjce-3-5-2 (2015).

52 Bard, A. & Faulkner, L. *Electrochemical Methods: Fundamentals and Applications*. (John Wiley & Sons, Inc, 2001).

53 Abureden, S. *et al.* Modified chalcogens with a tuned nano-architecture for high energy density and long life hybrid super capacitors. *Journal of Materials Chemistry A*, doi:10.1039/C7TA00897J (2017).

54 Dawson, K., Baudequin, M. & O'Riordan, A. Single on-chip gold nanowires for electrochemical biosensing of glucose. *Analyst* **136**, 4507-4513, doi:10.1039/C1AN15279C (2011).

55 Sun, X., Radovanovic, P. V. & Cui, B. Advances in spinel Li4 Ti5 O12 anode materials for lithium-ion batteries. *New Journal of Chemistry* **39**, 38-63, doi:10.1039/c4nj01390e (2014).

56 Zhao, B., Ran, R., Liu, M. & Shao, Z. A comprehensive review of Li4Ti5O12-based electrodes for lithium-ion batteries: The latest advancements and future perspectives. *Materials Science and Engineering: R: Reports* **98**, 1-71, doi:http://dx.doi.org/10.1016/j.mser.2015.10.001 (2015).

57 Jiang, Y.-M., Wang, K.-X., Zhang, H.-J., Wang, J.-F. & Chen, J.-S. Hierarchical Li4Ti5O12/TiO2 composite tubes with regular structural imperfection for lithium ion storage. *Scientific Reports* **3**, 3490, doi:10.1038/srep03490 http://www.nature.com/articles/srep03490#supplementary-information (2013).

58 Yi, T.-F. *et al.* Recent development and application of Li4Ti5O12 as anode material of lithium ion battery. *Journal of Physics and Chemistry of Solids* **71**, 1236-1242, doi:http://dx.doi.org/10.1016/j.jpcs.2010.05.001 (2010).

59 Hassan, F. M. *et al.* Pyrrolic-structure enriched nitrogen doped graphene for highly efficient next generation supercapacitors. *Journal of Materials Chemistry A* **1**, 2904-2912 (2013).

60 Zhang, B., Huang, Z.-D., Oh, S. W. & Kim, J.-K. Improved rate capability of carbon coated Li3.9Sn0.1Ti5O12 porous electrodes for Li-ion batteries. *Journal of Power Sources* **196**, 10692-10697, doi:10.1016/j.jpowsour.2011.08.114 (2011).

61 Li, X., Qu, M., Huai, Y. & Yu, Z. Preparation and electrochemical performance of Li4Ti5O12/carbon/carbon nano-tubes for lithium ion battery. *Electrochimica Acta* **55**, 2978-2982, doi:http://dx.doi.org/10.1016/j.electacta.2010.01.015 (2010).

62 Wu, H. *et al.* Sr-doped Li4Ti5O12 as the anode material for lithium-ion batteries. *Solid State Ionics* **232**, 13-18, doi:http://dx.doi.org/10.1016/j.ssi.2012.10.027 (2013).

63 Zhao, H. *et al.* Structural and electrochemical characteristics of Li4−xAlxTi5O12 as anode material for lithium-ion batteries. *Electrochimica Acta* **53**, 7079-7083, doi:http://dx.doi.org/10.1016/j.electacta.2008.05.038 (2008).

64 Huang, S., Wen, Z., Zhu, X. & Lin, Z. Effects of dopant on the electrochemical performance of Li4Ti5O12 as electrode material for lithium ion batteries. *Journal of Power Sources* **165**, 408-412, doi:10.1016/j.jpowsour.2006.12.010.

65 Sun, Y. K., Jung, D. J., Lee, Y. S. & Nahm, K. S. Synthesis and electrochemical characterization of spinel Li[Li(1−x)/3CrxTi(5−2x)/3]O4 anode materials. *Journal of Power Sources* **125**, 242-245, doi:http://dx.doi.org/10.1016/j.jpowsour.2003.08.013 (2004).

66 Song, H. *et al.* Anomalous decrease in structural disorder due to charge redistribution in Cr-doped Li4Ti5O12 negative-electrode materials for high-rate Li-ion batteries. *Energy & Environmental Science* **5**, 9903-9913, doi:10.1039/C2EE22734G (2012).

67 Kim, J.-G. *et al.* Zr4+ Doping in Li4Ti5O12 Anode for Lithium-Ion Batteries: Open Li+ Diffusion Paths through Structural Imperfection. *ChemSusChem* **7**, 1451-1457, doi:10.1002/cssc.201301393 (2014).

68 Hao, Y.-J., Lai, Q.-Y., Lu, J.-Z. & Ji, X.-Y. Effects of dopant on the electrochemical properties of Li4Ti5O12 anode materials. *Ionics* **13**, 369-373, doi:10.1007/s11581-007-0111-1 (2007).

69 Kim, J., Kim, S.-W., Gwon, H., Yoon, W.-S. & Kang, K. Comparative study of Li(Li1/3Ti5/3)O4 and Li(Ni1/2−xLi2x/3Tix/3)Ti3/2O4 (x = 1/3) anodes for Li rechargeable batteries. *Electrochimica Acta* **54**, 5914-5918, doi:http://dx.doi.org/10.1016/j.electacta.2009.05.058 (2009).

70 Lin, C., Lai, M. O., Lu, L., Zhou, H. & Xin, Y. Structure and high rate performance of Ni2+ doped Li4Ti5O12 for lithium ion battery. *Journal of Power Sources* **244**, 272-279, doi:10.1016/j.jpowsour.2013.01.056 (2013).

71 Long, W. *et al.* Electrochemical properties of Li4Ti5−2x Ni x Mn x O12 compounds synthesized by sol–gel process. *Materials Chemistry and Physics* **131**, 431-435, doi:10.1016/j.matchemphys.2011.09.071 (2011).

72 Wu, F., Li, X., Wang, Z. & Guo, H. Synthesis of chromium-doped lithium titanate microspheres as high-performance anode material for lithium ion batteries. *Ceramics International* **40**, 13195-13204, doi:http://dx.doi.org/10.1016/j.ceramint.2014.05.025 (2014).

73 Wolfenstine, J. & Allen, J. L. Electrical conductivity and charge compensation in Ta doped Li4Ti5O12. *J. Power Sources* **180**, 582-585, doi:DOI 10.1016/j.jpowsour.2008.02.019 (2008).

74 Cheng, L. *et al.* General synthesis of carbon-coated nanostructure Li4Ti5O12 as a high rate electrode material for Li-ion intercalation. *Journal of Materials Chemistry* **20**, 595-602, doi:10.1039/b914604k (2010).

75 Jo, M. R., Jung, Y. S. & Kang, Y.-M. Tailored Li4Ti5O12 nanofibers with outstanding kinetics for lithium rechargeable batteries. *Nanoscale* **4**, 6870-6875, doi:10.1039/c2nr31675g (2012).

76 Aravindan, V. *et al.* Electrospun nanofibers: A prospective electro-active material for constructing high performance Li-ion batteries. *Chemical Communications* **51**, 2225-2234, doi:10.1039/C4CC07824A (2015).

77 Li, H. *et al.* Ultralong SrLi2Ti6O14 nanowires composed of single-crystalline nanoparticles: Promising candidates for high-power lithium ions batteries. *Nano Energy* **13**, 18-27, doi:http://dx.doi.org/10.1016/j.nanoen.2015.02.002 (2015).

78 Jung, J.-W., Lee, C.-L., Yu, S. & Kim, I.-D. Electrospun nanofibers as a platform for advanced secondary batteries: a comprehensive review. *Journal of Materials Chemistry A* **4**, 703-750, doi:10.1039/C5TA06844D (2016).

79 Angammana, C. J. & Jayaram, S. H. Analysis of the Effects of Solution Conductivity on Electrospinning Process and Fiber Morphology. *IEEE Transactions on Industry Applications* **47**, 1109-1117, doi:10.1109/TIA.2011.2127431 (2011).

80 Haider, A., Haider, S. & Kang, I.-K. A comprehensive review summarizing the effect of electrospinning parameters and potential applications of nanofibers in

biomedical and biotechnology. *Arabian Journal of Chemistry*, doi:http://dx.doi.org/10.1016/j.arabjc.2015.11.015.

81 Tran, T. D., Feikert, J. H., Song, X. & Kinoshita, K. Commercial Carbonaceous Materials as Lithium Intercalation Anodes. *Journal of The Electrochemical Society* **142**, 3297-3302, doi:10.1149/1.2049977 (1995).

82 Shen, Y., Søndergaard, M., Christensen, M., Birgisson, S. & Iversen, B. B. Solid State Formation Mechanism of Li4Ti5O12 from an Anatase TiO2 Source. *Chem. Mater.* **26**, 3679-3686, doi:10.1021/cm500934z (2014).

83 Zaghib, K., Simoneau, M., Armand, M. & Gauthier, M. Electrochemical study of Li4Ti5O12 as negative electrode for Li-ion polymer rechargeable batteries. *Journal of Power Sources* **81–82**, 300-305, doi:http://dx.doi.org/10.1016/S0378-7753(99)00209-8 (1999).

84 Jhan, Y.-R. & Duh, J.-G. Electrochemical performance and low discharge cut-off voltage behavior of ruthenium doped Li4Ti5O12 with improved energy density. *Electrochimica Acta* **63**, 9-15, doi:http://dx.doi.org/10.1016/j.electacta.2011.12.014 (2012).

85 Capsoni, D. *et al.* Cations Distribution and Valence States in Mn-Substituted Li4Ti5O12 Structure. *Chemistry of Materials* **20**, 4291-4298, doi:10.1021/cm703650c (2008).

86 Han, D.-D., Pan, G.-L., Liu, S. & Gao, X.-P. PO43- doped Li4Ti5O12 hollow microspheres as an anode material for lithium-ion batteries. *RSC Advances* **5**, 92354-92360, doi:10.1039/C5RA17144J (2015).

87 Li, F., Zeng, M., Li, J., Tong, X. & Xu, H. Sb doped Li4Ti5O12 hollow spheres with enhanced lithium storage capability. *RSC Advances* **6**, 26902-26907, doi:10.1039/C6RA01831A (2016).

88 Huang, S., Wen, Z., Gu, Z. & Zhu, X. Preparation and cycling performance of Al^3^+and F^- co-substituted compounds Li4AlxTi5-xFyO12-y. *Electrochimica Acta* **50**, 4057-4062, doi:10.1016/j.electacta.2004.12.036.

89 Ganapathy, S., van Eck, E. R. H., Kentgens, A. P. M., Mulder, F. M. & Wagemaker, M. Equilibrium Lithium-Ion Transport Between Nanocrystalline Lithium-Inserted Anatase TiO2 and the Electrolyte. *Chemistry – A European Journal* **17**, 14811-14816, doi:10.1002/chem.201101431.

90 Yu, Z. *et al.* High rate capability and long-term cyclability of Li4Ti4.9V0.1O12 as anode material in lithium ion battery. *Electrochimica Acta* **56**, 8611-8617, doi:http://dx.doi.org/10.1016/j.electacta.2011.07.051 (2011).

91 Jamnik, J. & Maier, J. Treatment of the impedance of mixed conductors. Equivalent circuit model and explicit approximate solutions. *Journal of the Electrochemical Society* **146**, 4183-4188, doi:10.1149/1.1392611 (1999).

92 Chen, T. & Dai, L. Flexible supercapacitors based on carbon nanomaterials. *Journal of Materials Chemistry A* **2**, 10756-10775, doi:10.1039/C4TA00567H (2014).

93 Roldán, S. *et al.* An approach to classification and capacitance expressions in electrochemical capacitors technology. *Physical Chemistry Chemical Physics* **17**, 1084-1092, doi:10.1039/c4cp05124f (2014).

94 Sun, X. *et al.* In situ unravelling structural modulation across the charge-density-wave transition in vanadium disulfide. *Physical Chemistry Chemical Physics* **17**, 13333-13339, doi:10.1039/C5CP01326G (2015).

95 Chan, C. K. *et al.* High-performance lithium battery anodes using silicon nanowires. *Nat Nano* **3**, 31-35, doi:http://www.nature.com/nnano/journal/v3/n1/suppinfo/nnano.2007.411_S1.html (2008).

96 Mai, L., Dong, Y., Xu, L. & Han, C. Single Nanowire Electrochemical Devices. *Nano Letters* **10**, 4273-4278, doi:10.1021/nl102845r (2010).

97 Tarascon, J. M. & Armand, M. Issues and challenges facing rechargeable lithium batteries. *Nature* **414**, 359-367 (2001).

98 Armand, M. & Tarascon, J. M. Building better batteries. *Nature* **451**, 652-657 (2008).

99 Dong, L. *et al.* Flexible electrodes and supercapacitors for wearable energy storage: a review by category. *J. Mater. Chem. A* **4**, 4659-4685, doi:10.1039/c5ta10582j (2016).

100 Ren, G., Ma, G. & Cong, N. Review of electrical energy storage system for vehicular applications. *Renewable and Sustainable Energy Reviews* **41**, 225-236, doi:http://dx.doi.org/10.1016/j.rser.2014.08.003 (2015).

101 Lai, C.-H., Lu, M.-Y. & Chen, L.-J. Metal sulfide nanostructures: synthesis, properties and applications in energy conversion and storage. *J. Mater. Chem.* **22**, 19-30, doi:10.1039/c1jm13879k (2012).

102 Chen, J.-C., Hsu, C.-T. & Hu, C.-C. Superior capacitive performances of binary nickel–cobalt hydroxide nanonetwork prepared by cathodic deposition. *J. Power Sources* **253**, 205-213, doi:http://dx.doi.org/10.1016/j.jpowsour.2013.12.073 (2014).

103 Li, X., Li, Q., Wu, Y., Rui, M. & Zeng, H. Two-Dimensional, Porous Nickel–Cobalt Sulfide for High-Performance Asymmetric Supercapacitors. *ACS Applied Materials & Interfaces* **7**, 19316-19323, doi:10.1021/acsami.5b05400 (2015).

104 Shen, L. *et al.* NiCo2S4 Nanosheets Grown on Nitrogen-Doped Carbon Foams as an Advanced Electrode for Supercapacitors. *Advanced Energy Materials* **5**, 1400977-n/a, doi:10.1002/aenm.201400977 (2015).

105 Xiao, J., Wan, L., Yang, S., Xiao, F. & Wang, S. Design Hierarchical Electrodes with Highly Conductive NiCo2S4 Nanotube Arrays Grown on Carbon Fiber Paper for High-Performance Pseudocapacitors. *Nano Lett.* **14**, 831-838, doi:10.1021/nl404199v (2014).

106 Chen, H. *et al.* Highly conductive NiCo2S4 urchin-like nanostructures for high-rate pseudocapacitors. *Nanoscale* **5**, 8879-8883, doi:10.1039/C3NR02958A (2013).

107 Masikhwa, T. M. *et al.* Asymmetric supercapacitor based on VS2 nanosheets and activated carbon materials. *RSC Advances* **6**, 38990-39000, doi:10.1039/C5RA27155J (2016).

108 Yang, J. *et al.* Electroactive edge site-enriched nickel-cobalt sulfide into graphene frameworks for high-performance asymmetric supercapacitors. *Energy & Environmental Science* **9**, 1299-1307, doi:10.1039/C5EE03633J (2016).

109 Shen, J. *et al.* Controlled synthesis and comparison of NiCo2S4/graphene/2D TMD ternary nanocomposites for high-performance supercapacitors. *Chem Commun* **52**, 9251-9254, doi:10.1039/c6cc03699f (2016).

110 Karthikeyan, G. & Das, C. K. Transition Metal Salt Doping on Polypyrrole/MWCNT Composites for Supercapacitor Applications. *Macromol. Symp.* **315**, 98-105, doi:10.1002/masy.201250512 (2012).

111 Hu, Y., Liu, H., Ke, Q. & Wang, J. Effects of nitrogen doping on supercapacitor performance of a mesoporous carbon electrode produced by a hydrothermal soft-templating process. *J. Mater. Chem. A* **2**, 11753-11758, doi:10.1039/c4ta01269k (2014).

112 Shao, G., Yao, Y., Zhang, S. & He, P. Supercapacitor characteristic of La-doped Ni(OH)2 prepared by electrode-position. *Rare Metals* **28**, 132-136, doi:10.1007/s12598-009-0026-2 (2009).

113 Qu, Q. T. *et al.* V2O5·0.6H2O nanoribbons as cathode material for asymmetric supercapacitor in K2SO4 solution. *Electrochemistry Communications* **11**, 1325-1328, doi:http://dx.doi.org/10.1016/j.elecom.2009.05.003 (2009).

114 Wang, N., Zhang, Y., Hu, T., Zhao, Y. & Meng, C. Facile hydrothermal synthesis of ultrahigh-aspect-ratio V2O5 nanowires for high-performance supercapacitors. *Current Applied Physics* **15**, 493-498, doi:http://dx.doi.org/10.1016/j.cap.2015.01.026 (2015).

115 Fang, W.-C. Synthesis and Electrochemical Characterization of Vanadium Oxide/Carbon Nanotube Composites for Supercapacitors. *The Journal of Physical Chemistry C* **112**, 11552-11555, doi:10.1021/jp8011602 (2008).

116 Higgins, D. C. *et al.* Shape-controlled octahedral cobalt disulfide nanoparticles supported on nitrogen and sulfur-doped graphene/carbon nanotube composites for oxygen reduction in acidic electrolyte. *Journal of Materials Chemistry A* **3**, 6340-6350, doi:10.1039/C4TA06667G (2015).

117 Liang, Y., Li, Y., Wang, H. & Dai, H. Strongly Coupled Inorganic/Nanocarbon Hybrid Materials for Advanced Electrocatalysis. *Journal of the American Chemical Society* **135**, 2013-2036, doi:10.1021/ja3089923 (2013).

118 Madarász, J. & Pokol, G. Comparativeevolved gas analyses on thermal degradation of thiourea by coupled TG-FTIRand TG/DTA-MS instruments. *Journal of Thermal Analysis and Calorimetry* **88**, 329-336, doi:10.1007/s10973-006-8058-4 (2007).

119 Pei, S. & Cheng, H.-M. The reduction of graphene oxide. *Carbon* **50**, 3210-3228, doi:http://dx.doi.org/10.1016/j.carbon.2011.11.010 (2012).

120 Liu, Y., Li, Y., Yang, Y., Wen, Y. & Wang, M. Reduction of Graphene Oxide by Thiourea. *Journal of Nanoscience and Nanotechnology* **11**, 10082-10086, doi:10.1166/jnn.2011.4985 (2011).

121 Dubin, S. *et al.* A One-Step, Solvothermal Reduction Method for Producing Reduced Graphene Oxide Dispersions in Organic Solvents. *ACS Nano* **4**, 3845-3852, doi:10.1021/nn100511a (2010).

122 Peng, S. *et al.* In situ growth of NiCo2S4 nanosheets on graphene for high-performance supercapacitors. *Chemical Communications* **49**, 10178-10180, doi:10.1039/C3CC46034G (2013).

123 Popović, J. *et al.* Partial inverse spinel structure of manganese-doped gahnite: XRD and EPR spectroscopy studies. *Journal of Alloys and Compounds* **509**, 8487-8492, doi:http://dx.doi.org/10.1016/j.jallcom.2011.06.006 (2011).

124 Arif Sher Shah, M. S. *et al.* Single-step solvothermal synthesis of mesoporous Ag-TiO2-reduced graphene oxide ternary composites with enhanced photocatalytic activity. *Nanoscale* **5**, 5093-5101, doi:10.1039/C3NR00579H (2013).

125 El-Kady, M. F., Shao, Y. & Kaner, R. B. Graphene for batteries, supercapacitors and beyond. *Nature Reviews Materials* **1**, 16033, doi:10.1038/natrevmats.2016.33 (2016).

126 Raccichini, R., Varzi, A., Passerini, S. & Scrosati, B. The role of graphene for electrochemical energy storage. *Nat Mater* **14**, 271-279, doi:10.1038/nmat4170 (2015).

127 He, G. *et al.* S, N-Co-Doped Graphene-Nickel Cobalt Sulfide Aerogel: Improved Energy Storage and Electrocatalytic Performance. *Advanced Science*, 1600214-n/a, doi:10.1002/advs.201600214 (2016).

128 Liu, Q. *et al.* One-pot synthesis of nitrogen and sulfur co-doped graphene supported MoS2 as high performance anode materials for lithium-ion batteries. *Electrochimica Acta* **177**, 298-303, doi:http://dx.doi.org/10.1016/j.electacta.2015.01.193 (2015).

129 Nair, V. S. *et al.* Crystalline Li3V6O16 rods as high-capacity anode materials for aqueous rechargeable lithium batteries (ARLB). *RSC Advances* **4**, 28601-28605, doi:10.1039/C4RA02804J (2014).

130 Warwick, M. E. A., Roberts, A. J., Slade, R. C. T. & Binions, R. Electric field assisted chemical vapour deposition - a new method for the preparation of highly porous supercapacitor electrodes. *Journal of Materials Chemistry A* **2**, 6115-6120, doi:10.1039/C3TA14185C (2014).

131 Nguyen, H. T. T., Jung, D., Park, C.-Y. & Kang, D. J. Synthesis of single-crystalline sodium vanadate nanowires based on chemical solution deposition method. *Materials Chemistry and Physics* **165**, 19-24, doi:http://dx.doi.org/10.1016/j.matchemphys.2015.05.053 (2015).

132 Ding, Y.-L. *et al.* A Lamellar Hybrid Assembled from Metal Disulfide Nanowall Arrays Anchored on a Carbon Layer: In Situ Hybridization and Improved Sodium Storage. *Advanced Materials* **28**, 7774-7782, doi:10.1002/adma.201602009 (2016).

133 Tao, J. G. *et al.* Origin of XPS binding energy shifts in Ni clusters and atoms on rutile TiO2 surfaces. *Surface Science* **602**, 2769-2773, doi:http://dx.doi.org/10.1016/j.susc.2008.06.034 (2008).

134 Sadanandam, G., Lalitha, K., Kumari, V. D., Shankar, M. V. & Subrahmanyam, M. Cobalt doped TiO2: A stable and efficient photocatalyst for continuous hydrogen production from glycerol: Water mixtures under solar light irradiation. *International Journal of Hydrogen Energy* **38**, 9655-9664, doi:http://dx.doi.org/10.1016/j.ijhydene.2013.05.116 (2013).

135 Oswald, S. Binding energy referencing for XPS in alkali metal-based battery materials research (I): Basic model investigations. *Applied Surface Science* **351**, 492-503, doi:http://dx.doi.org/10.1016/j.apsusc.2015.05.029 (2015).

136 Liu, L. *et al.* Influence of vanadium doping on the supercapacitance performance of hexagonal birnessite. *Journal of Power Sources* **277**, 26-35, doi:http://dx.doi.org/10.1016/j.jpowsour.2014.12.004 (2015).

137 Huang, L., Li, Y., Zhou, Q., Yuan, W. & Shi, G. Graphene oxide membranes with tunable semipermeability in organic solvents. *Advanced Materials* **27**, 3797-3802 (2015).

138 Magda, G. Z. *et al.* Exfoliation of large-area transition metal chalcogenide single layers. *Scientific Reports* **5**, 14714, doi:10.1038/srep14714 (2015).

139 Peyrot, D. & Silly, F. On-Surface Synthesis of Two-Dimensional Covalent Organic Structures versus Halogen-Bonded Self-Assembly: Competing Formation of Organic Nanoarchitectures. *ACS Nano* **10**, 5490-5498, doi:10.1021/acsnano.6b01938 (2016).

140 Chen, W., Xia, C. & Alshareef, H. N. One-Step Electrodeposited Nickel Cobalt Sulfide Nanosheet Arrays for High-Performance Asymmetric Supercapacitors. *ACS Nano* **8**, 9531-9541, doi:10.1021/nn503814y (2014).

141 Pu, J. *et al.* Preparation and Electrochemical Characterization of Hollow Hexagonal NiCo2S4 Nanoplates as Pseudocapacitor Materials. *ACS Sustainable Chemistry & Engineering* **2**, 809-815, doi:10.1021/sc400472z (2014).

142 Pu, J. *et al.* Direct Growth of NiCo2S4 Nanotube Arrays on Nickel Foam as High-Performance Binder-Free Electrodes for Supercapacitors. *ChemPlusChem* **79**, 577-583, doi:10.1002/cplu.201300431 (2014).

143 Li, G. & Xu, C. Hydrothermal synthesis of 3D Ni x Co1− x S2 particles/graphene composite hydrogels for high performance supercapacitors. *Carbon* **90**, 44-52, doi:10.1016/j.carbon.2015.03.066 (2015).

144 Abureden, S. A., Hassan, F. M., Yu, A. & Chen, Z. Reconciled Nanoarchitecture with Overlapped 2D Anatomy for High Energy Hybrid Supercapacitors. *Energy Technology*, n/a-n/a, doi:10.1002/ente.201700225.

145 Choi, N.-S. *et al.* Challenges Facing Lithium Batteries and Electrical Double-Layer Capacitors. *Angewandte Chemie International Edition* **51**, 9994-10024, doi:10.1002/anie.201201429 (2012).

146 Lukatskaya, M. R., Dunn, B. & Gogotsi, Y. Multidimensional materials and device architectures for future hybrid energy storage. *Nature Communications* **7**, 12647, doi:10.1038/ncomms12647 (2016).

147 Wang, H. *et al.* Advanced asymmetrical supercapacitors based on graphene hybrid materials. *Nano Research* **4**, 729-736, doi:10.1007/s12274-011-0129-6 (2011).

148 Shi, S. *et al.* Flexible asymmetric supercapacitors based on ultrathin two-dimensional nanosheets with outstanding electrochemical performance and aesthetic property. *Scientific Reports* **3**, 2598, doi:10.1038/srep02598 http://www.nature.com/articles/srep02598#supplementary-information (2013).

149 Liu, Y., Wang, R. & Yan, X. Synergistic Effect between Ultra-Small Nickel Hydroxide Nanoparticles and Reduced Graphene Oxide sheets for the Application in High-Performance Asymmetric Supercapacitor. *Scientific Reports* **5**, 11095, doi:10.1038/srep11095 http://www.nature.com/articles/srep11095#supplementary-information (2015).

150 Xia, H. *et al.* Facile Synthesis of Hematite Quantum-Dot/Functionalized Graphene-Sheet Composites as Advanced Anode Materials for Asymmetric Supercapacitors. *Advanced Functional Materials* **25**, 627-635, doi:10.1002/adfm.201403554 (2015).

151 Feng, J. *et al.* Metallic Few-Layered VS2 Ultrathin Nanosheets: High Two-Dimensional Conductivity for In-Plane Supercapacitors. *Journal of the American Chemical Society* **133**, 17832-17838, doi:10.1021/ja207176c (2011).

152 Therese, H. A. *et al.* VS2 Nanotubes Containing Organic-Amine Templates from the NT-VOx Precursors and Reversible Copper Intercalation in NT-VS2. *Angewandte Chemie International Edition* **44**, 262-265, doi:10.1002/anie.200461326 (2005).

153 Murphy, D. W., Cros, C., Di Salvo, F. J. & Waszczak, J. V. Preparation and properties of LixVS2 (0 .ltoreq. x .ltoreq. 1). *Inorganic Chemistry* **16**, 3027-3031, doi:10.1021/ic50178a008 (1977).

154 Beamson, G. B., D. High Resolution XPS of Organic Polymers: The Scienta ESCA300 Database (Beamson, G.; Briggs, D.). *Journal of Chemical Education* **70**, A25, doi:10.1021/ed070pA25.5 (1993).

155 Khalid, S., Cao, C., Wang, L. & Zhu, Y. Microwave Assisted Synthesis of Porous NiCo2O4 Microspheres: Application as High Performance Asymmetric and Symmetric Supercapacitors with Large Areal Capacitance. *Scientific Reports* **6**, 22699, doi:10.1038/srep22699

http://www.nature.com/articles/srep22699#supplementary-information (2016).

156 Sing, K. S. W. *et al.* in *Handbook of Heterogeneous Catalysis* (Wiley-VCH Verlag GmbH & Co. KGaA, 2008).

157 Feng, Y., Zhang, H., Fang, L., Li, W. & Wang, Y. Novel three-dimensional flower-like porous Al2O3 nanosheets anchoring hollow NiO nanoparticles for high-efficiency lithium ion batteries. *Journal of Materials Chemistry A* **4**, 11507-11515, doi:10.1039/C6TA04323B (2016).

158 Parveen, N. & Cho, M. H. Self-Assembled 3D Flower-Like Nickel Hydroxide Nanostructures and Their Supercapacitor Applications. *Scientific Reports* **6**, 27318, doi:10.1038/srep27318

http://www.nature.com/articles/srep27318#supplementary-information (2016).

159 Hassan, F. M. *et al.* Evidence of covalent synergy in silicon–sulfur–graphene yielding highly efficient and long-life lithium-ion batteries. *Nature Communications* **6**, 8597, doi:10.1038/ncomms9597

http://www.nature.com/articles/ncomms9597#supplementary-information (2015).

160 Seel, S. C., Hoyt, J. J., Webb, E. B. & Zimmerman, J. A. Modeling metallic island coalescence stress via adhesive contact between surfaces. *Physical Review B* **73**, 245402 (2006).

161 Ghanem, W. A., Bayyoumi, F. M. & Ateya, B. G. The high temperature corrosion of a low alloy steel in aqueous sodium chloride. *Corrosion Science* **38**, 1171-1186, doi:http://dx.doi.org/10.1016/0010-938X(96)00012-1 (1996).

162 Whelpdale, D. M. & List, R. The Coalescence process in raindrop growth. *Journal of Geophysical Research* **76**, 2836-2856, doi:10.1029/JC076i012p02836 (1971).

163 Dubrovskii, V. G. *Nucleation Theory and Growth of Nanostructures, NanoScience and Technology,*. 1-73 (Nucleation Theory and Growth of Nanostructures, 1 NanoScience and Technology,, 2014).

164 Steudel, R. Mechanism for the Formation of Elemental Sulfur from Aqueous Sulfide in Chemical and Microbiological Desulfurization Processes. *Industrial & Engineering Chemistry Research* **35**, 1417-1423, doi:10.1021/ie950558t (1996).

165 Ferreira, S. O. & Ferreira Jr., S. C. Volmer-Weber growth of CdTe on silicon: a one-dimension Monte Carlo model. *Brazilian Journal of Physics* **36**, 294-297 (2006).

166 Rajkumar, M., Hsu, C.-T., Wu, T.-H., Chen, M.-G. & Hu, C.-C. Advanced materials for aqueous supercapacitors in the asymmetric design. *Progress in Natural Science: Materials International* **25**, 527-544, doi:http://dx.doi.org/10.1016/j.pnsc.2015.11.012 (2015).

167 Krengel, M., Adelhelm, P., Klein, F. & Bensch, W. FeV2S4 as a high capacity electrode material for sodium-ion batteries. *Chemical Communications* **51**, 13500-13503, doi:10.1039/C5CC04022A (2015).

168 Kim, S. U., Perdue, B., Apblett, C. A. & Srinivasan, V. Understanding Performance Limitations to Enable High Performance Magnesium-Ion Batteries. *Journal of The Electrochemical Society* **163**, A1535-A1542, doi:10.1149/2.0321608jes (2016).

169 Liu, S. *et al.* Controllable sulfuration engineered NiO nanosheets with enhanced capacitance for high rate supercapacitors. *Journal of Materials Chemistry A* **5**, 4543-4549, doi:10.1039/C6TA11049E (2017).

170 Kim, B. C., Hong, J.-Y., Wallace, G. G. & Park, H. S. Recent Progress in Flexible Electrochemical Capacitors: Electrode Materials, Device Configuration, and

Functions. *Advanced Energy Materials* **5**, 1500959-n/a, doi:10.1002/aenm.201500959 (2015).

171 Li, Y., Tang, F., Wang, R., Wang, C. & Liu, J. Novel Dual-Ion Hybrid Supercapacitor Based on a NiCo2O4 Nanowire Cathode and MoO2–C Nanofilm Anode. *ACS Applied Materials & Interfaces* **8**, 30232-30238, doi:10.1021/acsami.6b10249 (2016).

172 Chen, K. & Xue, D. High Energy Density Hybrid Supercapacitor: In-Situ Functionalization of Vanadium-Based Colloidal Cathode. *ACS Applied Materials & Interfaces* **8**, 29522-29528, doi:10.1021/acsami.6b10638 (2016).

173 Portet, C., Yushin, G. & Gogotsi, Y. Effect of Carbon Particle Size on Electrochemical Performance of EDLC. *Journal of The Electrochemical Society* **155**, A531-A536, doi:10.1149/1.2918304 (2008).

174 Wagemaker, M., Borghols, W. J. H. & Mulder, F. M. Large Impact of Particle Size on Insertion Reactions. A Case for Anatase LixTiO2. *Journal of the American Chemical Society* **129**, 4323-4327, doi:10.1021/ja067733p (2007).

175 Kavan, L. *et al.* Li Insertion into Li4Ti5 O 12 (Spinel) : Charge Capability vs. Particle Size in Thin-Film Electrodes. *Journal of The Electrochemical Society* **150**, A1000-A1007, doi:10.1149/1.1581262 (2003).

176 Agarwal, S. R., Sundarrajan, S., Venkatesan, A. & Ramakrishna, S. One-Step Synthesis of Hollow Titanate (Sr/Ba) Ceramic Fibers for Detoxification of Nerve Agents. *Journal of Nanotechnology* **2012**, 7, doi:10.1155/2012/429021 (2012).

177 Long, W. *et al.* Electrochemical properties of Li4Ti5−2xNixMnxO12 compounds synthesized by sol–gel process. *Materials Chemistry and Physics* **131**, 431-435, doi:10.1016/j.matchemphys.2011.09.071 (2011).

178 Song, H. *et al.* Anomalous decrease in structural disorder due to charge redistribution in Cr-doped Li4Ti5O12 negative-electrode materials for high-rate Li-ion batteries. *Energy & Environmental Science* **5**, 9903, doi:10.1039/c2ee22734g (2012).

179 Zhang, Z. *et al.* Hydrothermal synthesis of Zn-doped Li4Ti5O12 with improved high rate properties for lithium ion batteries. *Ceramics International* **39**, 6139-6143, doi:10.1016/j.ceramint.2013.01.032 (2013).

180 Qiu, C., Yuan, Z., Liu, L., Ye, N. & Liu, J. Sol–gel preparation and electrochemical properties of La-doped Li4Ti5O12 anode material for lithium-ion battery. *Journal of Solid State Electrochemistry* **17**, 841-847, doi:10.1007/s10008-012-1930-1 (2012).

181 Huang, S., Wen, Z., Zhu, X. & Gu, Z. Preparation and electrochemical performance of Ag doped Li4Ti5O12. *Electrochemistry Communications* **6**, 1093-1097, doi:10.1016/j.elecom.2004.08.013 (2004).

182 Wan, H. *et al.* NiCo2S4 porous nanotubes synthesis via sacrificial templates: high-performance electrode materials of supercapacitors. *CrystEngComm* **15**, 7649-7651, doi:10.1039/C3CE41243A (2013).

Appendix A

Table A-1. Comparison of the electrochemical performance of Ni-LTONF$_{10}$ with recent reports in literature (capacities in mAh.g^{-1})

	Morphology	***Dopant***	***0.2 C***	***10 C***	***20 C***	***50 C***
This work	***Nanofibers***	***Ni***	***190***	***134.9***	***116***	***63***
Ref. [69]	*Nanoparticle*	*Ni*	*170*	*No Data*	*No Data*	*No Data*
Ref.[70]	*Nanoparticle*	*Ni*	*150@0.5 C*	*72 /5 C*	*No Data*	*No Data*
Ref.[177]	*Nanoparticle*	*Ni/Mn*	*172@0.5C*	*No Data*	*No Data*	*No Data*
Ref.[59]	*Nanofibers*	*Zr^{+4}*	*151/ 0.1 C*	*135*	*130*	*No Data*
Ref.[137]	*Nanowire*	*Sr*	*161.2*	*110*	*96.2*	*No Data*
Ref.[178]	*Nanoparticle*	*Cr*	*145/ 1 C*	*125*	*No Data*	*No Data*
Ref.7[90]	*Nano article*	*V*	*177/ 0.1 C*	*117 @ 5 C*	*No Data*	*No Data*
Ref.[179]	*Nano Sheets*	*Zn*	*182.4*	*122.4*	*No Data*	*No Data*
Ref.[180]	*Nanoparticle*	*Ni*	*167.2*	*150@ 5 C*	*No Data*	*No Data*
Ref.[181]	*Nanoparticle*	*Ag*	*192.9*	*163@ 4 C*	*No Data*	*No Data*

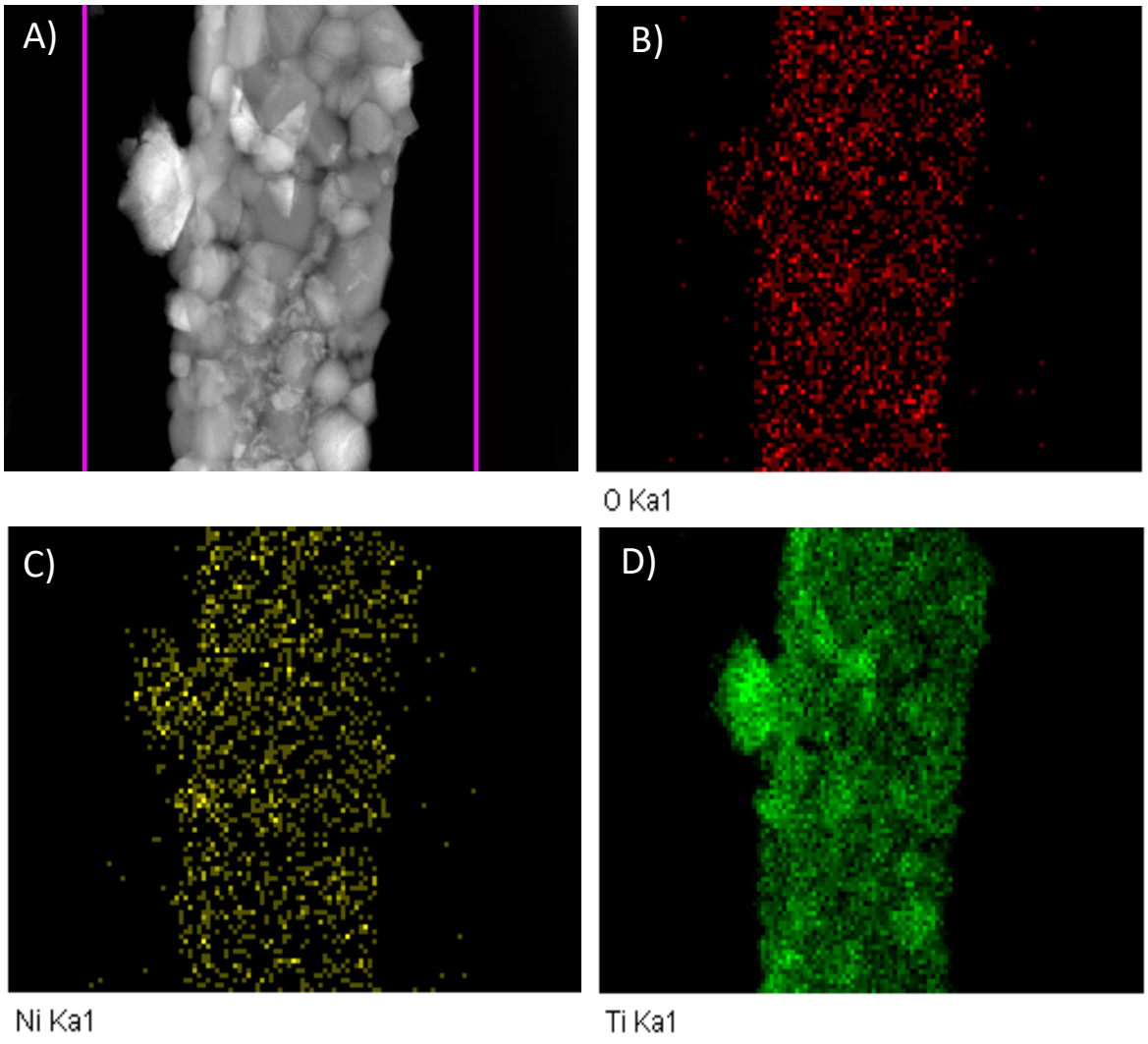

Figure A-1. TEM images of Ni-LTONF$_5$ showing the EDS mapping of oxygen, nickel and titanium in a homogenous distribution.

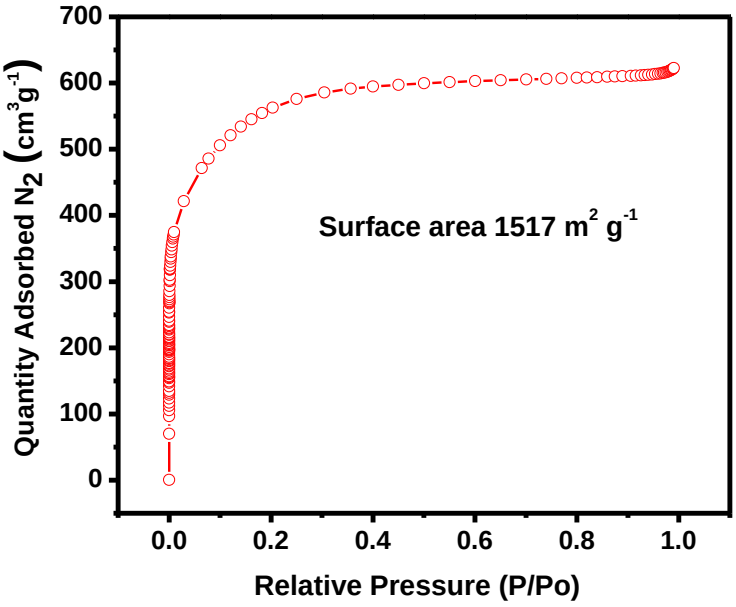

Figure A- 2. Nitrogen adsorption- desorption isotherm curve of AC electrode. The measured BET specific surface area is 1517 m^2 g^{-1}.

Appendix B

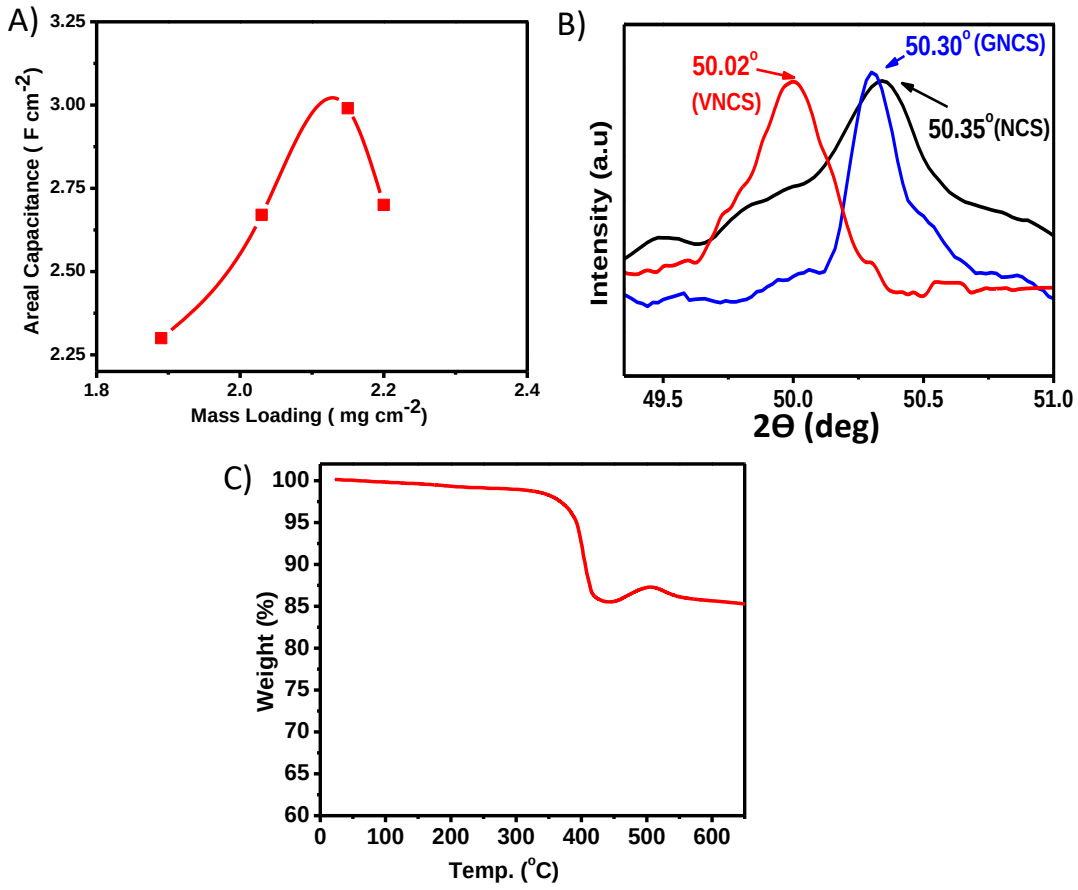

Figure B- 1 A) Areal capacitance variation with mass loading of VNCS, B) XRD shift of plane (511) of , VNCS, and C) TGA analysis of VNCS sample (reprinted from Ref.[53], with permission of the Royal Society of Chemistry)

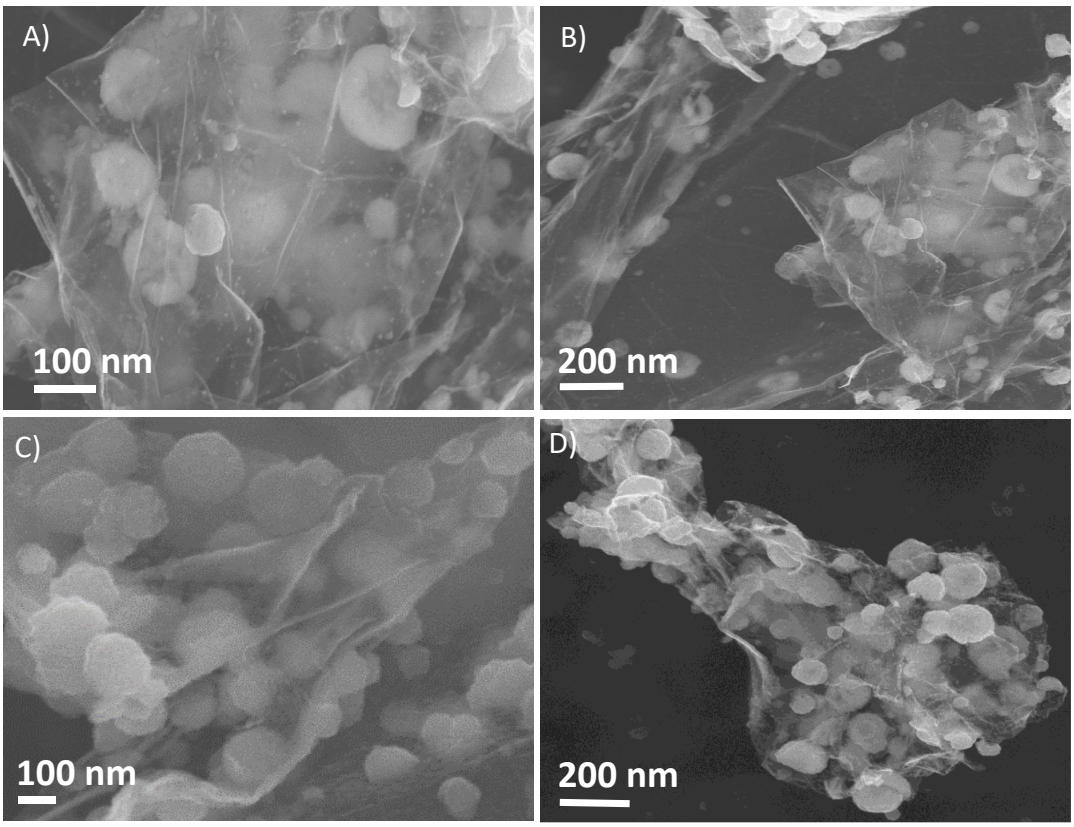

Figure B-2. SEM images showing the graphene wrapping of NCS in GNCS. (reprinted from Ref.[53], with permission of the Royal Society of Chemistry)

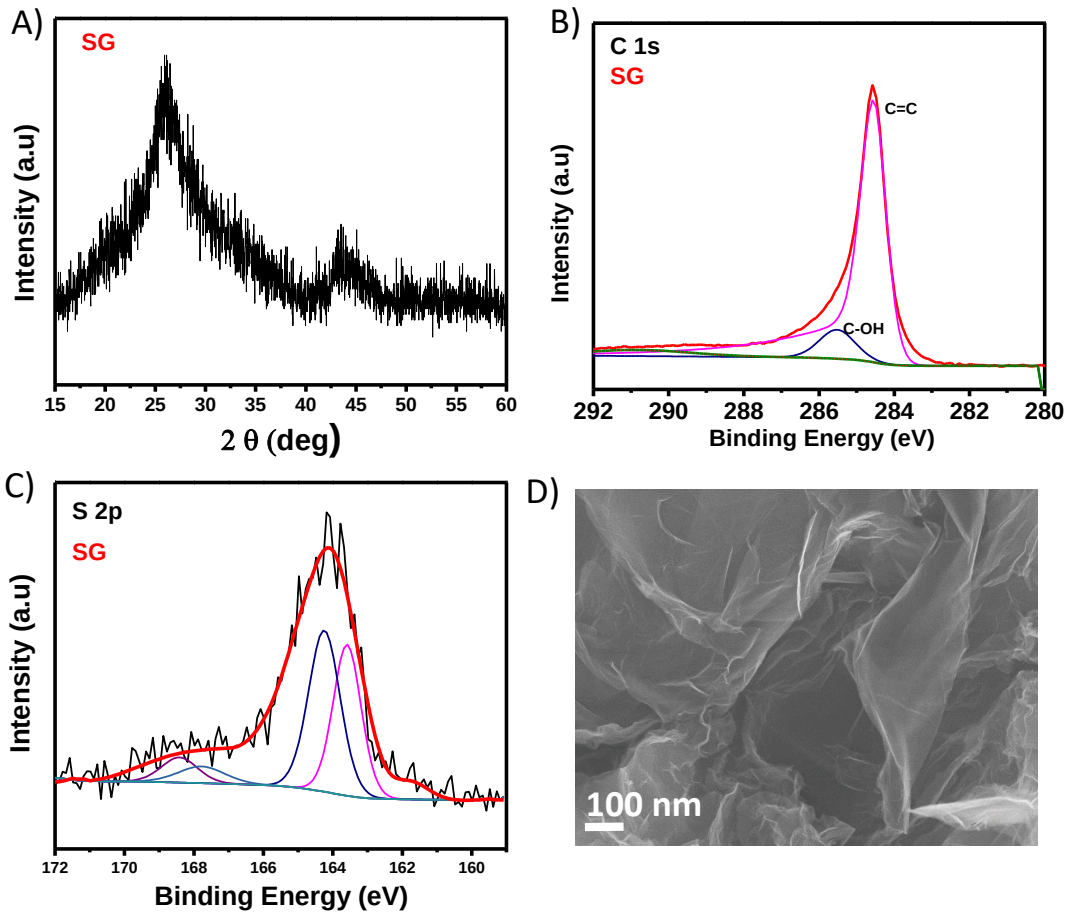

Figure B-3. A) XRD pattern of sulfur doped graphene (SG), B-C) XPS analysis of SG showing C 1s and S 2p respectively, and D) SEM image of SG nanosheets

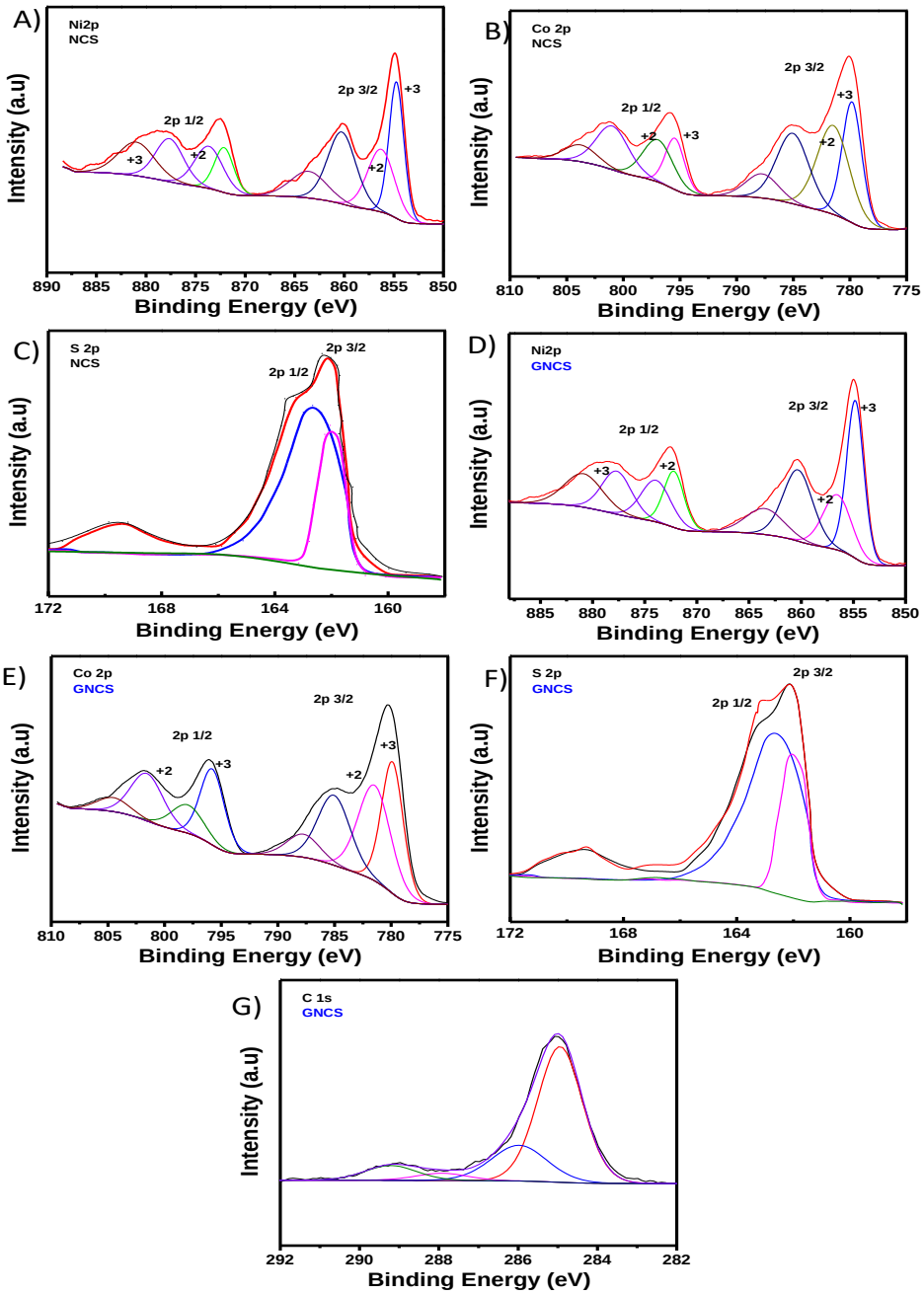

Figure B-4. XPS results, A-C) Ni 2p, Co 2p and S2p XPS spectra, respectively for NCS sample, and D-G) Ni 2p, Co 2p, S2p and C 1s XPS spectra, respectively for GNCS. (reprinted from Ref.[53], with permission of the Royal Society of Chemistry)

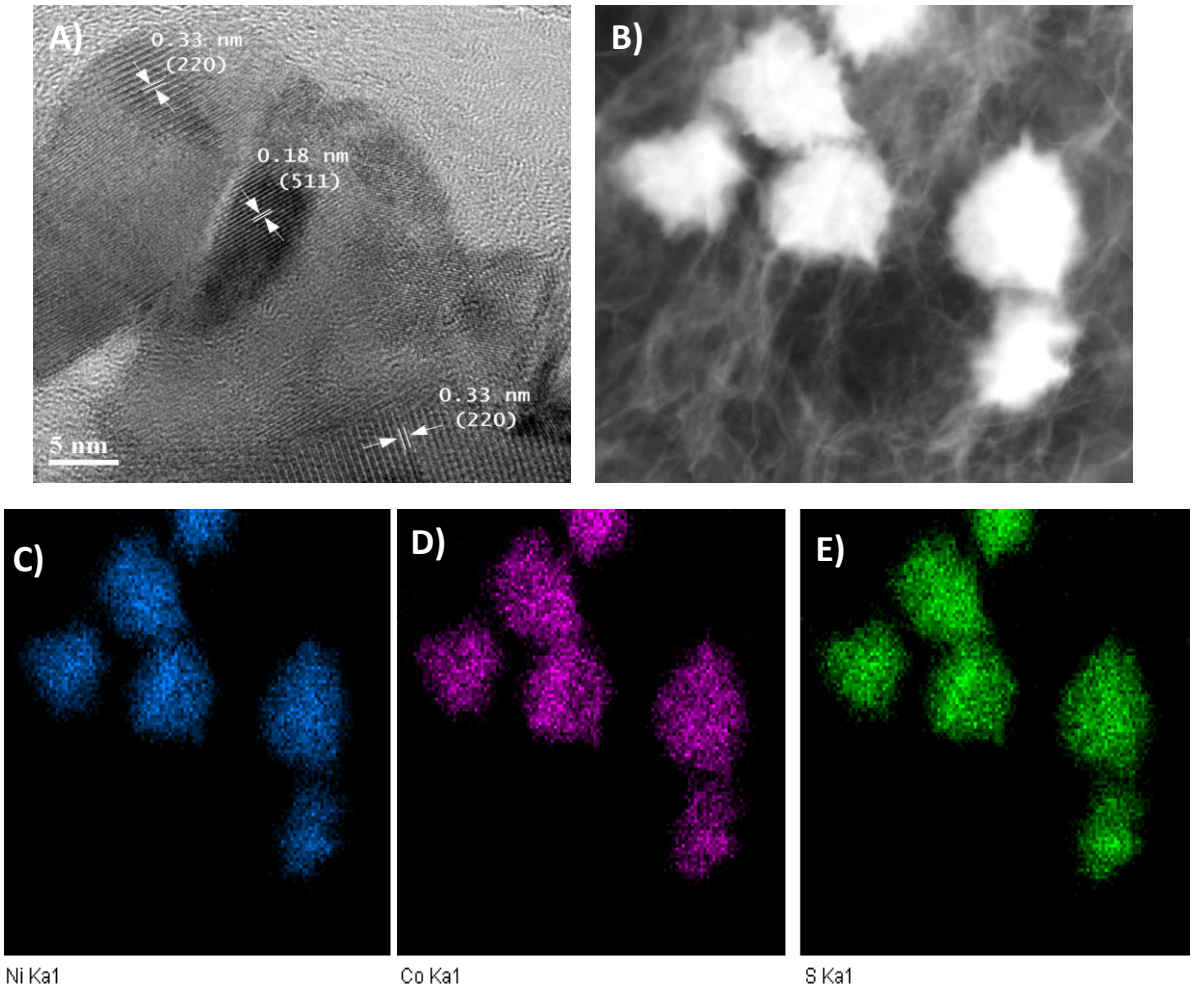

Figure B-5. A) HRTEM image of GNCS showing the fingerprint of different d-spacing, B) HRTEM showing the distribution of nanoparticles on the graphene sheets, and C-D) EDS mapping showing the nickel, cobalt and sulfur elements, respectively.

Table B-1. Detailed information about peaks of different elements in the three materials. (Reproduced from Ref.[53], with permission of the Royal Society of Chemistry)

Sample	Peak	BE (eV)	FWHM (eV)	Area (P) CPS (eV)	Atomic ratio (%)
NCS	Ni 2p	854.84	2.38	105871.61	14.002
	Co 2p	780.28	3.65	205211.37	28.432
	S 2p	163.2	2.08	68967.12	57.580
GNCS	Ni 2p	854.88	2.44	200901.38	9.528
	Co 2p	780.25	3.61	392198.45	19.542
	S 2p	162.18	2.04	128769.93	38.792
	C1S	284.88	1.35	52742.86	32.136
VNCS	Ni 2p	854.05	2.31	56626.06	11.106
	Co 2p	779.58	3.53	106986.08	21.978
	S 2p	162.05	2.01	36049.18	44.733
	C1S	284.62	1.37	13103.64	21.745
	V 2p	516.40	1.21	1945.99	0.443

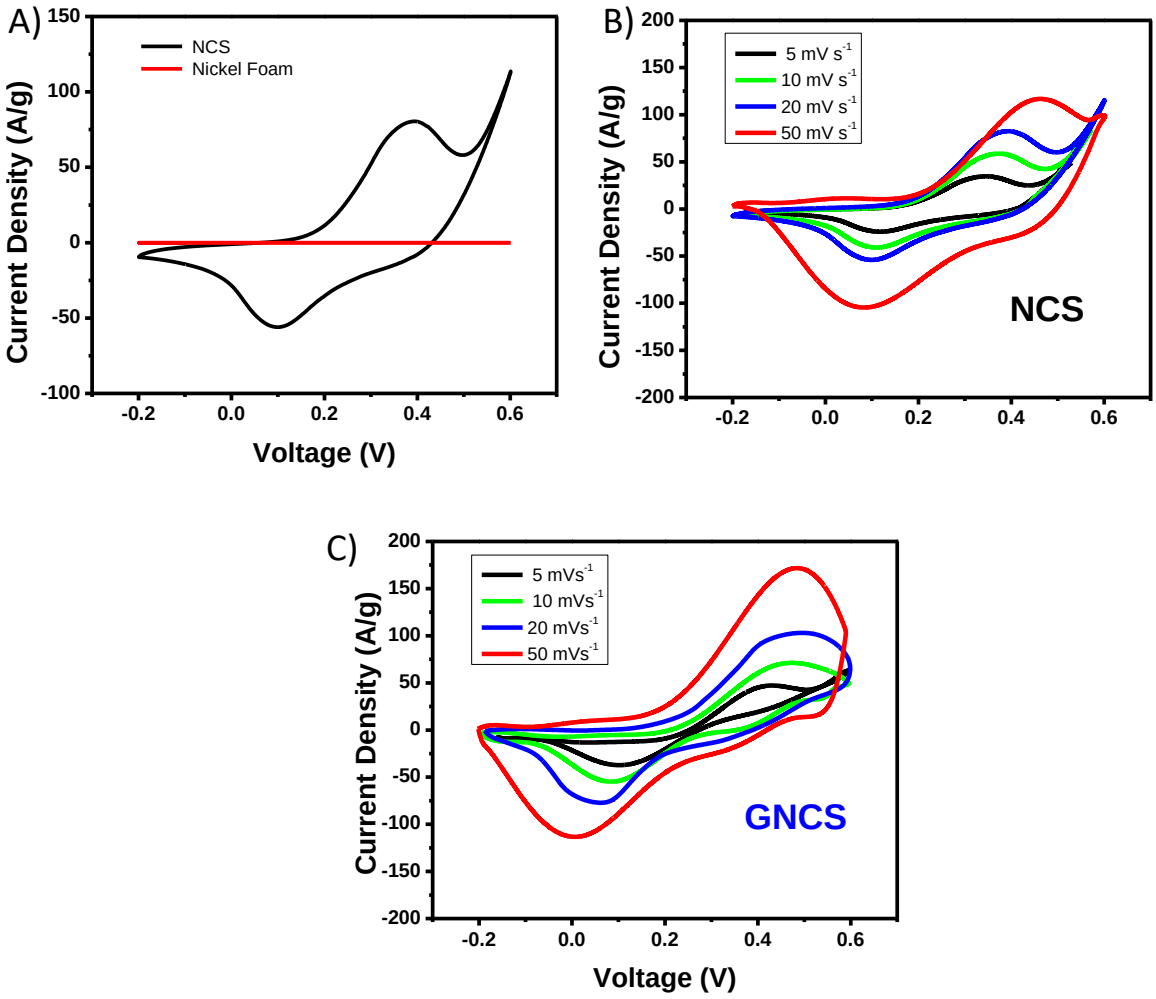

Figure B-6. A) CV test showing the negligible effect of nickel foam on the material performance, B) CV test at different scan rates of NCS, and C) CV test at different scan rates of GNCS. (reprinted from Ref.[53], with permission of the Royal Society of Chemistry)

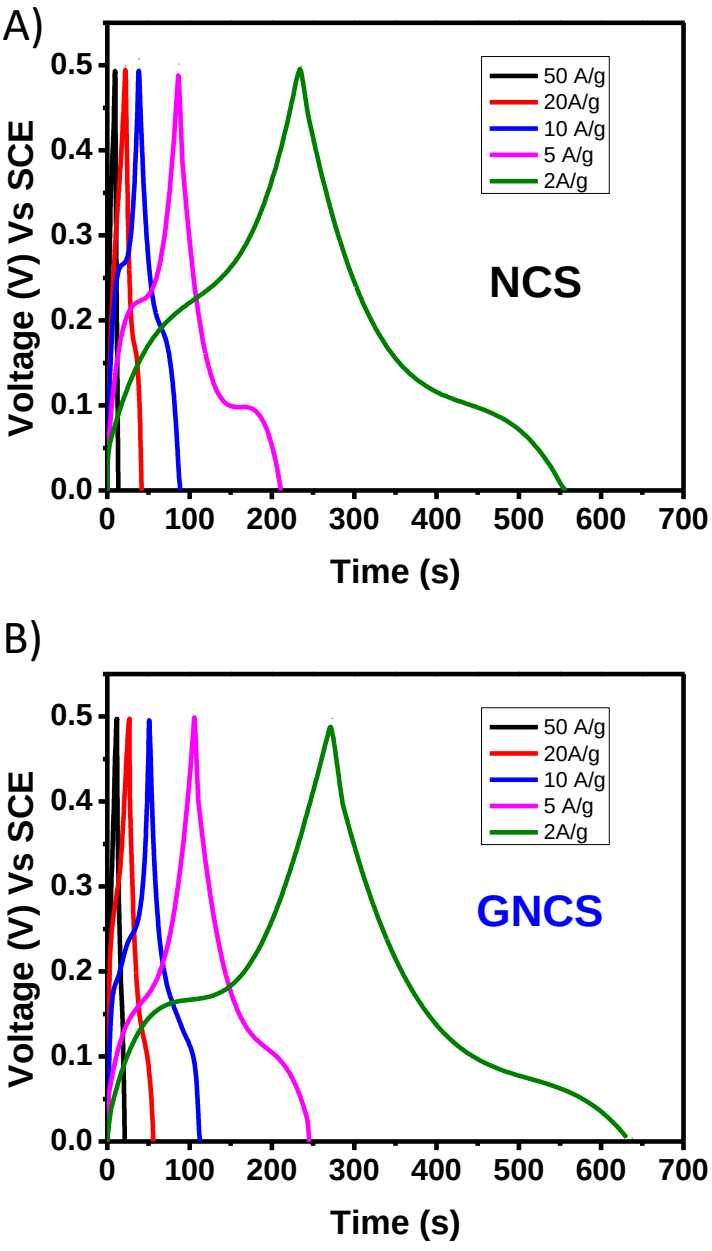

Figure B- 7. CD measurements at different current densities of A) NCS, and B) GNCS. (reprinted from Ref.[53], with permission of the Royal Society of Chemistry)

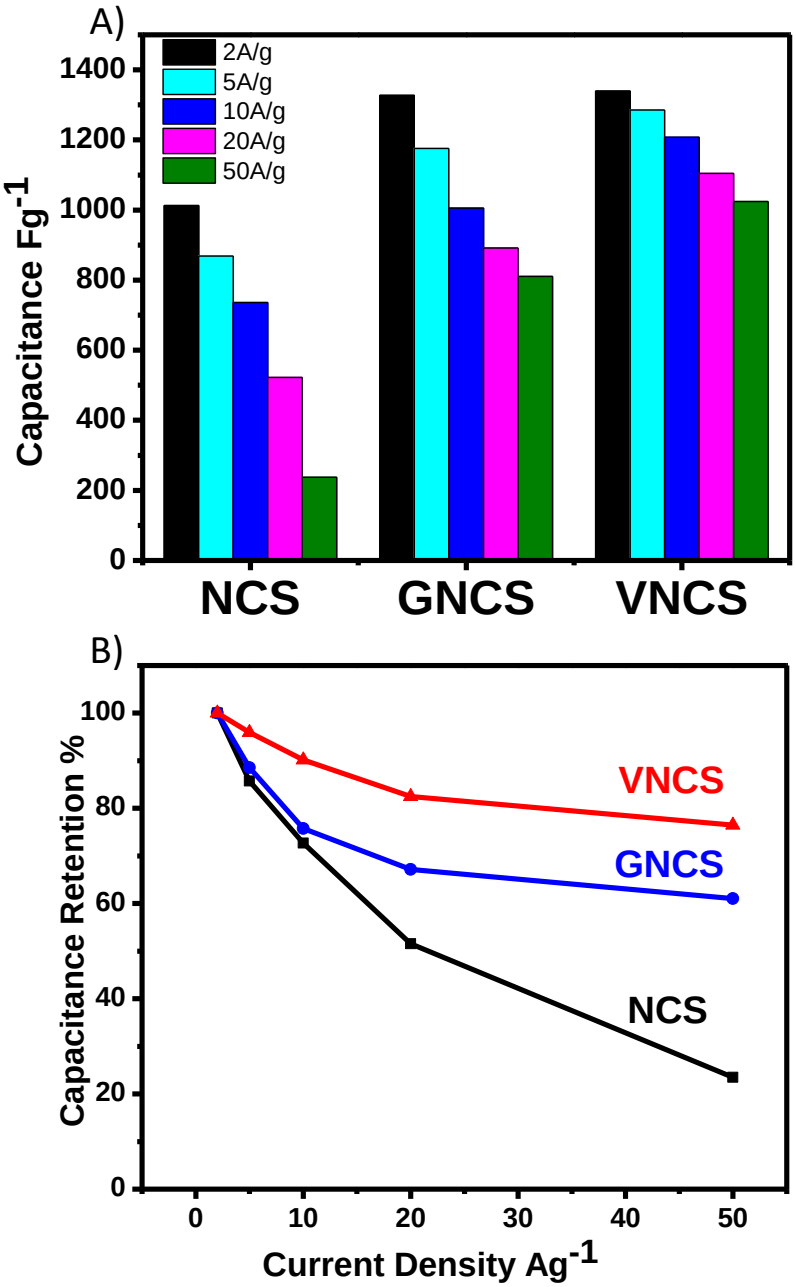

Figure B-8. A) Specific capacitance values of all samples at different current rates, and B) Capacitance retention of all samples at all current densities. (reprinted from Ref.[53], with permission of the Royal Society of Chemistry)

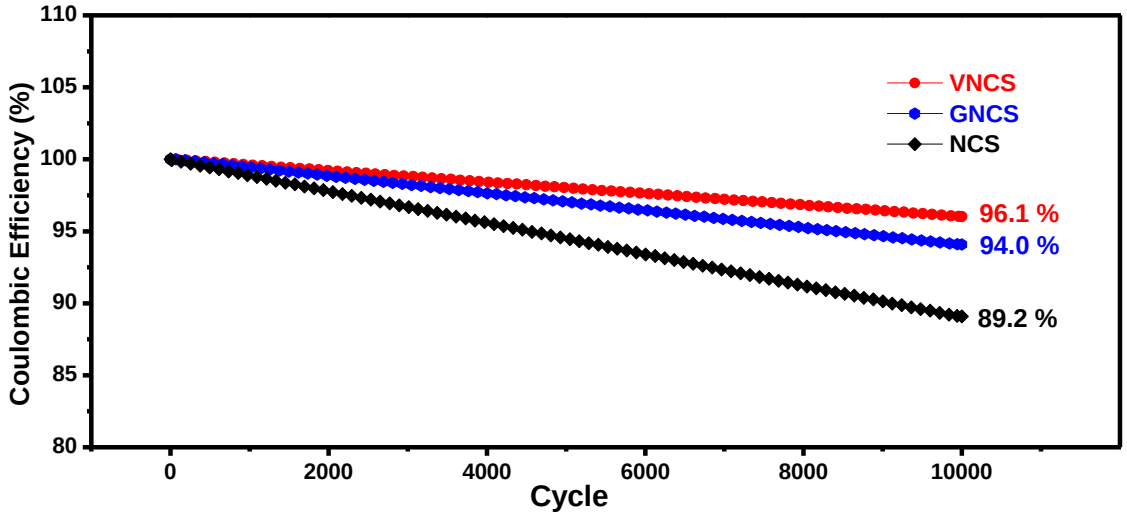

Figure B-9. Columbic efficiency throughout the testing cycles. (reprinted from Ref.[53], with permission of the Royal Society of Chemistry)

Table B-2. Comparison between our work and recent reports (Reproduced from Ref.[53], with permission of the Royal Society of Chemistry)

Ref.	Material	Loading mg.cm^{-2}	Cs @ 2Ag^{-1} (Fg^{-1})	Capacitance retention (%)		Long cycling (Cycles @ current density)	Capacitance at Cycle # 1 (Fg^{-1})	Reported C*apacitance* retention (% @ number of cycles)	Cs Retention at 10000 cycles (%)
				20 Ag^{-1}	50 Ag^{-1}				
This Work	**V-Modified $NiCo_2S_4$ /Graphene**	**2.03-2.25**	**1339**	**82**	**76.5**	**10000 @ 10A/g**	**1160.6**	**90.5 @10000 cycles**	**90.5**
(Ref)[122]	$NiCo_2S_4$ ultrathin Nano sheets/Graphene	Not reported	1451 @ 3A g^{-1}	52.4	Not reported	2000@ 5A g^{-1}	1161	95.4 @ 2000 cycles	Not reported
(Ref)[103]	$NiCo_2S_4$ Nano sheets/Ultrathin	4	1304	85.6	Not reported	6000@8 Ag^{-1}	1248	~ 81 @6000 cycles	Not reported
(Ref)[109]	$NiCo_2S_4$ / Graphene/MoS2	5	1270@ 1Ag^{-1}	45	Not reported	4000@ 5Ag^{-1}	1002	92 @ 4000	Not reported
(Ref)[104]	$NiCo_2S_4$ NS/NCF	2.3	1231	71	Not reported	2000@ 10A g^{-1}	1025	90.4 @200	No reported
(Ref)[143]	(3D) $Ni_xCo_{1-x}S_2$/graphene composite hydrogels	5	1166 @ 1Ag^{-1}	48	Not reported	1000@ 5 A g^{-1}	1084	69.4 @ 1000 cycles	Not reported
(Ref)[106]	$NiCo_2S_4$ urchin-like	2-3	1149 @1 Ag-1	77.3	66.2	5000@ 20 Ag^{-1}	888	91.4 @ 5000	Not reported
(Ref)[182]	$NiCo_2S_4$ porous nanotubes	4-6	1093 @ 0.2 Ag^{-1}	Not reported	Not reported	1000@ 1 Ag^{-1}	933	63 @ 1000 cycle	Not reported
(Ref)[128]	$NiCo_2S_4$ /ball-in-ball hollow spheres	5	1036 @ 1 Ag^{-1}	68.1	Not Reported	2000@ 5Ag^{-1}	892	87 @ 2000 cycles	Not reported
(Ref)[28]	$Ni_xCo_{3-x}S_4$ Hollow Nano prisms	1.0	895.2 @ 1Ag^{-1}	65.3	Not reported	1500@ 5 Ag^{-1}	782	85.7	No reported
(Ref)[142]	$NiCo_2S_4$ nanotubes/binder free	4.2	738 @ 2 Ag^{-1}	73 @ 32 Ag^{-1}	Not reported	4000@ 8 Ag^{-1}	738	93.4 @ 4000 cycles	Note reported
(Ref)[141]	$NiCo_2S_4$ Nanoplates/ Hollow Hexagonal	Not reported	437	52.8	Not reported	1000@ 2Ag^{-1}	388	63 @ 1000 cycles	Not reported

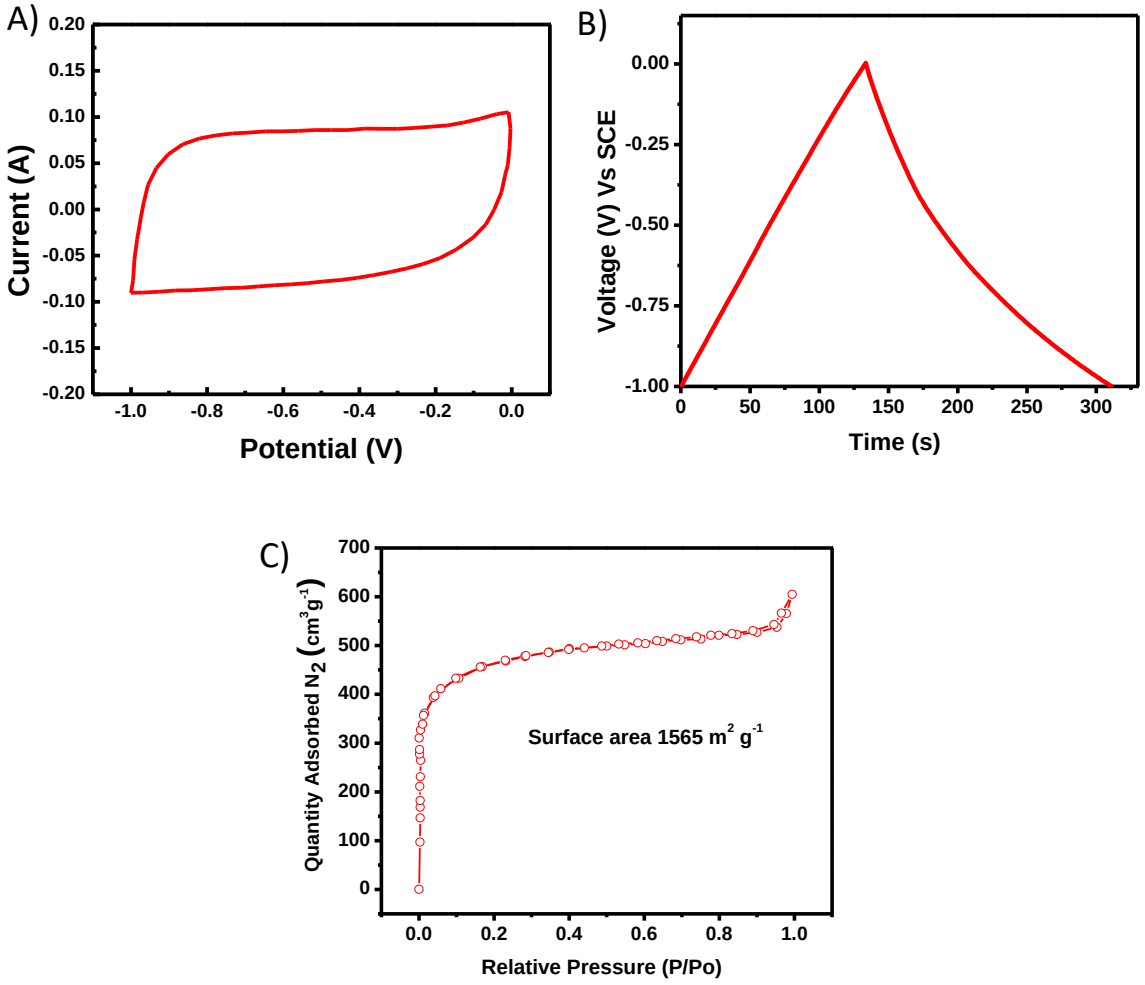

Figure B-10. A) CV of AC/G electrode at 20 mV s^{-1}, B) CD test AC/G electrode at 2A g^{-1}, and C) N2-adsoprtion desorption isotherm of AC/G with BET surace area 1565 m^2 g^{-1}. (Figure A and B reprinted in adapted form from Ref.[53], with permission of the Royal Society of Chemistry)

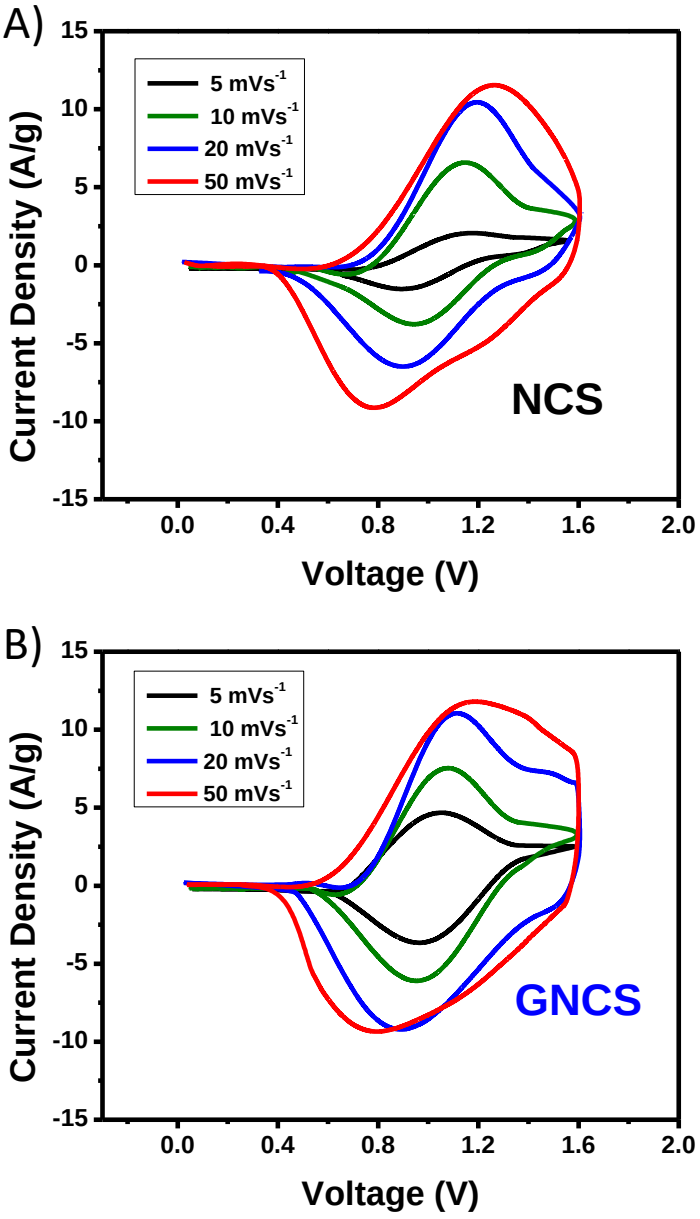

Figure B-11. CV test at different scan rates of A) NCS-HSC samples, and B) GNCS-HSC. (reprinted from Ref.[53], with permission of the Royal Society of Chemistry)

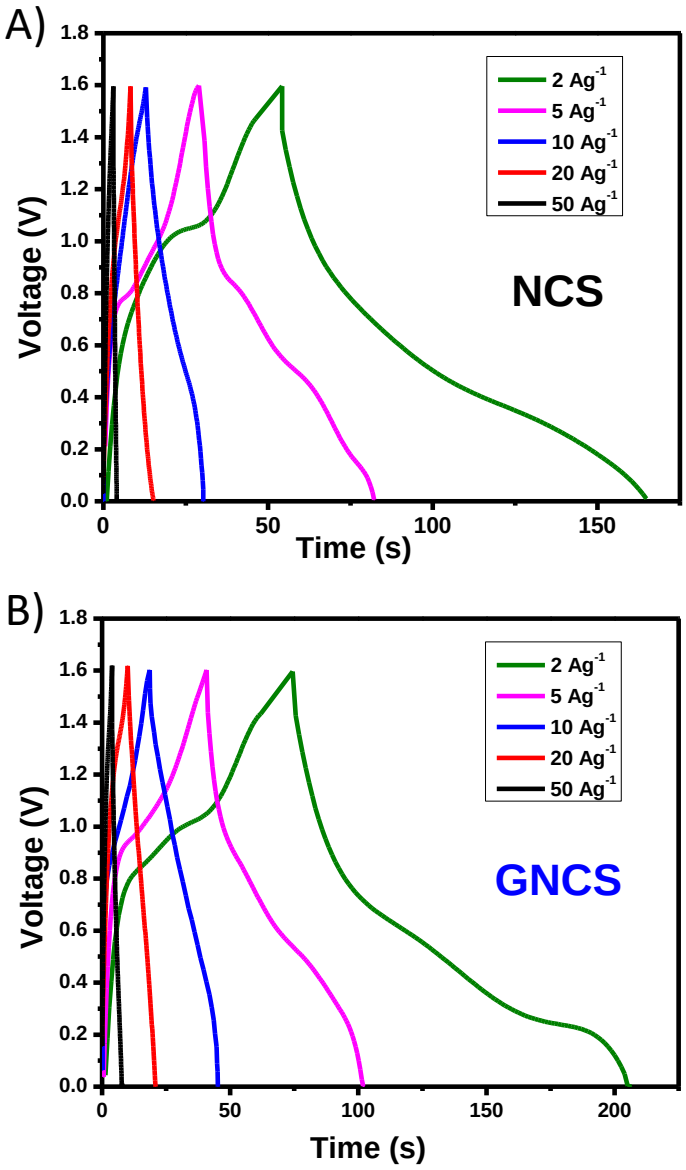

Figure B-12. Charge-Discharge at different current densities of A) NCS- HSC, and B) GNCS- HSC.

(reprinted from Ref.[53], with permission of the Royal Society of Chemistry)

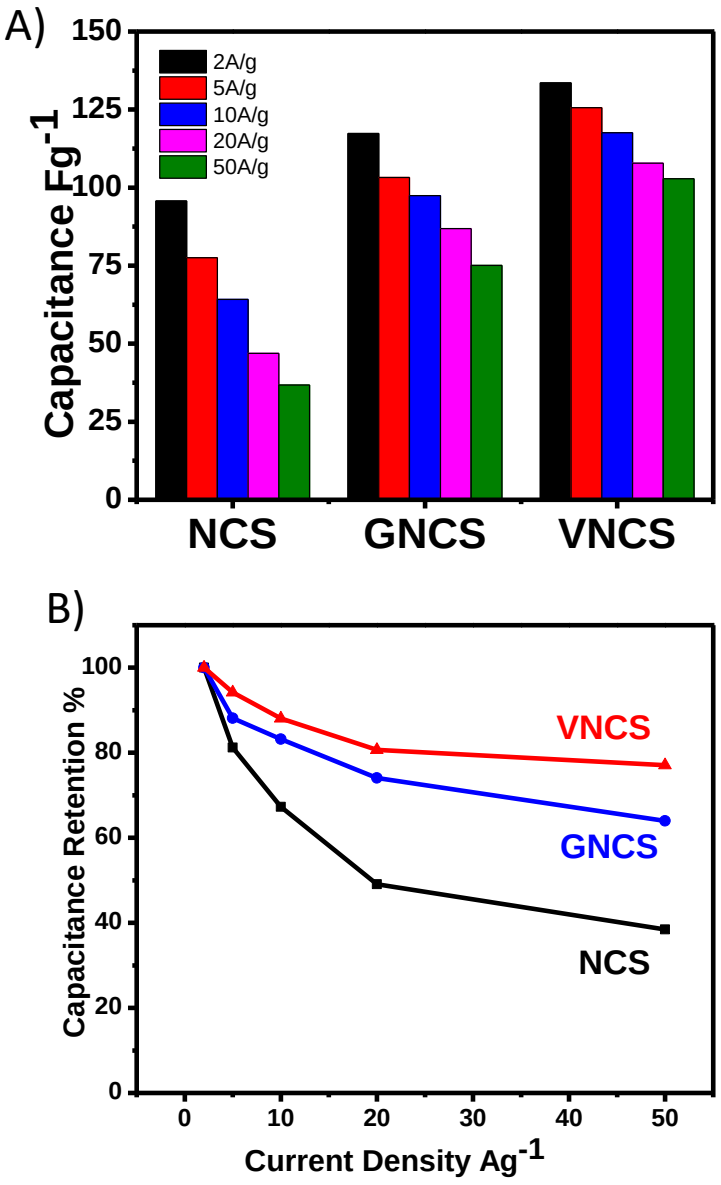

Figure B-13. A) Capacitance values of all devices at different current densities, and B) Capacitance retention of all devices compared to the capacitance value of each sample at 2 Ag^{-1}. (reprinted from Ref.[53], with permission of the Royal Society of Chemistry).